Gas Evolution in Disk Galaxies

Disk Stability, Gas Accretion &
The Impacts of Spiral Density Waves

Hsiang-Hsu Wang
Max-Planck-Institut für Astronomie (MPIA)
Zentrum für Astronomie der Universität Heidelberg,
Institut für Theoretische Astrophysik (ITA)

Heidelberg 2010

Dissertation in Astronomy
submitted to the
Combined Faculties of the Natural Sciences and Mathematics
of the Ruperto-Carola-University of Heidelberg, Germany,
for the degree of
Doctor of Natural Sciences

Put forward by
Lic. *Hsiang-Hsu Wang*
born in Tainan, Taiwan

Oral examination: 19.01.11

Gas Evolution in Disk Galaxies

Disk Stability, Gas Accretion &
The Impacts of Spiral Density Waves

Referees: **Prof. Dr. Ralf Klessen**
Priv. Doz. Dr. Henrik Beuther

Abstract

This thesis studies many aspects of gas evolution in disk galaxies. A simple, effective method is developed for initializing a three-dimensional gaseous disk which is in detailed equilibrium. With this method, theoretical predictions for disk stability and swing amplification are numerically studied for three-dimensional disks. The missing link between intergalactic gas accretion and the star formation activity is found for the galaxy M83. We improve the analysis method to search for the signature of gas infall. For the first time, gas accretion with sufficient fresh gas to fuel star forming disk is kinematically confirmed. The impacts of spiral density waves on gas motions are studied numerically. Shock driven turbulence is quantified and is found to match excellently with observations. Furthermore, the evolution of shock itself has profound impacts on redistributing gaseous surface density, angular momentum and on the development of substructures.

Zusammenfassung

Diese Arbeit untersucht viele Aspekte der zeitlichen Entwicklung von Gas in Scheibengalaxien. Eine einfache und effektive Methode zur Initialisierung einer dreidimensionalen Gasscheibe in detailliertem Gleichgewicht wurde entwickelt. Mithilfe dieser Methode untersuchen wir theoretische Vorhersagen ber Stabilitt und 'Swing' Verstrkung dreidimensionaler Scheiben durch numerische Simulationen. Fr die Galaxie M83 wurde der fehlende Zusammenhang zwischen Akkretion intergalaktischen Gases und der Sternentstehungsrate gefunden. Wir verbesserten die Analysemethode zum Auffinden von Gaseinfall. Zum ersten Mal wurde eine ausreichende Gasakkretion zum speisen einer Sterne formenden Scheibe kinematisch besttigt. Der Einfluss von spiralfrmigen Dichtewellen auf die Gasbewegung wurde numerisch untersucht. Schock-getriebene Turbulenz wurde quantifiziert und stimmt mit Beobachtungen exzellent berein. Des Weiteren hat die Entwicklung des Schocks selbst weitreichende Einflsse auf die Umverteilung von Gasoberflchendichte, Drehimpuls und die Entwicklung von Substrukturen.

Contents

Chapter 1

Introduction

Galaxies are complex systems composed of stars, gas, dust and invisible dark matters, embedded in a relatively vast empty space. These galaxies are the basic building blocks of the Universe. Although modern cosmological models suggest that these visible luminous objects occupy only a small fraction of the constituents of the Universe, our current understanding of the cosmos fully relies on the light emitted by the normal matter. Observational, theoretical and numerical studies on the formation and evolution of galaxies in the past century has largely renovated our viewpoint about the Universe.

1.1 Galaxies in the Universe

1.1.1 Classification of Galaxies

As the heliocentric model of planetary motions suggested by the Polish-born astronomer Nicolaus Copernicus (1473−1543) shifts our standing point in the solar system, a series of pivotal works of Edwin Hubble (1889−1953) profoundly revolutionize our understanding of our position in the Universe. The great Shapley-Curtis debate (1920) over the nature of the nebulae centered on their distances from us and the size of the Milky Way was finally settled conclusively by Hubble's work in 1923. Hubble measured the distances bewteen the Milky Way and several nebulae, including the Andromeda (M31), via the luminosity-period relation of Cepheid variables stars. He concluded that some of the nebulae are too distant to be part of the Milky Way and they are, in fact, our neighbor galaxies. This realization greatly extends the original Milky Way centered viewpoint to a much larger ecosystem in the Universe, i.e., the Milky Way is just one of the countless galaxies.

Galaxies come in different flavors in terms of size and morphology. Hubble's scheme of classification of galaxies (Hubble 1926, 1936) was the first step to understand the nature of galaxies

based on morphology. As shown in Fig. 1.1, Hubble arranged galaxies into the tuning-fork diagram and categorized them into three groups based on their appearance, i.e., ellipticals (E's), spirals (S's) and irregulars (Irr's). Spirals are further divided into two separated sequences, the normal spirals without bars (S's) and the barred spirals (SB's). A transition type between ellipticals and spirals is designated as lenticulars (S0's). Galaxies on the left of the diagram are called 'early' and on the right 'late' in type. This is an unfortunate relic of nomenclature derived from the early misunderstanding of the evolution of galaxies. Before, galaxies were believed to be formed from the collapse of proto-galactic nebulae supported by pressure. As gas falls inward, the kinetic energy is converted into thermal energy and dissipates via radiation. Eventually, due to the conservation of angular momentum, a rotational supported gaseous disk results, ensuing the structure development such as spirals and bars.

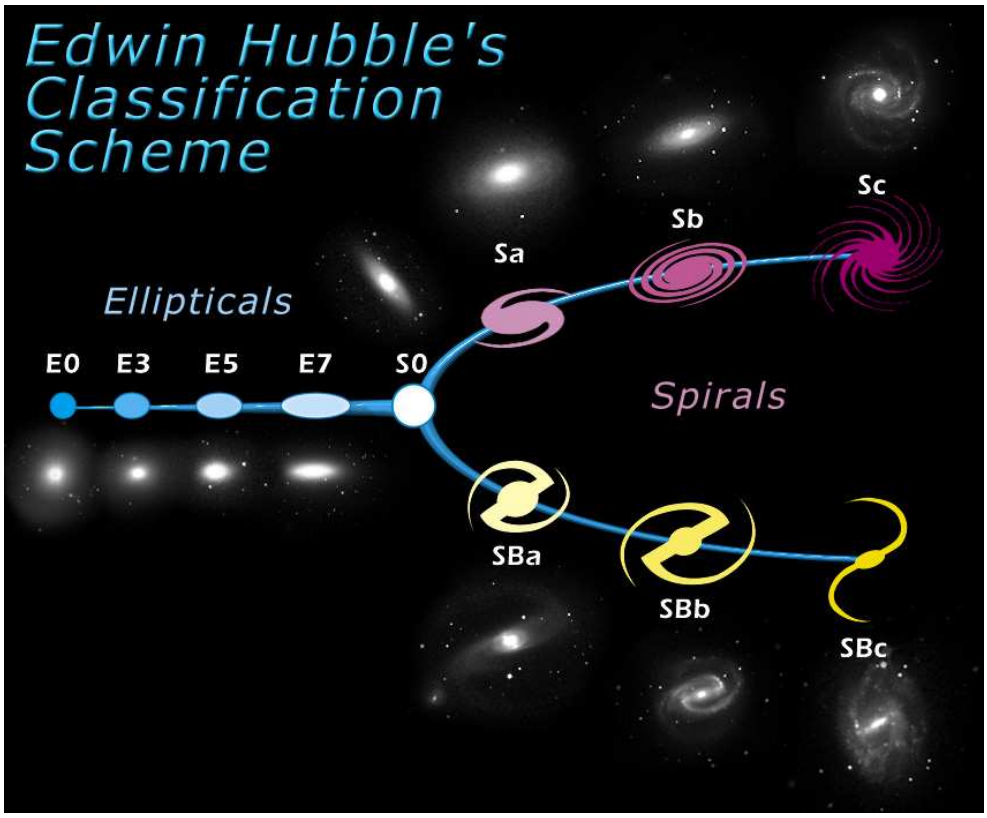

Figure 1.1: Diagram of Hubble's Tuning Fork classification scheme from Hubblesite.

Ellipticals are classified based on their apparent axial ratio, $\epsilon \equiv 1 - b/a$, where a and b represent the apparent major and minor axis, respectively. Ellipticals with an apparent axial ratio, ϵ, are designated with 'Eα', with $\alpha \equiv 10\epsilon$. For instance, ellipticals with $\epsilon = 0.3$ are classified as E3 and sphericals with $\epsilon = 0$ as E0. Ellipticals with $\epsilon > 0.7$, however, have never been observed. Spiral galaxies are morphologically more interesting than ellipticals. Spiral galaxies, normal and barred, having the most conspicuous bulge-to-disk luminosity ratios are classified as 'Sa' or

'SBa'. These galaxies are also the most tightly wound spirals. Those with the least bulge-to-disk luminosity ratios and the most open spirals are classified as 'Sc' or 'SBc'. Whereas, the intermediate ones are classified as 'Sb' or 'SBb'. Lenticulars are disk galaxies without visible spirals. Due to the lack of gas and dust, they usually appear featureless (S0/SB0) with very little ongoing star formation activities. For those galaxies, which have no obvious regular structure, are classified as 'Irr'.

Based on Hubble's work, de Vaucouleurs (1959) refined the tuning-fork and incorporated other important morphological features into the scheme. For disk galaxies, De Vaucouleurs introduced the new notation 'SA' for spirals without bar, 'SAB' for spirals with a weak bar, 'SB0' for barred lenticular galaxies, 'Sd'/'SBd' for bulgeless spiral/barred galaxies with diffuse, broken arms. Galaxies of highly irregular appearance are denoted as 'Im'. Irregular bulgeless galaxies similar to Magellanic could are represented as 'Sm'/'SBm'. In addition, notation 'r' is used to incorporate the presence of rings in galaxies. Surprisingly, although this simple classification scheme is originally designed only for describing the morphology of galaxies, it correlates very well for quantities of galaxies such as bulge-to-disk ratio, gas content, colors, metallicity, star formation activities, etc.

1.1.2 Galaxy Distribution in The Universe

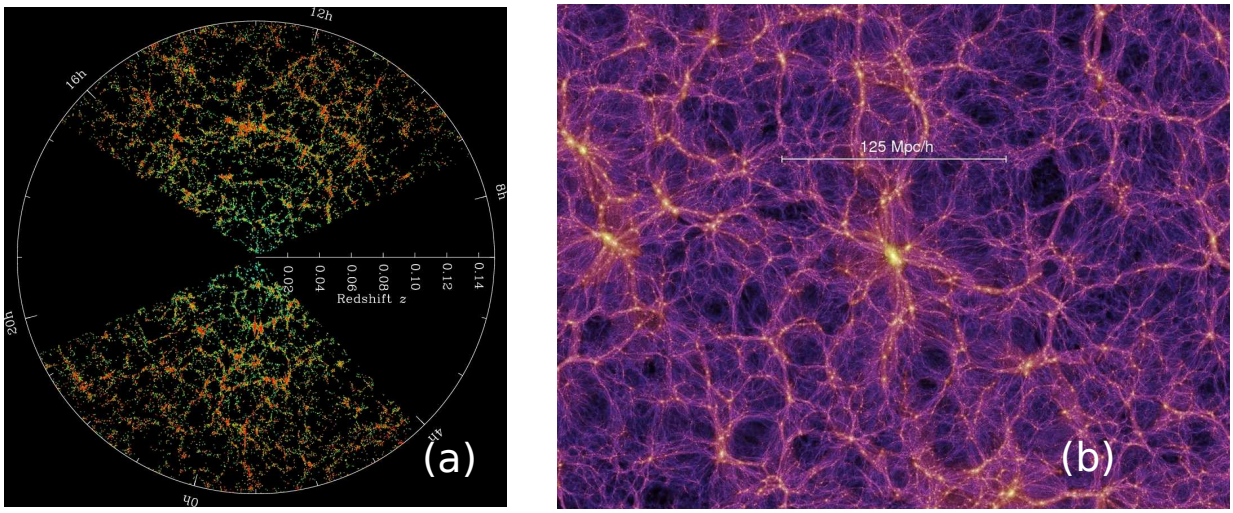

Figure 1.2: (a) Slices through the SDSS 3-dimensional map of the distribution of galaxies. Earth is at the center, and each point represents a galaxy, typically containing about 100 billion stars. *Credit*: M. Blanton and the Sloan Digital Sky Survey. (b) Dark matter distribution in the CDM Universe predicted by the Millennium Simulation (Springel et al. 2005).

To build up the correlations between morphology, galaxy properties and environment, one needs

to understand the evolution course of galaxies over cosmological time scales. Hubble's next celebrated discovery, Hubble's law (Hubble 1929), was empirically derived as $v = H_0 D$, with v being the recession velocity, the Hubble constant H_0 (73.5 ± 3.2 km s^{-1} Mpc^{-1} derived from the five-year WMAP, 2008) and D the proper distance. It states that the galaxies in deep space are drifting away from Earth with a velocity, v, proportional to their distance, D, from Earth. Hubble's results together with the cosmological principle suggests that the Universe has a starting point in spacetime. This concept is now known as the big bang theory (Lemaître 1927).

Galaxies evolve with the Universe. A model that is able to describe the evolution and the structure formation in the cosmos is required. Λ Cold Dark Matter (ΛCDM) is now considered as the best current model of the big bang cosmology. Every cosmology which takes into account the existence of dark energy as well as cold dark matter is labelled in this category. These models are being able to account for several observation facts: (i) the existence and structures in Cosmic Microwave Background (CMB) observed from the Wilkinson Microwave Anisotropy Probe (WMAP, Spergel et al. 2007) (ii) the accelerating expanding Universe inferred from the redshift-distance relations from Type Ia supernovae (Riess et al. 1998; Perlmutter et al. 1999) (iii) large scale structures of galaxy clusters (iv) the abundance of primordial elements. In the CDM paradigm, structures are formed bottom-up, i.e., small objects gravitationally collapse first and massive objects are formed through a continuously hierarchical merging (White & Rees 1978; Kauffmann et al. 1993; Lacey & Cole 1993). Since dark matter only interacts with matter gravitationally, it evolves faster than the normal matter in the early Universe. With the expansion of the Universe, gas cools and gradually falls into a potential well due to the overdensity of dark matter. Eventually, stars form collectively through gravitational collapse of gas and galaxies are born.

Recently, large scale survey such as Two-degree-Field Galaxy Redshift Survey (2dFGRS) and Sloan Digital Sky Survey (SDSS) have characterized the large scale structures in a three-dimensional fashion. As shown in Fig. 1.2a, galaxies are not distributed randomly. They are organized in a form now called 'cosmic web' composed of large filamentary, sheet-like structures as well as bubble-like voids. These maps may shed light on how galaxies form, be used to test the cosmological paradigm and to understand the nature of dark matter and dark energy. In order to accomplish these goals, a large scale numerical simulation called Millennium Simulation is carried out by Virgo Consortium (Springel et al. 2005). A snapshot of the distribution of dark matter is shown in Fig. 1.2b.

Although the Millennium simulation seems to be able to reproduce the complex 'cosmic web', the simulation fails to replicate the voids as observed in Fig. 1.2a, which actually stresses the distribution of luminous matter. This suggests that either a bias exists between the mass distribtution of luminous and dark matter or the physics of CDM model is incomplete.

1.1.3 Environmental Effects on Galaxies

From Fig. 1.2a, it is evident that galaxies are not distributed randomly. Galaxy formation in the context of hierarchical ΛCDM scenario suggests a tight relation to the halo mass assembly process (Evrard et al. 1990). The frequency of different type of morphology turns out to be sensitive to the environment. The Local Group, for example, comprises ~35 galaxies in which only three are spirals namely the Milky Way, M31 and M33. The remainder are classified between irregular and dwarf elliptical galaxies. In general, the relationship between the morphological type and the environments in which they are located are quantified by Morphology-Density relation (Dressler 1980; Postman & Geller 1984; Whitmore et al. 1993; Goto et al. 2003; Maulbetsch et al. 2007). The magnitude-limited survey for galaxies outside clusters are strongly biased to the late type spirals (80%) with the rest equally 10% attributed to S0 and ellipticals. The trend changes smoothly with increasing population density. In the groups with an intermediate density, 40% spirals, 40% S0 and 20% of ellipticals, whereas in the rich clusters, the mix is 10% spirals, 50% S0 and 40% ellipticals. Luminous cD galaxies are generally found in the center of rich clusters. Toomre & Toomre (1972) show that galaxy merger is one of the effectively ways responsible for the morphology transformation from spirals to ellipticals. Since then, this scenario has been used to explain the formation of massive ellipticals (van der Wel et al. 2009 and references therein). Figure 1.3 shows two examples of colliding galaxies, the Stephan's Quintet and the Antennae Galaxies. Collisions between galaxies are common in clusters and often result in more massive ellipticals.

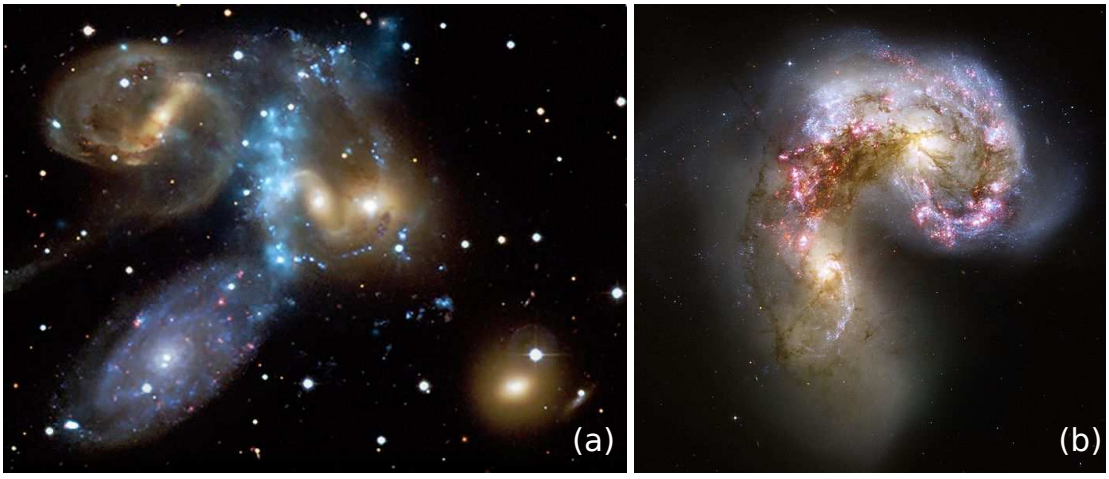

Figure 1.3: (a) Stephan's Quintet (NGC 7317, 18a, 18b, 19, 20). Image Credits: X-ray (blue): NASA/CXC/CfA/E. O'Sullivan Optical (brown): Canada-France-Hawaii-Telescope/Coelum. (b) The Antennae Galaxies (NGC 4038/NGC 4039). Image Credits: NASA, ESA, SAO, CXC, JPL-Caltech, and STScI

Environment not only has profound impact on the structure of galaxies but also on its star forma-

tion history. There is strong evidence showing that the star formation activity is quenched when a galaxy enters a dense cluster. The reason for the suppression of star formation is still unclear despite several possibilities have been proposed such as the ram-pressure stripping (Gunn & Gott 1972), galaxy harrasment (Moore et al. 1996; Bell et al. 2007; Ruhland et al. 2009) and galaxy starvation (Larson et al. 1980).

1.2 Spiral Galaxies

1.2.1 Spiral Density Waves and Substructures

Numerical simulations conducted by Toomre & Toomre (1972) showed that disks are fragile to external disturbances. A violent gravitational harrasment from an intruder of roughly equal mass stirs the rotational spin of disk, randomizing the orbits of stars which results in a morphological transformation from a disky to an elliptical galaxy. In the last Section, we notice that late-type disky galaxies are dominant in low-density regions in the Universe. In these relatively isolated areas, up to 80% are found to be disky, suggesting that these disks may have been evolved over a cosmological timescale without a major merger event. Disk galaxies are usually spirals. Among them about two-thirds are barred (de Vaucouleurs 1963), one third being strong barred and the other one third being weak barred. Furthermore, they are usually gas rich, luminous and actively forming stars. All these properties suggest that the Universe has prepared a laboratory which is under a relatively good control for us to study the relationship of gas and stars, the angular momentum of primordial gas, the history of gas accretion, the primordial cosmic magnetic field, the properties of dark matter, etc. Understanding the evolution course of disk galaxies therefore becomes a focal point of attention.

A disk galaxy is a flat, rotationally supported 'cosmic frisbee' consisting of stars, gas, dust, spheroidal concentration of stars in the center now known as the 'bulge' and globular clusters residing in the dark halo. The striking spiral we perceive on the photoplates of nearby galaxies only tells us a part of the story. The luminous spirals are due to the bright, young, massive stars which contribute only a small fraction of the total stellar population. Images taken from near-infrared wavelength shows smooth, broad, sinusoidal spirals that represent the older stars (population II), which is the main body of galactic disks. For instance, over 90% of the total mass of the Milky Way disk belongs to this population.

Gas is dissipative and is relatively cold with a typical velocity dispersion of $\sim$10 km s^{-1}. Stellar disk, however, is treated as an ensemble of collisionless stars with a much larger typical dispersion velocity 40 km s^{-1}. The different nature of gaseous disk and stellar disk leads to

two separate approaches to study the galactic structure. On the one hand, the smooth, broad, sinusoidal-varing spirals seen in near-infrared suggests the use of linear theory of density waves for the disk stars. On the other hand, the narrow luminous spirals composed of gas, dust and young stars are treated as a nonlinear problem of gasdynamics. The tight correlation between gas spirals and stellar spirals suggests that this two problems are not entirely separable. They are inter-related to each other through the gravitational field to which they both contribute.

Figure 1.4 shows one of the most spectacular spiral galaxies NGC 5194 (M51) and its companion NGC 5195. It is believed that the grand-design spirals are the result of tidal interaction between them. On the inside edge of the bright optical arms, the narrow dust lanes, which obscure the visible light emitted from bright stars, follow the spiral shape. Fujimoto (1966) suggests that the dust lanes seen along the luminous arms are the results of galactic shocks. The narrow dust lanes, albeit makes up only 1% the total mass of interstellar medium, effectively obsecure the visible starlight, marking the location of gaseous density peak.

Figure 1.4: NGC 5194(M51)/NGC 5195. Image Credits: STScI/AURA, ESA, NASA.

Within the framework of Quasi-Stationary Spiral Structure (QSSS) hypothesis, Roberts (1969) and Woodward (1975) semi-analytically work out shock solutions attempting to find an explaination for the large-scale star formation along the spiral arms. When gas clouds of sub-critical mass pass through the spiral shocks, they get compressed into super-critical mass, triggering gravitational collapse and form stars. This picture naturally predicts a geometrically angular shift between the densest HI and the peak emission of H_α, which traces young stars. Roberts (1969) qualitatively confirms this prediction using the the data available at that time. The angular offsets are also found between CO and H_α (Vogel et al. 1988; Garcia-Burillo et al. 1993; Rand & Kulka-

rni 1990; Scoville et al. 2001), dust lanes and H_α (Roberts 1969; Rots 1975). Recently, Tamburro et al. (2008) also find the angular shift in emissivity peaks between HI (data from THINGS) and 24 μm (data from SINGS), which traces the dust-shrouded massive stars. Kinematic evidences that support the galactic shock scenario come from the analysis of non-circular motion along spirals (Aalto et al. 1999; Visser 1978a,b; Roberts & Stewart 1987; Shetty et al. 2007). Velocity component which is perpendicular to shocks is expected to drop proportional to the density contrast measured before and after the shock, resulting in a net radially inward streaming motion.

In addition to grand-design spiral arms, the structures between them are far more complicated. Substructures perpendicularly protruding from the spirals are identified as spurs or feathers. Many theoretical studies has been carried out to explain the nature and the origin of spurs. Semi-analytical calculations without involving self-gravity attribute the substructures to the ultra-harmonics (Woodward 1975; Shu et al. 1973). Balbus (1988) views the substructures as a result of the growth of gravitational instability in preferred directions. Numerical works that follow the nonlinear development of gas has also been conducted (Kim & Ostriker 2002a; Chakrabarti et al. 2003; Wada & Koda 2004; Kim et al. 2006; Dobbs & Bonnell 2006). Among them, Wada & Koda (2004) and Kim et al. (2006) propose that spiral shock is potentially a major ingredient capable of tapping randomized energy from the regular rotation motions. Despite many works which have been dedicated to explore possible mechanisms that may induce the substrutures, the impacts of grand-design spiral waves on ISM turbulence are still less recognized in the literature.

1.2.2 Star Formation, Turbulence and Gas Accretion

Spiral galaxies roughly of the size of the Milky Way are actively making stars due to their higher gas surface density. Schmidt (1959) and Kennicutt (1998) find that star formation rate, $\Sigma_{\rm SFR}$, is related by a simple power law with gas surface density, $\Sigma_{\rm SFR} \propto \Sigma_{\rm gas}^n$, with $n = 1.4$, over several order of magnitude in surface density. This relation is now referred to as the 'Kennicutt-Schmidt law'. Furthermore, there appears a threshold surface density (Kennicutt 1989, 1998; Martin & Kennicutt 2001) above which star formation is activated by disk instability (Toomre 1964; Jog & Solomon 1984; Rafikov 2001). This threshold surface density suggests a cut-off radius beyond which the surface density is too low to form stars.

However, the low efficiency of turning gas into stars in molecular clouds suggests the star formation process is regulated by a variety of processes, i.e., the interplay between gravitational instability, magnetic fields, gaseous dissipation and turbulence. Turbulence can be found on a wide span of scales ranging from intergalactic gas down to protostellar accretion disks. Since the energy of turbulence can dissipate in one crossing time, its ubiquity poses a strict constrain on possible driving and maintaining sources. In spiral galaxies, a remarkable fact is that the velocity

dispersion measured in HI emission lines is observed to be fairly constant extending from inner star-forming disks to regions well beyond optical disks (Dickey & Lockman 1990; van Zee & Bryant 1999; Tamburro et al. 2009). The inferred values are in a range between 10 km s^{-1} and 20 km s^{-1} (Bigiel et al. 2008; Walter et al. 2008).

Within the star-forming disk, several possibilities such as steller feedback (see Mac Low & Klessen 2004; Elmegreen & Scalo 2004 and references therein), gravitational instability (Agertz et al. 2009), swing amplification (Goldreich & Lynden-Bell 1965; Toomre 1981; Agertz et al. 2009), magnetorotational instability (MRI, Balbus & Hawley 1991; Sellwood & Moore 1999; Piontek & Ostriker 2004, 2005, 2007) and spiral density waves (Wada & Koda 2004; Kim et al. 2006), has been proposed as mechanisms driving turbulence. Given the lack of correlation between turbulence and star formation in the outskirts of galaxies, other type of sources apart from stellar feedback could be responsible for injecting the turbulent energy. Recently, Klessen & Hennebelle (2010) propose that the turbulent energy observed in the outskirts of galaxies is a natural outcome of galactic gas accretion. The efficiency needed to convert infall motions into the required level of turbulence is only a few percent in Milky Way type galaxies.

Following the line of Klessen & Hennebelle (2010), problems of star formation, ISM turbulence and gas accretion are evidently inter-related. The Milky Way is forming new stars at a rate of $\dot{M}_{\rm SF} \geq 2$ $M_\odot$ yr^{-1} (Diehl et al. 2006). Assuming a constant star formation rate, without an external gas supply, star formation will run out of gas in a few billion years much less than the Hubble time (Pflamm-Altenburg & Kroupa 2009; Klessen & Hennebelle 2010). Similar gas depletion time is also reported for many nearby spiral galaxies (Bigiel et al. 2008). Furthermore, it is well-known that the star formation rate was higher in the past than it is today, suggesting an even shorter depletion time around only one billion years in the early Universe (Hippelein et al. 2003; Hopkins & Beacom 2006; Genzel et al. 2010; Daddi et al. 2010a,b).

Two popular scenario has been proposed to explain how the intergalatic gas accretes onto the disk. The first is directly related with the process of galaxy formation called the 'hot mode' (White & Rees 1978). Intergalactic gas falls into the dark matter potential, gets shocked and virialized. Overtime, the gas cools down and gentlely rains down onto the disk. This scenario might be supported by the detection of velocity gradient perpendicular to the galactic plane (Fraternali et al. 2005). Numerical simulations, however, suggest the other possibility. Gas can reach the center of the potential in a form like clouds, streams and filaments (Kereš et al. 2005; Dekel & Birnboim 2006; Kereš et al. 2009). This scenario is now known as the 'cold mode'. In this thesis, we are the first to provide the observational evidences that support the 'cold mode' accretion.

Direct evidences that support the scenario of ongoing gas accretion come from the observations of high velocity clouds (HVCs) moving towards disks, which are identified by the kinematic

anomaly appearing in the p-v diagram (Wakker et al. 2007; Fraternali 2009). A simple energy estimation shows that they cannot be the results of galactic fountain. In all, the visible accretion rate of cold gas in galaxies is estimated ~0.2 $M_\odot$ yr^{-1}, one order of magnitude less than the required gas infall in order to sustain the star formation over cosmological timescales (Sancisi et al. 2008; Fraternali 2010).

1.2.3 Dark Matter Halo

The existence of dark matter in spiral galaxies is inferred from their rotation curves. If we combine the mass distribution of luminous matter including stellar mass, gas, interstellar dust and halo stars, a Keplerian fall-off ($V_{\rm rot} \propto R^{-1/2}$, with $V_{\rm rot}$ being the rotation velocity and R galactocentric radius) in the outer part of rotation curve is expected. However, instead of the Keplerian fall-off, nearly flat rotation curves are traced far out of optical disks through 21 cm emission lines and still show no sign of declination (de Blok et al. 2008). If we use the rotation speed to measure the mass distribution as a function of radius in spiral galaxies, the 'missing mass' now coined with the name 'dark matter' is required to provide enough gravitational force in order to support flat rotation curves.

Our understanding about the nature of dark matter is still very little. It is dark because it does not emit light. It is hard to detect because it is not supposed to interact with luminous matter except through the gravitational effects. It is important because it occupies 80% the mass budget of matter and therefore dominates the evolution of structure formation in the Universe. Within the framework of cold dark matter, the dark matter is believed to move at normal velocity contrast to the warm dark matter moving at relativistic velocity and to the hot dark matter moving at ultrarelativistic velocity.

A galactic disk is believed to be embedded in a dark matter halo. Numerical simulations conducted by Julio Navarro, Clarlos Frenk and Simon White in 1996 reveal a universal density profile of halo as described in Eq. (2.26). In their simulations, this profile is found over a wide range of size and mass scales, ranging from dwarf galaxies to rich clusters of galaxies. However, other detailed simulations find the shape of dark halo to be triaxial and r^{-1} cusp in the center (Frenk et al. 1988; Dubinski 1994; Hayashi et al. 2004, 2007; Capuzzo-Dolcetta et al. 2007). Many observational efforts has been dedicated to confirm these predictions kinematically. They find the center of halos is not characterized by a r^{-1} cusp but by a central kpc-sized 'core' (Kuzio de Naray et al. 2008 and references therein). The triaxial profiles are also not supported by measuring the noncircular motions in spiral galaxies (Trachternach et al. 2008 and references therein). The dark matter halo seems to be in a round shape.

These discrepancies pose challenges to the nature of dark matter, the structure formation in disk

galaxies, e.g. bar/bulge formation due to the interaction between stars and dark matter, and the evolution of disk galaxies.

1.2.4 Stellar Disks

As described in the previous sections, gas evolves in the potential largely contributed by the dark matter and the stellar disk. Photometrically, stellar disk can be decomposed into a central concentrated bulge and an exponential disk of a constant scale-height. In the following, we describe the profiles of both components.

Outside of centeral bulge, surface brightness (emission from stars) observed from other disk galaxies suggests an exponentially radial profile, $I(R) = I_{\rm d}\exp(-R/R_{\rm d})$, with $I_{\rm d}$ being the extropolated centeral surface brightness, R the galactocenter distance and $R_{\rm d}$ the scalelength of the stellar disk. Recent result shows the scalelength for the Milky Way is estimated 2.5 ± 0.5 kpc. The vertical structure of the stellar disk can be inferred from the observations of edge-on disk galaxies. Optical observations suggest the luminosity distribution perpendicular to disks can be reasonably fitted with the $\mathrm{sech}^2(z/z_{\rm d})$ profile, where z describes the height away from the midplane and $z_{\rm d}$ the scaleheight of disks. This vertical structure can be understood by a self-gravitating sheet with Gaussian velocity dispersion independent of z (Spitzer 1942). Combining these results leads to a description for a three-dimensional stellar disk:

$$I(R,z) = I_{\rm d}\exp(-R/R_{\rm d})\mathrm{sech}^2(z/z_{\rm d}). \tag{1.1}$$

The stellar disk can be further decomposed into a thin disk populated with younger massive metal-rich stars (population I) and a thick disk with older metal-poor stars (population II) (Burstein 1979; van der Kruit & Searle 1981a,b). In the solar neighborhood, the scaleheight of the thin disk is measured 300 pc and 1 kpc for the thick disk. Over 90% of mass is concentrated in the thin disk. The variation of the vertical extent in stellar disks was estimated to be independent of the radius from earlier observations of edge-on disk galaxies (van der Kruit & Searle 1981a,b). However, near infrared observations of Kent et al. (1991) suggest a moderate flaring beyond 5 kpc in the Milky Way with a slope of 20 pc kpc^{-1}. The same trend has been confirmed for a larger sample of edge-on disk galaxies (de Grijs & Peletier 1997).

In addition to stellar disks, disk galaxies of late-type passing from S(B)a to S(B)c contain a bulge with decreasing central bulge/disk luminosity ratio ranging from $L_{\rm bulge}/L_{\rm disk} \sim 0.3$ to $L_{\rm bulge}/L_{\rm disk} \sim 0.05$. The bulge of the Milky Way, for example, contributes 15% of the total luminosity.

Bulges can be subdivided into three types: classical bulges, box/peanut bulges and disk-like bulges. A classical bulge is described as a spheroidal structure containing old stars with little star

formation activity and dust compared to the disk component. Their surface brightness can be fitted with an $r^{1/4}$ law now known as De Vaucouleurs' law (Carollo et al. 1999). Several scenarios has been proposed to explain the formation of classical bulges. Steinmetz & Muller (1995), in their numerical simulations, suggest that bulges can form during the first starburst triggered by the gravitational collapse. Later, Steinmetz & Navarro (2002) show that the merger of disk galaxies of similar size at redshift $z \sim 3.3$ can stir stars in the disk and form a bulge progenitor. Noguchi (1999) proposed that dense clumps can form in a proto-disk via graivitational instability. These clumps then gradually spiral towards the center of galaxy by dynamical friction and form a classical bulge. As for box/peanut bulges, numerical simulations carried out by Athanassoula (2005) conclude that this type of bulges are simply part of the result of secular evolution of bars seen in nearly edge-on galaxies.

Kormendy (1993) points out that many bulges, which are classified by the $r^{1/4}$ law, have properties similar to disks other than bulges in terms of morphology and kinematics. In fact, they often present structures like spirals, rings, dust lanes and star forming knots in the very center of galaxies. The well-organized structures suggest that it cannot be formed through violent mergers. Secular evolution of disk might be responsible for this type of bulge. In all, the formation of disk-like bulges is still unclear.

The tight correlation between the mass of supermassive black holes, M_{bh}, and the velocity dispersion, σ, of the surrounding stellar bulges suggests that black holes somehow evolve with bulges (Ferrarese & Merritt 2000; Gebhardt et al. 2000). This relation is now known as the M_{bh}-σ relation. Since then, other relations that correlate the mass of black holes and the properties of host bulges has been found. Graham et al. (2001) shows that M_{bh} correlates with the concentration of the host bulge quantified by the Sersic index n. Marconi & Hunt (2003) and Häring & Rix (2004) demonstrate a good correlation between the mass of supermassive black holes and the mass of bulges. To sum up, a black hole with larger M_{bh} tends to have a larger velocity disperion, a more concentrated bulge and a more massive bulge. Given that different kinds of bulge discussed in the above, the physical origin and the implication of these relations are still unclear.

1.2.5 Gaseous Disks

Overall, gas content is more rich in late-type galaxies than earlier types. In optical, most of the gas concentrates in the galactic midplane with a scaleheight significantly smaller than stellar disks. Unlike stellar disk, the distribution of gaseous disk is less well defined due to complex phase transitions, star-gas interactions, star-forming processes, gas accretion, etc.

In general, the distribution of HI gas detected by 21 cm lines is fairly flat and uniform with a scalelength much larger than stellar disk (Leroy et al. 2008), while in some galaxies a HI hole is

present in their center. HI gas can be traced far beyond optical disks and is usually significantly flaring in the outer disk (Lockman 1984; Wouterloot et al. 1990; Klessen & Hennebelle 2010). The ubiquity and the abundance of HI makes it the most important tracer to study the dynamics of disk and the interaction of galaxies. The molecular, H_2, is not easy to observe. Its abundance is usually inferred from the transition lines of CO in the radio or the infrared portion of spectrum. Unlike the widespread HI, molecular gas concentrates towards the centers of galaxies and is often structured into the form of giant molecular clouds (GMCs) or dark clouds. In the outer part of galaxies, molecular clouds are often organized along the spiral arms. The ionized gas emits visible light as an electron recombines with a proton. This process happens when the ultraviolet light emitted from the young, bright, massive stars ionizes the surrounding neutral atomic HI.

The scaleheight of HI disk is observed to be nearly constant in the inner Milky Way (< 8.5 kpc). This was a long-standing puzzle since the scaleheight of gas disk is expected to increase with radius due to the exponentially descreasing surface density of the stellar disk (Oort 1962). This is mainly because in earlier approaches, the self-gravity of gas is often neglected due to its small fraction of total mass compared to the stellar disk. Recently, Narayan & Jog (2002) revisited this problem in a semi-analytical way. They adopt the velocity dispersion of stars, neutral gas and molecular gas from observations and include the joint gravity contributed by stars, dark matter and gas. By assuming the gas disk is in hydrodynamic equilibrium in the vertical direction, their results fit excellently to the observed scaleheight. Furthermore, they also find that the gas disk also has impact on the scaleheight of stars. Because the vertical velocity dispersion of stars is only 20 km s^{-1} measured in the solar neighborhood. Their results suggest that the vertical structure of disk is sensitive to the gravity of all ingredients, i.e, stars, dark matter and gas. To properly model a galactic disk in numerical simulations, one needs to treat the vertical structure self-consistently in order to have an equilibrium disk.

1.3 Layout of The Thesis

We have outlined the properties and some questions associated with each constituent in a disk galaxy. The interplay between each component makes the evolution of disk galaxies extremely complicated. On small scales, stars form from the gravitational collapse of gas. Stellar feedbacks enrich the gas content, affecting the chemical evolution of interstellar medium. Energy released from stars regulates the birth rate and properties of next generations of stars. Ultraviolet lights emitted from stars ionize the neutral gas, coupling the evolution of gas and stars to interstellar magnetic fields. On large scales, disk instability forms structures such as spirals and bars. Subsequently, the secular evolution of disk appearance is reshaped by the torques excerted by spirals and bars over cosmological timescales (Foyle et al. 2010 and references therein).

Although some important insights can be obtained by theoretical works, complicated interactions between gas and stars and highly nonlinear behaviors of gasdynamics make pure mathematical analyses impractical to trace the disk evolution. With the advances in computing power and the development of new numerical techniches, we are now in a good position to tackle these questions outlined in the previous sections on computers. Before complicating the disk with different physics, one needs to initialize a well-controlled three-dimensional disk in order to have conclusive results. We mainly learn two things from Narayan & Jog (2002): (i) galactic disks are roughly in equilibrium state in the vertical direction (ii) to model a composite disk including dark matter, stars and gas, one needs to build the joint potential self-consistently. In Chapter 2, we devise a simple, effective method to compute the three-dimensional density and velocity structure of an isothermal gas disk in hydrodynamic equilibrium in the presence of arbitrary external potential. We implement this method with the adaptive mesh refinement magnetohydrodynamics code RAMSES (Teyssier 2002). The three-dimensional disk stability and the swing amplification are carefully examined and compared with the theoretical predictions.

In Chapter 3, we search for the evidences of intergalactic gas accretion for the disk galaxy, M83. We essentially improve the Fourier analysis method proposed by Schoenmakers et al. (1997) to evaluate the possible presence and strength of any radial flow for M83. We combine the high resolution interferometric HI map from THINGS with single dish data from the 100-m radio telescope of the Max-Planck-Institut fur Radioastronomie at Effelseberg (Huchtmeier & Bohnenstengel 1981) in order to obtain a complete census of the atomic hydrogen across M83. Evidences of gas accretion through filaments, i.e., cold mode, are examined kinematically.

In Chapter 4, we quantify the impacts of spiral density waves on gas motions. It has been long proposed that spiral density waves is one of the mechanisms contributing turbulent energy into the gas (Wada & Koda 2004). The efficiency of this process and how it happens is not well understood and quantified. On the one hand, the luminous arms seem to suggest that density wave is triggering the star formation by compressing sub-critical clouds into super-critical ones. On the other hand, density-wave driven turbulence may regulate the process of star formation. We measure the hydrodynamical velocity dispersion along the line-of-sight and compare our results with observations from THINGS. We address how efficient the gas is transported toward the center of galaxies by redistributing angular momentum. We quantify the radial velocity as a function of radius. We demonstrate that vortensity conservation which has been used for theoretical and obervational studies (Balbus 1988; Shetty et al. 2007) does not apply to a flow which has curved shocks. We semi-analytically quantify the creation of vortensity due to shocks and compare it with the intrinsic disk vortensity. In addition, we investigate the origin of spurs and how the retrograde motion with respect to the galaxy rotation results.

In Chapter 5, we summarize the results and their implications. Possible extensions of these works will be discussed.

Chapter 2

Equilibrium Initialization and Stability of Three-Dimensional Gas Disks

2.1 Introduction

The stability of gas disks plays an important role in governing the structure of disk galaxies and in regulating their star formation rate. Although important insights can be obtained using perturbation theory (Toomre 1964; Lin & Shu 1964; Rafikov 2001), the onset of stability and its impact on the star formation and evolution of gas disks is best studied using hydrodynamical simulations. These can follow the non-linear behavior of the system, which cannot be addressed by linear analysis. With the recent advances in computing power and the development of new numerical techniques, we are now in a good position to treat a three-dimensional, isolated galaxy self-consistently.

However, in order for a stability analysis to be meaningful and reliable, it is of paramount importance that one can specify equilibrium initial conditions. After all, if the initial disk is not in equilibrium, its relaxation during the first time-steps of the simulation may trigger instabilities that are of little relevance for our understanding of the stability of disk galaxies. Unfortunately, no analytical solution is known for the density, velocity field and temperature of a three-dimensional gas disk in hydrostatic equilibrium in the external potential of a dark matter halo and/or a stellar disk. Consequently, previous hydrodynamical simulations have either started from non-equilibrium initial conditions, or have resorted to iterative techniques to set-up the initial conditions, at the cost of having little control over the resulting equilibrium configuration. In this Chapter we present a new method that allows one to compute the density and velocity structure of a realistic, isothermal, three-dimensional gas disk in hydrostatic equilibrium in an abritrary external potential.

Hydrostatic equilibrium implies a balance between gravity and pressure. Gravity includes the self-gravity of the disk plus that of external components (i.e. dark matter halo, bulge, stellar

disk, etc), while the pressure is given by an equation of state $p = p(\rho_g, T)$, with p being the gas pressure, ρ_g the gas density and T the temperature. The challenge is to find a ρ_g, T and the velocity field, $\vec{v}$, such that the system is self-consistent (i.e., obeys the Poisson equation) and in hydrostatic equilibrium.

In the case of an isothermal, axisymmetric, perfectly self-gravitating disk (i.e., no external potential), the equilibrium disk has a sech^2 distribution (Spitzer 1942) in the vertical direction, with a scale-height that is proportional to $\sqrt{c_s^2/\rho_g(R, z = 0)}$, where c_s is the sound speed. Here, cylindrical coordinates, (R, ϕ, z), are used to describe the density field. This immediately shows that since $\rho_g(R, z = 0)$ is typically a decreasing function of radius, one generally expects the scale-height to be a function of R. In particular, in the case of a globally isothermal disk, the sound speed $c_s^2 \propto T$ is constant in space, giving rise to a flaring disk, i.e., the scale-height increases with increasing R (Narayan & Jog 2002, hereafter NJ02; Agertz et al. 2009). Alternatively, if we want to initialize a disk with a constant scale-height, a radial temperature gradient needs to be introduced. Tasker & Bryan (2006) initialize their disks to be isothermal and to have a constant scale-height. As indicated above, this cannot be an equilibrium configuration. Consequently, the disk is expected to experience an unavoidable relaxation process which makes the initialization not well-controlled and might potentially contaminate the physics, e.g., star formation, gas dynamics etc., of interest. Agertz et al. (2009) set-up their isothermal disks based on the local total surface density of gas plus dark matter. Although the scale-height of their initial disk changes with radius, the local total surface density is not defined in a mathematical way and therefore elusive. In addition, their surface density does not follow an exponential profile.

An important assumption underlying Spitzer's analysis is that the radial variation in the potential is negligible compared to that in the vertical direction. This assumption is supported by observation that disks typically have vertical scale-heights that are an order of magnitude smaller than their radial scale-length (van der Kruit & Searle 1981b,a). A well studied example is the Milky Way, whose scale-height is less than 200 pc for the cold gas (Jackson & Kellman 1974; Lockman 1984; Sanders et al. 1984; Wouterloot et al. 1990; see also Narayan & Jog 2002) and roughly 300 pc for the stars in the Solar neighborhood (Binney & Tremaine 2008; Kent et al. 1991), compared to a radial scale-length of ~ 3.5 kpc. Throughout this Chapter we therefore follow Spitzer and consider disks to be 'thin', allowing us to treat their radial and vertical structure separately. Hence, we caution that our method is not valid for thick disk structures. However, since we are mainly concerned with cold gas disks in this Chapter, this restriction is of little importance.

Springel et al. (2005) introduce a flexible solution for initializing a gas disk self-consistently. Basically, they solve Eq. (2.2), Eq. (2.3) and Eq. (2.24) (see Section 2.2) iteratively. First, they deploy a number of particles (say, $2048 \times 64 \times 64$) on a distorted grid structure in the radial, the azimuthal and the vertical directions. Unlike the live particles, these particles are simply used as markers for mass distribution. Second, they compute the joint total potential and the resulting

force field numerically with a hierarchical multipole expansion based on a tree code. Third, given the potential just computed, integrating Eq. (2.2) for a given midplane volume density, $\rho_{\rm g}(R, z = 0)$, gives the vertical structure of density. Fourth, adjust the midplane volume density to fulfill Eq. (2.24). Repeat the procedure between the second step and the fourth until the result converges.

Although this description is quite general and flexible, for several reasons, this is not commonly used in the grid-based codes which are featured with adaptive-mesh refinement (AMR). The first and also the most fundamental one is that the grid structure is normally unknown before we actually initialize the disk. Except the uniform-grid initialization, the grid structure is automatically generated based on the criterion for refinement. Second, for a fully parallelized code, the initial data is distributed over different processors and memory storages. This means that the data exchange between processors is necessary in order to fully compute the joint total potential. The situation becomes even more technically challenging when initializing with AMR. Third, The vertical structure of the gas disk depends only on the vertical potential difference (see Eq. (2.7) and Eq. (2.9) below). A description of the equatorial potential is enough for specifying the velocity field (See Eq. (2.13), Eq. (2.29) and the results shown in Section 2.3). In general, given the density distribution computed by the methods introduced in Section 2.2.2 together with the conclusion in Section 2.2.1, we are allowed to acquire the exact velocity field by Eq. (A.17) in Casertano (1983). Fully solving the Poisson equation becomes not necessary. Fourth, initializing a disk over distributed memories allow us to deal with a larger data set which cannot be fully contained in a single memory storage.

We propose a simple but very effective way of initializing a three-dimensional gas disk. This method can be easily incorporated into any existing code based on either a Lagrangian or Eulerian approach. No data exchange between processors is needed. Vertical density profile is obtained self-consistently without solving the full Possion equation. We implement these ideas with the adaptive mesh refinement magnetohydrodynamics code RAMSES (Teyssier 2002) and apply our concepts to probe the onset of the disk instability. We modify the dispersion relation for the infinitesimally thin disk (Lin & Shu 1964)to be able to treat thick disks (Goldreich & Lynden-Bell 1965; Kim & Ostriker 2002b, 2006; Shetty & Ostriker 2006; Lisker & Fuchs 2009). The threshold value $Q_{\rm th}$ is then obtained semi-analytically. Previous studies on this subject are either focused on a small patch of a galaxy (2D/3D: Kim & Ostriker 2002b) or are globally two-dimensional but with the reduction of gravity included in the governing equations (Shetty & Ostriker 2006). In this Chapter, we revisit the subject as a test of our fully three-dimensional isolated galaxy models. Models with or without stellar potential are investigated.

Galactic disks are comprised of stars and gas. Both components are coupled to each other via the Poisson equation. Since the stellar disk dominates the mass budget within the luminous disk, its presence has great impact on the scale-height of the gas disk as described in NJ02. A balanced

initial condition depends not only on the correct vertical structure but also on the correct rotation velocity. To specify the rotation velocity needed, the mass enclosed within a certain radius must be under control. Although it is common practice to specify the functional form of the volume densities of 3D disks, we show that because of the flaring disk this typically results in a surface density profile that contains a central 'hole' (Agertz et al. 2009). This problem can be trivially avoided by specifying the desired surface density profile instead. We show that the corresponding volume density can easily be obtained using a simple iterative scheme. The surface density of the total gas ($HI + H_2$) from observation (Leroy et al. 2008) typically follows an expotential profile in disk galaxies. This profile gives an analytic description of the total mass enclosed within a radius as well as a reasonable approximation for velocity field as shown by Eq. (2.29) below (Binney & Tremaine 2008).

Describing the stellar disk with a fixed background potential is at best an approximation to reality. The interaction between live stellar disk and gas can potentially destabilize the system (Rafikov 2001; Li et al. 2005b,a, 2006; Kim & Ostriker 2007). After all, the gas is cold compared to the stellar disk and has highly non-linear response to the asymmetric stellar potential. The gravitational interplay between the collisionless stars and dissipative gas is important for a number of key questions in galactic dynamics. For example, what is the physical origin of grand design spirals? Or what initiates and regulates the formation of stars? Having access to well-controlled initial and environmental conditions is a prerequisite to discovering their causes.

This Chapter is organized as follows. The ideas of initializing a gas disk are outlined in Section 2.2. Details of the simulation parameters and test runs are described in Section 2.3. Axisymmetric instability of the disk is revisited in Section 2.4. The self-induced spirals due to swing amplification will be discussed in Section 2.5. A brief summary and the possible extension of this work is put in Section 2.6.

2.2 Formulation of Equations

In this Section, we develop the required relations and equations to immerse a 3D gas disk in a preexisting static potential. Assuming that the gas disk and the preexisting potential share the same symmetry axis, cylindrical coordinates, (R, ϕ, z), are adopted to formulate the dynamics of the system. Axial-symmetry enables us to discard the terms describing the variation in azimuthal direction, i.e., $\partial/\partial\phi = 0$. A gas disk which is in detailed balance should fulfill the following

equations:

$$\frac{1}{\rho_{\rm g}}\frac{\partial p}{\partial R}+\frac{\partial \Phi}{\partial R} = \frac{V_{\rm rot}^2}{R}, \tag{2.1}$$

$$\frac{1}{\rho_{\rm g}}\frac{\partial p}{\partial z}+\frac{\partial \Phi}{\partial z} = 0, \tag{2.2}$$

with $\rho_{\rm g}$, p, $V_{\rm rot}$ and Φ being the volume density of the gas, the gas pressure, the azimuthal rotation velocity ("rotation velocity" in short) and the joint total potential. Equation (2.1) describes that the gravitational pull in radial direction is counterbalanced by the centrifugal force and the pressure gradient. Equation (2.2) states that hydrostatic equilibrium along the symmetry axis, the z-direction, is achieved by the balance between vertical pull of the gravity and the pressure gradient in z.

To make the system self-consistent, the Poisson equation must be involved:

$$\nabla^2\Phi = 4\pi G(\rho_{\rm g}+\rho_{\rm DM}+\rho_{\rm s}), \tag{2.3}$$

with G, $\rho_{\rm DM}$ and $\rho_{\rm s}$ being the gravitational constant, and the volume density of dark matter and stars. The total potential is comprised of the contributions from the dark matter halo, the stellar disk and the self-gravity of the gas, i.e., $\Phi = \Phi_{\rm DM}+\Phi_{\rm s}+\Phi_{\rm g}$. In addition, the ideal gas law provides the link between the gas density, the gas temperature and the gas pressure:

$$p = \rho_{\rm g}(\gamma-1)e(T), \tag{2.4}$$

where γ represents the ratio of the heat capacities (adiabatic index), e the specific internal energy and T the gas temperature. In the case of an ideal gas, the specific internal energy depends only on temperature, and is given by

$$e = \frac{1}{\gamma-1}\frac{k_{\rm B}T}{\mu m_{\rm p}}, \tag{2.5}$$

with $k_{\rm B}$ being the Boltzmann's constant, μ the atomic weight and $m_{\rm p}$ the mass of a proton. However, to close the set of equations, we should either invoke the energy equation or an equation of state (EoS), which will be used to evolve the system.

A disk which is in hydrodynamic equilibrium should stay in its original state if we evolve the disk with the same equation of state which is used to set-up the disk. The numerical results throughout this Chapter are based on the isothermal equation of state, i.e.,

$$p = c_{\rm s}^2\rho_{\rm g}, \tag{2.6}$$

with $c_{\rm s}$ being the sound speed, a temporal and spatial constant. Equations (2.1) to (2.6) then form the basis of our discussion. In this Chapter, all the disks are in detailed equilibrium with

the isothermal EoS. If those disks are adopted to evolve with a cooling function or a polytropic EoS, we can make sure any change in temperature or dynamics is purely caused by a cooling or a heating source.

For a polytropic gas, $p = K\rho_{\rm g}^{\Gamma}$. with Γ and K being constant, integrating Eq. (2.2) gives:

$$\rho_{\rm g}(R,z) = \rho_{\rm g}(R,z=0)\left[1 - \frac{\Gamma-1}{c_{\rm s}^2(R,z=0)}\Phi_z(R,z)\right]^{\frac{1}{\Gamma-1}}, \tag{2.7}$$

where $\Phi_z(R,z) = \Phi(R,z) - \Phi(R,z=0)$ defines the vertical potential difference. We have used the fact that $c_{\rm s}^2 \equiv \partial p/\partial\rho_{\rm g} = K\Gamma\rho_{\rm g}^{\Gamma-1}$ when approaching Eq. (2.7). Note that given $\Gamma \neq 1$, the internal energy has the following relation:

$$e(T) = \frac{K\rho_{\rm g}^{\Gamma-1}}{\gamma-1}. \tag{2.8}$$

Combining Eq. (2.5) and Eq. (2.8) gives the temperature field as a function of position if the gas disk is initialized with a non-isothermal EoS. As a special case, when $\Gamma \to 1$, Eq. (2.7) then converges to a form for the isothermal gas:

$$\rho_{\rm g}(R,z) = \rho_{\rm g}(R,z=0)\exp\left(-\frac{\Phi_z(R,z)}{c_{\rm s}^2}\right). \tag{2.9}$$

As we can see from Eq. (2.7) and Eq. (2.9), the vertical structure of gas disk depends on the gas properties in the midplane and the vertical potential difference.

To fully characterize a gas disk which is in detailed balance, we need to specify the velocity, the density and the temperature at every location in the beginning of the simulation. In the following sub-sections we study the general properties of the velocity and density field, which allows us to devise a simple, but effective method to initialize a 3D gas disk in hydrostatic equilibrium.

2.2.1 Azimuthal Rotation Velocity

In this sub-section, we treat the azimuthal rotation velocity as generally as possible. To make the notation concise, we drop the subscript of gas density, $\rho_{\rm g}$, and restore the subscript after this sub-section. Without further assumption, integrating Eq. (2.2) from 0 to z gives:

$$\int_0^z \frac{1}{\rho}\frac{\partial p}{\partial z}{\rm d}z = -\Phi_z(R,z). \tag{2.10}$$

By integrating Eq. (2.10) in parts, we have:

$$\frac{p(R,z)}{\rho(R,z)} = \left.\frac{p(R)}{\rho(R)}\right|_{z=0} - \int_0^z \frac{p}{\rho^2}\frac{\partial\rho}{\partial z}{\rm d}z - \Phi_z(R,z). \tag{2.11}$$

Inserting Eq.(2.11) into (2.1), we get (see Appendix A.1 for further details):

$$\begin{aligned}\frac{V_{\rm rot}^2(R,z)}{R} &= \frac{1}{\rho}\frac{\partial p}{\partial R} + \frac{\partial \Phi(R,z)}{\partial R} \\ &= \left.\frac{1}{\rho}\frac{\partial p}{\partial R}\right|_{z=0} + \left.\frac{\partial \Phi(R)}{\partial R}\right|_{z=0} \\ &- \int_0^z \left\{\left(\frac{\partial \rho}{\partial z}\right)\frac{\partial}{\partial R}\left(\frac{p}{\rho^2}\right) - \left(\frac{\partial \rho}{\partial R}\right)\frac{\partial}{\partial z}\left(\frac{p}{\rho^2}\right)\right\} {\rm d}z. \end{aligned} \tag{2.12}$$

Equation (2.12) shows that the rotation velocity is independent of height above or below the midplane so long as the integral vanishes. It is evident that gas with a barotropic equation of state, i.e., $p(\rho_{\rm g})$, fulfills this requirement. In addition, for an initially constant temperature (T is everywhere the same in the beginning) disk, the initial pressure is a function of volume density only and therefore the integral becomes zero. In this case, equation (2.12) can be simplified further:

$$V_{\rm rot}^2(R,z) = R\left.\frac{\partial \Phi}{\partial R}\right|_{z=0} + (\gamma-1)e\left.\frac{\partial \ln \rho}{\partial \ln R}\right|_{z=0}. \tag{2.13}$$

Equation (2.13) states that the process of specifying the initial velocity in 3D comes down to knowing the rotation velocity in the equatorial midplane.

2.2.2 Density Distribution

From now on, to avoid confusion, we restore the subscript for the gas density. To proceed further, we consider the gas layer to be a very thin structure embedded in a static potential contributed by the background spherical dark matter and the stellar disk. Because the gas disk is observationally thin we neglect the radial variation compared to the vertical one (i.e., $|(\partial/\partial R(R\partial\Phi_{\rm g}/\partial R))/R| \ll |\partial^2\Phi_{\rm g}/\partial z^2|$). In Appendix A.5 we show that this is a valid assumption for realistic gas disks. For an axisymmetric thin disk, the Poisson equation then reduces to (Binney & Tremaine 2008):

$$\frac{{\rm d}^2\Phi_{\rm g}}{{\rm d}z^2} = 4\pi G\rho_{\rm g}. \tag{2.14}$$

with $\Phi_{\rm g}$ being the potentials contributed by the gas. In the following, we focus only on disks with initially constant temperature, i.e., the rotation velocity required for equilibrium has no dependence on the height above or below the midplane.

Density Method

Differentiation Eq. (2.2) with respect to z and inserting Eq. (2.14) leads to a second-order non-linear differential equation:

$$\frac{\mathrm{d}^2 p}{\mathrm{d}z^2} - \frac{1}{\rho_\mathrm{g}}\frac{\mathrm{d}\rho_\mathrm{g}}{\mathrm{d}z}\frac{\mathrm{d}p}{\mathrm{d}z} + \rho_\mathrm{g}(4\pi G\rho_\mathrm{g} + \frac{\mathrm{d}^2\Phi_\mathrm{s}}{\mathrm{d}z^2} + \frac{\mathrm{d}^2\Phi_\mathrm{DM}}{\mathrm{d}z^2}) = 0, \tag{2.15}$$

with Φ_s and Φ_DM being the potentials contributed by the stellar disk and the dark matter, respectively. So far, Eq. (2.15) is still general with respect to any kind of equation of state. However, a single equation with two unknowns p and ρ_g is not solvable. To continue with Eq. (2.15), in this sub-section, we assume that the gas is barotropic, i.e., $p(\rho_\mathrm{g})$. Given density distributions of stars, the dark matter and the boundary conditions in the midplane:

$$\rho_\mathrm{g}(R, 0) = \rho_0(R) \text{ and } \frac{\mathrm{d}\rho_\mathrm{g}}{\mathrm{d}z} = 0, \tag{2.16}$$

equation (2.15) can be solved by numerical integration, e.g., using the Runge-Kutta method. For a single-component, self-gravitating, locally isothermal disk ($c_\mathrm{s}(R)$ can be a function of radius), Eq. (2.15) has an exact solution:

$$\rho_\mathrm{g}(R, z) = \rho_0(R)\mathrm{sech}^2(z/h), \tag{2.17}$$

with $\rho_0(R)$ being the gas volume density in the midplane, $h = \sqrt{c_\mathrm{s}^2/2\pi G\rho_0}$ the scale-height and c_s the local isothermal sound speed. According to Eq. (2.17) and since the midplane volume density, $\rho_0(R)$, generally decreases with radius, to keep the scale-height a constant, the sound speed and therefore the temperature must be a function of radius.

Equation (2.15) is the simplified version of the formula derived by NJ02 (see also Kim & Ostriker 2002b), where they investigated the vertical structure in a gravitationally coupled, multi-component galactic disk. It is important to notice that all calculations can be done locally without the need of exchanging information between processors and therefore greatly reduces the complexity of coding.

In principle Eq. (2.15) allows one to compute the density of the gas such that the disk initially is in hydrostatic equilibrium. The actual implementation using Eq. (2.15) does not guarantee the positivity of the density. In particular, at large radii $\rho_\mathrm{g}(R, z)$ is typically close to zero, and small errors due to the numerical integration often yield negative densities. This problem is especially relevant when using the adaptive-mesh refinement techniques.

Initializing a gas disk with AMR usually starts with the coarsest grid. A natural selection of the integration step is the cell size. Then a problem immediately rises when solving Eq. (2.15) to specify the volume density. Supposing that the cell size is much larger than the scale-height of

the gas disk, the errors introduced by the coarse integration may lead to negative densities on the outskirt of the computation domain. One might think the integration can be done by using either adaptive integration intervals or simply a fixed integration interval which is much smaller than the cell size. However, the improvements only guarantee the convergence of the solution not the positivity. Nevertheless, because of the generality of Eq. (2.15), density method is still valuable for semi-analytic research.

Potential Method

In this sub-section, we develop another route for specifying the density distribution. We stress that the following derivation is only applicable to initially isothermal disks. With this constraint, integrating Eq. (2.2) gives:

$$\rho_{\rm g}(R,z) = \rho_0(R)\exp\left(-\frac{\Phi_z(R,z)}{(\gamma-1)e}\right). \tag{2.18}$$

Combining Eq. (2.14) and Eq. (2.18), a second-order non-linear equation for the vertical potential difference of gas is obtained:

$$\frac{{\rm d}^2\Phi_{{\rm g},z}}{{\rm d}z^2} = 4\pi G\rho_0(R)\exp\left(-\frac{\Phi_z(R,z)}{(\gamma-1)e}\right). \tag{2.19}$$

Given the analytic forms of $\Phi_{\rm DM}$ and $\Phi_{\rm s}$ the only unknown is the potential difference of gas, $\Phi_{{\rm g},z} = \Phi_{\rm g}(R,z) - \Phi_{\rm g}(R,z=0)$. Similar to the density method, given the boundary conditions $\rho_0(R)$, $\Phi(R,z=0)$ and ${\rm d}\Phi(R,z=0)/{\rm d}z = 0$, numerical integration can be applied to solve Eq. (2.19). By inserting Φ_z obtained by integrating Eq. (2.19) into Eq. (2.18), the density distribution is acquired. Notice that what really matters to us is the potential difference, not the absolute value. This means the value of $\Phi_{\rm g}(R,z=0)$ can be an arbitrary constant, although we do know the values of $\Phi_{\rm DM}(R,z=0)$ and $\Phi_{\rm s}(R,z=0)$.

The merit of this formulation is evident, the occurrence of negative density is avoided by Eq. (2.18). Tiny errors in the potential difference will not do any harm to the positivity of the gas density. Numerical experiments show that in normal cases in which both the density method and potential method work, the solutions are consistent.

At a given radius, R, solving Eq. (2.19) only provides us with information about the potential difference, $\Phi_z(R,z)$. However, a useful byproduct of the potential method is that it is possible to acquire a good approximation of the total potential by:

$$\Phi_{\rm g}(R,z) = \Phi_{\rm g}(R,z=0) + \Phi_{{\rm g},z}(R,z), \tag{2.20}$$

as long as we know the potential in the midplane, $\Phi_{\rm g}(R,z=0)$. Equation (2.20) is an approximation because the use of Eq. (2.19) is based on the reduced Poisson equation Eq. (2.14) in

which the variation in radial direction is ignored. The gradient of the potential $\Phi_{\rm g}(R, z = 0)$ determines the velocity field required while the vertical potential difference $\Phi_{{\rm g},z}(R, z)$ gives the vertical structure of the disk. In principle, the radial force, which is associated with $\Phi_{\rm g}(R, z = 0)$, in the equatorial plane for an axially symmetric density distribution can be evaluated precisely by the equation (A.17) in Casertano (1983). This allows us to obtain the total potential without fully solving the Poisson equation. In practice, if the initialization is performed with multi-node clusters, each node only keeps part of the information about the density distribution, data exchange with AMR itself is technically challenging. In Section 2.3, for an exponential disk, the numerical results will show that the use of Eq. (2.29) is a good approximation for most of our interests. The corresponding $\Phi_{\rm g}(R, z = 0)$ associated with Eq. (2.29) can be found in the book by Binney & Tremaine (2008), Eq. (1.164a).

Equation (2.20) is useful, because involving the total potential into the formulation is an important step for self-consistently building up the combined disks comprised of a live stellar disk and a gas disk. Extension to the work of Shu (1969), Kuijken & Dubinski (1995, hereafter, KD95) develop a self-consistent disk-bulge-halo model for galaxies. The distribution function built by Eq. (6) in KD95 involves the potential differences Φ_z and $\Phi(R, 0) - \Phi(R_{\rm c}, 0)$, with $R_{\rm c}$ the radius of the guiding center. The potential method presented here can be naturally incorporated into the framework of KD95. Therefore, in this Chapter, all the disks are initialized by the potential method.

Exponential Disk

Some studies have assumed that the midplane density of a 3D gas disk has an exponential form (Tasker & Bryan 2006; Agertz et al. 2009). However, as we now demonstrate, in general this results in a surface density distribution that peaks at a specific non-zero radius, giving rise to a ring-like feature. We assume a gas disk with the popular sech^2 vertical profile:

$$\rho_{\rm g}(R, z) = \rho_{\rm c} \exp(-R/R_{\rm d}) \mathrm{sech}^2\left(\frac{z}{h(R)}\right), \tag{2.21}$$

with $\rho_{\rm c}$ being the central volume density, $R_{\rm d}$ the disk scale-length and $h(R)$ the scale-height as a function of radius. The surface density then reads:

$$\Sigma(R) = \int_{-\infty}^{\infty} \rho_{\rm g}(R, z) {\rm d}z = 2\rho_{\rm c} \exp(-R/R_{\rm d}) h(R). \tag{2.22}$$

Based on Eq. (2.22), we measure the scale-height of a disk at certain radius by $h(R) = \Sigma(R)/(2\rho_0(R))$. The extrema of the surface density can be evaluated by taking the derivative to Eq. (2.22):

$$\frac{{\rm d}\Sigma(R)}{{\rm d}R} = 2\rho_{\rm c} \exp(-R/R_{\rm d}) \left(\frac{{\rm d}h(R)}{{\rm d}R} - \frac{h(R)}{R_{\rm d}}\right) = 0. \tag{2.23}$$

We Suppose that the disk is linearly flaring, i.e., $h(R) = h_0 + R/R_\mathrm{h}$, with h_0 being the minimum scale-height of the disk and R_h a factor controlling the degree of flaring. The peak of the surface density then locates at $R_\mathrm{peak} = R_\mathrm{d} - h_0 R_\mathrm{h}$. Whenever the R_peak is positive, we get a ring in surface density. However, a ring in the surface gas density is not commonly seen in a real disk galaxy. An exponential profile in the total gas is prevalent in disk galaxies (Leroy et al. 2008).

In order to avoid this feature, it is advantageous to specify the actual surface density of the disk, rather than its midplane density. In the case of the exponential profile, the surface density reads:

$$\Sigma(R) = \Sigma_0 \exp\left(-R/R_\mathrm{d}\right) = \int_{-\infty}^{\infty} \rho_\mathrm{g}(R, z)\mathrm{d}z, \tag{2.24}$$

with Σ_0 being the surface density in the galactic centre. Combining Eq. (2.24) and Eq. (2.18), the volume density in the midplane can be expressed as:

$$\rho_0(R) = \frac{\Sigma_0 \exp\left(-R/R_\mathrm{d}\right)}{\int_{-\infty}^{\infty} \exp\left(-\Phi_z/[(\gamma-1)e]\right)\mathrm{d}z}. \tag{2.25}$$

It shows that the correct volume density in the midplane for the desired surface density profile can be obtained iteratively. Given a initial guess for $\rho_0(R)$, Φ_z is evaluated via Eq. (2.19) and also the integral appears in Eq. (2.25). One needs to iterate between Eq. (2.19) and Eq. (2.25). However, depending on the quality of the initial guess, convergence can be reached very fast. For instance, with the initial guess being $\rho_0(R) = \Sigma_0 \exp(-R/R_\mathrm{d})$, a six-time iteration already gives us a reasonable exponential disk.

We pursue the exponential disk for several reasons. One is simply because it is commonly seen in disk galaxies. Another is that we have a better control of the total mass. As we can see, if we specify the midplane volume density instead of the surface density, we do not exactly know the total mass until we finish the integration. Without knowing the total mass in advance, evaluating the circular velocity contributed by the self-gravity will not be a trivial task. Nevertheless, in principle, any profile of the surface density can be achieved simply by the process introduced in this sub-section.

2.3 Implementation and Tests

2.3.1 Simulation Parameters

In this Section, we test the ideas outlined in the previous Section. We implement the method in the AMR-code RAMSES (Teyssier 2002). RAMSES uses grid-based Riemann-solvers for the magneto-hydrodynamics (MHD) and particle-mesh (PM) technique for the collisionless physics.

Run	T (K)	$M_s(M_\odot)$	Figure
Gas0	4×10^4	-	(2.1),(2.2),(2.3)
Gas1	2×10^4	-	(2.4),(2.5)
Gas2	1×10^4	-	(2.4),(2.5),(2.8)
Gas3	9×10^3	-	(2.4),(2.5)
Gas4	8×10^3	-	(2.4),(2.5)
GasStar1	7×10^3	4×10^{10}	(2.6),(2.7),(2.8)
GasStar2	6×10^3	4×10^{10}	(2.6),(2.7)
GasStar3	5×10^3	4×10^{10}	(2.6),(2.7)
GasStar4	4×10^3	4×10^{10}	(2.6),(2.7)

Table 2.1: Models' Parameters. All disks have a gas mass of $10^{10}M_\odot$.

It has a fully parallelized Poisson solver with periodic boundary conditions, which we use for this Chapter. Gas disks which are initialized isothermally with an exponential surface density of a scale-length of 3.5 kpc and a total mass of $10^{10}M_\odot$ are embedded in a static potential. An isothermal equation of state is used to evolve the disks throughout this Chapter.

The tests are mainly divided into two groups, one group is evolved with a static stellar potential (models with the prefix GasStar), the other without (models with the prefix Gas). Gas1 to Gas4 are M33-like gas-rich galaxies, while GasStar1 to GasStar4 are more similar to the Milky-Way. The main parameters of the models are listed in Table 2.1. The size of the computational domain is 250 kpc on a side. Up to 12 levels of refinement are used for those runs without stellar potential, and 13 levels for the other group, i.e., the corresponding highest spatial resolutions are about 60 pc and 30 pc, respectively.

The volume density of the halo is described by the NFW profile (Navarro et al. 1997):

$$\rho_{\rm DM}(r) = \frac{M_{200}}{4\pi f(c) r_{200}} \frac{cx}{r^2(1+x)^2}, \tag{2.26}$$

with the Virial mass $M_{200} = 10^{12}M_\odot$, $x = rc/r_{200}$, concentration parameter $c = 12$, distance $r = \sqrt{R^2+z^2}$, Virial radius $r_{200} = 213$ kpc and $f(c) = \ln(1+c) - c/(1+c)$. The Virial radius ($r_{200}$) is a radius within which the averaged matter density is 200 times the critical density.

The density distribution of the stellar disk reads (Miyamoto & Nagai 1975; Binney & Tremaine 2008):

$$\rho_s(r) = \left(\frac{b^2 M_s}{4\pi}\right) \frac{aR^2 + (a+3\sqrt{z^2+b^2})(a+\sqrt{z^2+b^2})^2}{\left[R^2 + (a+\sqrt{z^2+b^2})^2\right]^{5/2} (z^2+b^2)^{3/2}}, \tag{2.27}$$

with $M_s = 4 \times 10^{10} M_\odot$ being the mass of the stellar disk, $a = 3.5$ kpc and $b = 0.2$ kpc the shape parameters.

In light of the result drawn from Section 2.2.1, for an initially constant temperature setup, we only need to know the circular velocity in the midplane for initializing the velocity field. The rotation velocity, V_{rot}, is decomposed into four components:

$$V_{rot}^2 = V_{DM}^2 + V_s^2 + V_g^2 + V_p^2, \tag{2.28}$$

where V_{DM}, V_s, V_g are the circular velocities corresponding to the dark matter halo, the stellar disk and the gas disk, and V_p denotes the contribution due to the pressure gradient.

In this Chapter, we have the analytic form for V_{DM} and V_s. For the contribution from the gas disk and pressure gradient, we take the approximation for an infinitesimally thin disk with exponential surface density as described in Eq. (2.24). We set:

$$V_g^2(R) = 4\pi G \Sigma_0 R_d y^2 [I_0(y)K_0(y) - I_1(y)K_1(y)] \tag{2.29}$$

$$V_p^2(R) = (\gamma - 1) e \left. \frac{\partial \ln \rho}{\partial \ln R} \right|_{z=0}, \tag{2.30}$$

with $y = R/(2R_d)$, I_0, K_0, I_1 and K_1 being the modified Bessel functions of the first and second kinds of zeroth/first-order, respectively. Equation (2.30) derives from the second term of Eq. (2.13). However, contribution from pressure gradient in the midplane can only be evaluated after the gas disk is set up. Note that for an exponential disk, surface and volume densities decrease with radius and hence V_p^2 is negative.

2.3.2 A Stable Disk

To demonstrate that the disk built by the potential method described in Section 2.2 is in detailed equilibrium, we start with a stable equilibrium disk in model Gas0. In this test, the stellar disk is deliberately removed. Without the dynamical support from the stellar disk, the self-gravity of the gas plays the dominant role in determining the vertical structure of the disk and provides a not negligible contribution to the rotation velocity.

Figure 2.1a decomposes the rotation curve into the different contributions by the halo, the gas and the pressure gradient. Note that the forces of the self-gravity and the pressure gradient are in opposite sense, the self-gravity pulls matter inwards while the pressure gradient pushes outwards. In this figure, V_p is shown in its absolute value. If we ignore the pressure gradient, the disk would rotate too fast and gradually drift outward. Figure 2.1b shows the conventional Toomre's Q defined by:

$$Q = \frac{c_s \kappa}{\pi G \Sigma_g}. \tag{2.31}$$

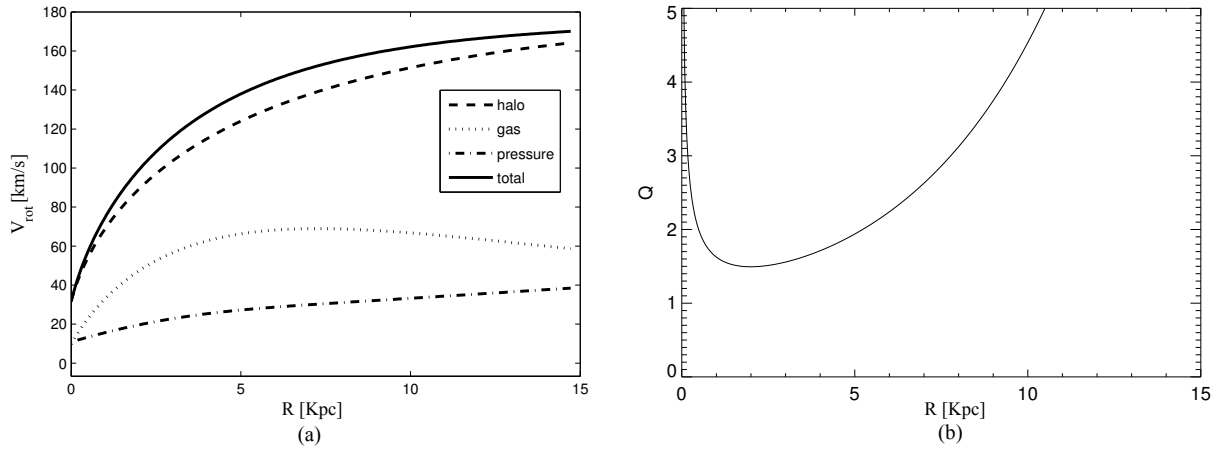

Figure 2.1: Model Gas0: (a) The total rotation velocity (solid) and contributions from dark matter halo (dashed), gas (dotted) and gas pressure (dash-dotted). Note that we plot the absolute value of the pressure gradient to have positive values for the direct comparison. It should be in opposite sense to the gravity. In this model contributions from the gas self-gravity and the pressure gradient is not negligible. (b) The Q value of model Gas0 as a function of radius as defined by Eq. (2.32). The Q is well above the threshold value $Q_{\rm th} = 1$, thus the disk is expected to be stable. No structure should develop with time.

with κ being the epicyclic frequency. It shows that the Q is well above $Q_{\rm th} = 1$, the threshold value for stability, at all radii. The disk is hot enough to keep the disk stable and no structure should develop with time.

We let the disk evolve for 1.6 Gyrs (four orbits for the gas at 10 kpc) and check how well the disk properties are kept. Figure 2.2a presents the evolution of the surface density and the rotation curve. The solid lines represent the initial states and the diamond symbols are the status after an evolution of 1.6 Gyrs. The surface density is obtained by projecting along the symmetry axis and the rotation curve is evaluated by the mass-weighted circular velocity, $\overline{v}_{\rm rot}(R) = \int \rho_{\rm g}(R,z) v_{\rm rot}(R,z) {\rm d}z / \Sigma_{\rm g}(R)$. Although a small amount of mass accretes onto the very central part of the disk, overall the surface density and the rotation curve are kept very well. Mass accretion into the center seems unavoidable for a Cartesian-grid code mainly because too small a number of cubic cells is used to mimic the circular motion in the centre. This accretion will be eventually halted by the pressure gradient built by the accumulating material.

Figure 2.2b shows the evolution of the scale-height. The solid line represents the initial state and the dotted line the evolution after 1.6 Gyrs. Upon closer inspection we find that the disk undergoes a very small amount of mass-redistribution in the radial direction, which we believe to be a consequence of our two approximations when initializing the disk. One is from the reduced Poisson equation, Eq. (2.14), and the other is from the use of Eq. (2.29). Equation

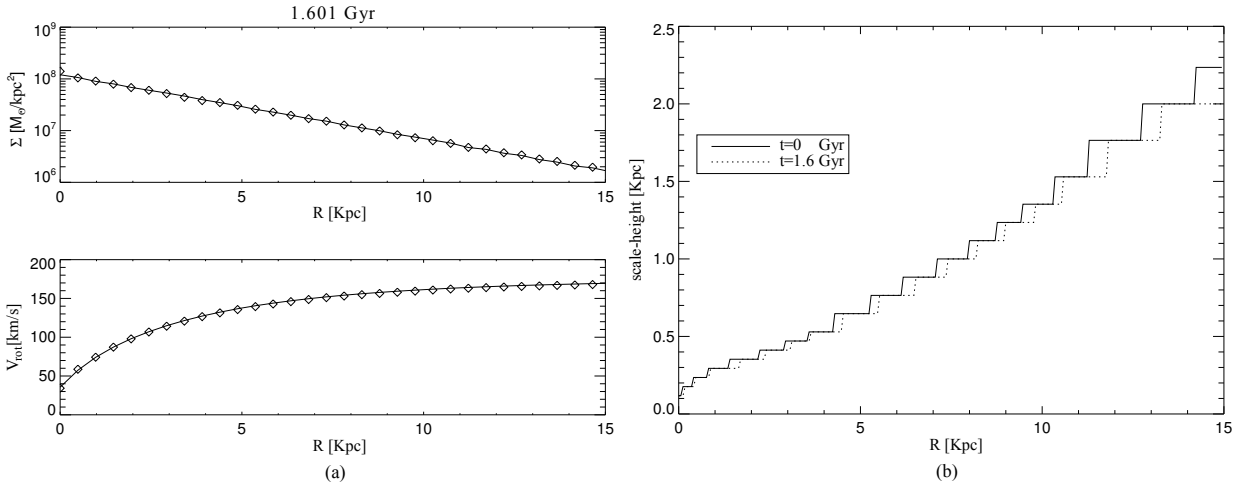

Figure 2.2: Model Gas0: The evolution of 1.6 Gyrs of a stable disk. (a) The evolution of the surface density (upper panel) and the rotation curve (lower panel) at $t = 0$ Gyr (solid) and $t = 1.6$ Gyr (diamond). Overall, the surface density and rotation curve are kept very well over 4 orbital periods. (b) The evolution of the scale-height at $t = 0$ Gyr (solid) and $t = 1.6$ Gyr (dotted). The small change in scale-height indicates that the required circular velocity is overestimated probably due to the approximation of Eq. (2.14) and Eq. (2.30). In all, the disk still stays well in the initial condition. The step-wise character of the scale-height reflects our discretization and the change of spatial resolution due to the AMR.

(2.29) overestimates the circular velocity needed to support the disk. The thickness of the disk reduces the potential in the midplane by a few percent (see Appendix A.2). Figure 2.3 shows the snapshots of the face-on surface density at $t = 0$ (Fig. 2.3a) and at $t = 1.6$ Gyr (Fig. 2.3b). No structure is developing during the course of the simulation.

To sum up, figures 2.1 to 2.3 indicate that without external perturbation the disk is quiet over secular time-scales. The shape of such a disk is naturally flaring, i.e., the scale-height increases with radius. The ideas described in Section 2.2 are able to treat the initial condition self-consistently. A well-balanced disk is especially useful to probe the onset of disk instability as described in the next Section.

2.4 Axisymmetric Instability

The question of disk stability has been investigated for more than four decades since the pioneering works by Toomre (1964) for collisionless stars and Goldreich & Lynden-Bell (1965) for gas sheets. Understanding the origin and evolution of disk structure is challenging. If the disk

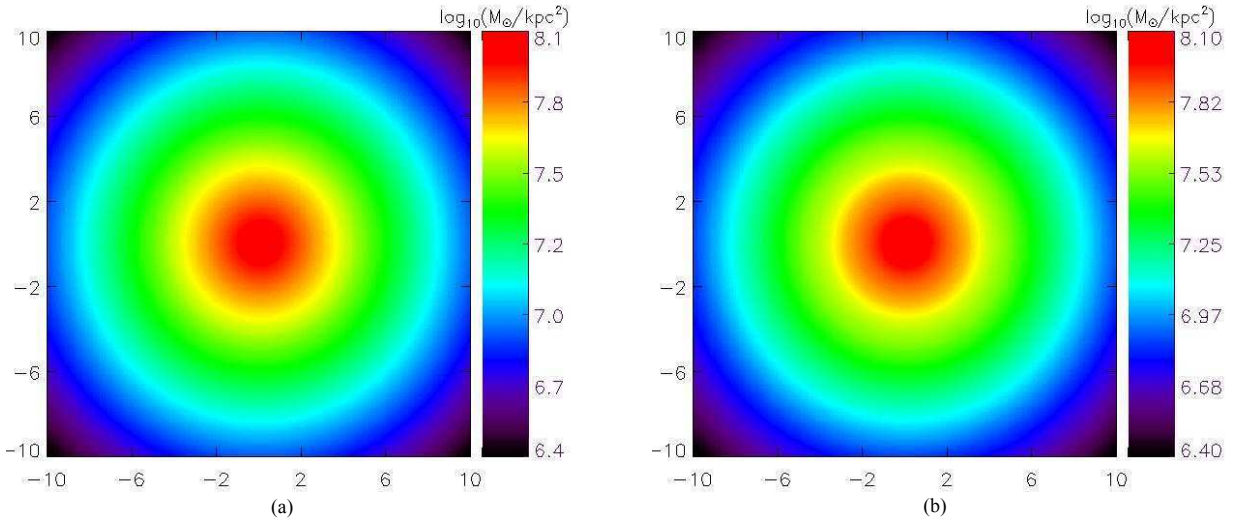

Figure 2.3: Model Gas0: The size of the images is 20 kpc × 20 kpc. The evolution of the surface density at (a) $t = 0$ Gyr and (b) at $t = 1.6$ Gyr. This figure shows that no structure is developing over secular time-scale.

is stable like our model Gas0, no structures can form. On the other hand, if the disk is highly unstable, the surface density will quickly fragment and develop a clumpy and chaotic-looking appearance. There will be no well-organized structures. The striking spiral appearance of many nearby disk galaxies indicates that those disks are marginally stable.

For an infinitesimally thin disk, the instability threshold is at $Q_{\rm th} = 1$ (Toomre 1964). The first theoretical work to include the finite thickness of a self-gravitating gas disk is that by Goldreich & Lynden-Bell (1965). Some authors have investigated the stability of finite thickness gas disks in numerical simulations (both in 2D and 3D) using local patches within a shearing box (Kim & Ostriker 2006, 2002b; Gammie 2001). This technique, in 2D, has also been used by Kim & Ostriker (2007) to investigate the interaction between the gas disk and a live stellar disk. Shetty & Ostriker (2006) used global 2D simulations in which they incorporated the effect of finite disk thickness by diluting the gravitational force. For 3D global disk calculations, see Li et al. (2005b,a, 2006), who investigate the relation between disk instability and star formation rate. These studies all agree that although the inclusion of the thickness does not have a qualitative impact on the disk instability, it does shift the threshold value of instability quantitatively. In addition, accounting for disk thickness may have a large impact on the evolution of a disk, such as the development of spurs or the wiggle instability (Kim et al. 2002; Kim & Ostriker 2006).

In this Section, armed with a well-balanced gas disk, we revisit the axisymmetric instability of disks in 3D global fashion. We first derive the reduction factor F which reflects the reduction of the gravity due to the finite thickness of the disk. Then the corresponding instability threshold

$Q_{\rm th}(R,T)$ derived from a semi-analytic calculation is compared with the numerical results. In the final sub-section, we also explore the impact of the presence of a static stellar potential on the axisymmetric instability.

2.4.1 The impact of thickness on disk stability

The Fourier component of the perturbed gravitational potential, Φ_k, of an infinitesimally thin disk is given by:

$$\Phi_k = -\frac{2\pi G\Sigma_k}{|k|}e^{ikx-k|z|}, \tag{2.32}$$

where k represents the wave number of the Fourier components and $x = R - R_0$ being the radial deviation for an axisymmetric perturbation. Supposing that a 3D disk is piled up by a stack of infinitesimally thin gas layers, we approximate the effect of the disk thickness by superimposing the contribution from every razor-thin layer:

$$\Phi_k(z) = -\frac{2\pi G\Sigma_k e^{ikx}}{|k|}\int_{-\infty}^{\infty} e^{-k|z-h|}\frac{\mathrm{sech}^2(h/h_z)}{2h_z}\mathrm{d}h, \tag{2.33}$$

with h_z being the scale-height of the disk. In Eq. (2.33), we model the vertical structure of the gas disk by a sech^2 function. This is valid especially for the inner part of disks where the vertical structure is mainly determined by the self-gravity of the gas. See also the Fig. A.1 in Appendix A.4. Equation (2.33) leads to the Fourier potential in the midplane:

$$\Phi_k(z=0) = -\frac{2\pi G\Sigma_k e^{ikx}}{|k|}F(k,h_z), \tag{2.34}$$

with $F(k,h_z)$ being the reduction factor described by (see Appendix A.3):

$$F(k,h_z) = 1 - \frac{1}{2}kh_z\left[H\left(\frac{kh_z}{4}\right) - H\left(\frac{kh_z}{4}-\frac{1}{2}\right)\right], \tag{2.35}$$

with H being the harmonic number defined by:

$$H(\alpha) = \int_0^1 \frac{1-y^\alpha}{1-y}\mathrm{d}y. \tag{2.36}$$

The Lin-Shu (1964) dispersion relation for the axisymmetric perturbation is then modified to:

$$\omega^2 = \kappa^2 - 2\pi G\Sigma_0|k|F(k,h_z) + c_{\rm s}^2k^2. \tag{2.37}$$

The dispersion relation states that on small scales ($k \to \infty$) the disk is stabilized by gas pressure, i.e., the term $c_{\rm s}^2k^2$. Large scales ($k \to 0$) are regulated by global shear, i.e., the κ^2 term. The instability however happens at intermediate wavelengths, much smaller than the disk size but

still larger than the thickness of the disk. In this region, neither global shear nor gas pressure can resist the gravitational collapse. The reduction factor, $0 < F \leq 1$, softens the effect of self-gravity and makes the disk more stable.

Given a certain radius R and temperature T, we obtain the threshold value $Q_{\rm th}(T, R)$ by probing the maximum value along the neutral curve defined by setting $\omega^2 = 0$ in Eq. (2.37) and calculating the epicyclic frequency, κ, from the rotation curve. Similar to the conventional Toomre criterion for the stability of an infinitesimally thin disk, $Q_{\rm th}$ is a threshold curve for thick disks. Above $Q_{\rm th}$ the disk is stable and otherwise unstable. Since the $Q_{\rm th}$ is a function of both temperature and radius, it is convenient to define the critical value $Q_{\rm crit}$, which is the value of $Q_{\rm th}$ for which $Q_{\rm th}(T, R)/Q(R) = 1$, and the corresponding critical temperature $T_{\rm crit}$.

The solid lines shown in Fig. 2.4 represent the threshold value $Q_{\rm th}$ as a function of radius. Each plot corresponds to a disk of different temperature. The dash-dotted lines are the actual Q values defined by Eq. (2.31) of the different models. From these figures, the most unstable radius is around $R = 2$ kpc. The corresponding surface densities after an evolution of 750 Myrs are shown in Fig. 2.5. The gas at the most unstable region has revolved for more than four orbital periods around the disk center.

These figures shows that the prediction of $Q_{\rm crit}$ and the numerical results match quite well. The Q value of Gas1 is well above the solid line and shows a featureless surface density. As shown in Gas2 and Gas3, with the decrease in temperature, the $Q_{\rm th}$ curves shift up and the disks' Q curves come down. As a consequence, the disk starts to develop multi-armed structure, which is very likely caused by swing amplification, as discussed in Section 2.5. And finally in Gas4, the curves Q and $Q_{\rm th}$ intersect. The disk fragments and starts to behave chaotically. A more detail calculation shows that the two curves just touch each other at a temperature $T_{\rm crit} = 8.5{\times}10^3$K with the maximum threshold $Q_{\rm crit} = 0.693$, which is close to $Q_{\rm crit} = 0.676$ of Goldreich & Lynden-Bell (1965) analysis but away from the numerical result, $Q_{\rm crit} = 0.647$, of Kim & Ostriker (2002b). However, the actual value of $Q_{\rm crit}$ is model dependent. Different models of the dark matter, the stellar disk and even the EoS will all affect the resulting value of $Q_{\rm crit}$.

2.4.2 The inclusion of stellar potentials

The inclusion of a static stellar disk alters two important factors which influence the stability of the disk. One is the rotation curve and the other is the thickness of the gas disk. By changing the rotation curve, the epicyclic frequency, κ, changes accordingly. Supposing a flat rotation curve described by $\Omega = V_0/R$, the epicyclic frequency κ then reads:

$$\kappa^2 = 2\Omega^2 = 2\frac{V_0^2}{R^2}, \tag{2.38}$$

with V_0 being the rotation velocity. The presence of a stellar disk tends to stabilize the gas disk via increasing V_0. However, by increasing the gravitational pull in the vertical direction, the gas disk becomes thinner and therefore more susceptible to gravitational collapse. In Section 2.4.1, we have already seen that the scale-height, which is governed by the temperature of the disk, is a very sensitive factor for the disk stability. GasStar1 to GasStar4 are designed to explore the competition between the two opponents.

From Fig. 2.6, we first notice that, compared to Fig. 2.4, the threshold value, $Q_{\rm crit}$, is boosted from 0.693 to 0.75 due to the decrease in scale-height. This makes the disk more prone to gravitational instability. On the other hand, the change of the rotation curve drastically shifts the dash-dotted curve upwards. Instability only sets in once the temperature of the gas disk drops below $T_{\rm crit} \sim 6000$ K. Overall, the presence of the static stellar disk tends to stabilize the disks.

Figure 2.7 shows the surface density after an evolution of 250 Myr. During this period, the gas in the most unstable region has finished 2.5 orbits. All the gas disks are developing multi-armed spiral structures within the region where the disk is the most vulnerable to instability according to Fig. 2.6. At this moment, the most unstable disk, GasStar4, is experiencing fragmentation. High density filaments are evident from the image. While GasStar2 is still in its early stage of instability, GasStar3 is just about to enter the fragmentation phase. GasStar1, on the other hand, does not fragments at all during the course of simulation.

The trend is clear. The cooler the disk, the faster it fragments. The spiral structure seen in these images are due to swing amplification (Toomre 1981; Goldreich & Lynden-Bell 1965), a mechanism that is capable of amplifying the perturbation by swinging the leading waves to trailing. Swing amplification is effective as the disk Q (dash-dotted line) is approaching the threshold $Q_{\rm th}$ (the solid line). The spirals are sheared, become tighter and tighter and enhanced. Once the density reaches the supercritical point, instability sets in.

2.5 Spontaneously Induced Spiral Structure

An interesting feature which is hard to ignore in Fig. 2.5 and Fig. 2.7 is that the marginally stable disks are spontaneously developing multi-arm spiral structures. We have already seen in Sections 2.3 and 2.4 that the effect of the disk thickness is to shift the range of the marginally stable region downwards and therefore to stabilize the disk. As we systematically lower the temperature to probe the onset of instability, runs with as well as without stellar potential are experiencing swing amplification.

Hohl (1971) found that disks which are marginally stable to axisymmetric perturbation are prone to develop a large-scale bar structure. This finding initiated both numerical (Zang & Hohl 1978;

Sellwood 1981, 1985; Fuchs & von Linden 1998; Sellwood & Moore 1999) and theoretical studies (Kalnajs 1978; Sawamura 1988; Vauterin & Dejonghe 1996; Pichon & Cannon 1997; Evans & Read 1998; Fuchs 2001) of marginally stable disks. Goldreich & Lynden-Bell (1965) and Toomre (1981) pointed out that self-gravitating, differentially rotating disks are able to amplify spiral waves by shearing a leading wave into a trailing one. Three key ingredients, self-gravity, shearing and epicyclic motions work harmonically to make the phenomenon now coined with the name 'swing amplification' happen.

Three necessary conditions need to be fulfilled in order to facilitate the swing amplification (Toomre 1981; Fuchs 2001; Fuchs & von Linden 1998; Binney & Tremaine 2008). First, the disk must be marginally stable, i.e., for an infinitesimally thin disk, $1 < Q < 2$, as defined by Eq. (2.31). Second, the parameter $X = k_{\rm crit}R/m = k_{\rm crit}/k_y$ (Toomre 1981; Binney & Tremaine 2008), with m being the number of arms and $k_{\rm crit} = \kappa^2/(2\pi G\Sigma_{\rm g})$ the critical wave number, has to be of order unity, i.e., somewhere between 1 and 3 (Goldreich & Lynden-Bell 1965; Julian & Toomre 1966; Toomre 1981). Third, there must be a mechanism that is able to induce leading arms in the system either explicitly by hand (Toomre 1981) or implicitly by random fluctuation induced by numerical noise (Toomre 1990; Sellwood & Carlberg 1984; Fuchs 2001). We notice that most of these works mentioned above are for live stellar disks not directly for the gas disk. But since the amplification principles are the same, the results are still applicable to pure gas disks.

As shown in Fig. 2.8a and 2.8b, GasStar1 gets more arms than Gas2 does. To be more quantitatively, Fig. 2.8c and 2.8d show the Fourier components as a function of radius. They are obtained by doing Fourier transform to $(\Sigma_{\rm g}(R,\phi) - \overline{\Sigma_{\rm g}}(R))/\overline{\Sigma_{\rm g}}(R)$, where $\overline{\Sigma_{\rm g}}(R)$ is the averaged surface density of a given radius. Note that the dominating modes tends to be multiples of $m = 4$. This is a consequence of using a Cartesian grid, for which $m = 4$ is the natural mode. However, the dominating mode is determined by physics. The dominating mode of Gas2 is $m = 8$ while in GasStar1 $m = 12$.

As is apparent from Eq. (2.38), including a stellar disk causes an increase in $k_{\rm crit}$. Consequently, a larger value of m is required in order to satisfy $1 < X < 3$. From the image shown in Fig. 2.8a and the relation, $k_{\rm crit} \propto \kappa^2$, to keep X a constant, the number of spiral arms in GasStar1 can be crudely estimated as $m \simeq 15$. More precisely, the number of spiral arms, m, is predicted by (Toomre 1981; Athanassoula et al. 1987; Fuchs 2001, 2008):

$$m = \frac{2\pi R}{\lambda_{\rm max}}, \tag{2.39}$$

with $\lambda_{\rm max}$ being defined by:

$$\lambda_{\rm max} = \frac{\lambda_{\rm crit}}{\chi(A/\Omega)}, \tag{2.40}$$

where $\lambda_{\rm crit} = 2\pi/k_{\rm crit}$. The coefficient χ is a function of rotation curve (Fuchs 2001), as measured by Oort's constant A.

We employ Eq. (2.39) to analytically estimate the number of arms and compare the predictions with the images shown in Fig. 2.8. For Gas2, spirals appear between 2 kpc and 5 kpc. Within this radial range, the most unstable wavelength ranges from 2.0 to 3.6 kpc. The corresponding prediction for m ranges from 6 to 9, while the simulation reveals a spiral pattern with 8-fold symmetry. For GasStar1, spirals are prominent between 3 and 4 kpc, while the corresponding most unstable wavelength ranges from 1.4 to 2.0 kpc. The twelve arms developing in GasStar1 should be compared to a predicted m ranging from 13 to 14. Hence, overall the trends in the simulations are in reasonable agreement with our predictions. Note that the spatial resolution in both simulations ranges from 60 pc to 120 pc, indicating that the most unstable wavelengths are well-resolved.

The observed small deviations can be explained as follows. First, the formulation used to predict the number of arms is precise only for stellar disks. However, Toomre (1981) has shown the strikingly similar behavior of gaseous disks (Goldreich & Lynden-Bell 1965) and stellar disks (Julian & Toomre 1966). Therefore, we have confidence that Eq. (2.39) is still applicable to gaseous disks. Second, the number of arms has to be an integer, a number of fraction given by Eq. (2.39) has no physical meaning. Third, the usage of a Cartesian grid introduces the multiples of the natural $m = 4$ mode, which manifests itself in the Fourier transform of the surface density. Fourth, swing amplification picks up the dominating mode. It takes some time to fully develop the dominating mode. All these factors combined determine the number of spiral seen in our simulations. It is important to realize that the most unstable radius according to the axisymmetric instability criterion might not be the most effective site for swing amplification, since the shear plays an important role in this process.

Without any external pumping source, spiral waves produced by swing amplification should be a transient phenomenon. Similar to material spirals, swing amplified spiral waves will experience azimuthal shearing which reduces their pitch angle until they become too tightly wound to be identified. As an example, in the Gas2 simulation, the spiral arm that appears around $R = 2$ kpc initially has a pitch angle of 90° and should be sheared to less than 1° within 2.2 Gyr. On the contrary, we find that the spontaneously induced spirals seen in Gas2 can last for more than 3 Gyr and still keep the pitch angle relatively open. This result suggests at least one mechanism keeps replenishing noise into the disk, leaving the physics to pick up the dominating mode and sustain the waves. This noise can be caused by numerics or preexisting waves.

2.6 Summary

In this Chapter we have developed a simple and effective method to compute the three-dimensional density and velocity structure of an isothermal gas disk in hydrodynamic equilibrium in the pres-

ence of an arbitrary external potential (i.e., dark matter halo and/or stellar disk). This is ideally suited to set-up the initial conditions of a three-dimensional gas disk in equilibrium in hydrodynamical simulations. We first notice that as long as the gas is barotropic or has constant temperature at $t = 0$, the circular velocity needed to support the self-consistent disk is independent of the height above or below the midplane. This feature greatly simplifies the process of specifying the initial velocity field. All we need to know is the rotation velocity in the midplane.

To specify the density distribution self-consistently, the hydrostatic equation coupled with the reduced Poisson equation is adopted to develop the vertical structure of the gas. Two sets of second-order non-linear differential equations are found. One is directly associated with the gas density called the density method, the other associated with the gas potential called the potential method. In a simulation involving a huge dynamic range (using AMR techniques), the potential method is shown to be numerically more stable. A simple local iteration can be performed to gain a better control on the shape and the mass of disks. These ideas are simple enough to be incorporated into any existing code, and most importantly they are very effective.

With gas disks that are in detailed balance, we are able to systematically investigate the axisymmetric stability of a fully three-dimensional disk for the first time. We probe the onset of instability both semi-analytically and numerically. Simulations without stellar disk show that the thickness of the gas disk, which is governed by the temperature of the disk, has a huge impact on the disk stability. The reduction of the gravity decreases the threshold value by around 30 percent in our models. As we gradually lower the gas temperature, the threshold $Q_{\rm th}$ shifts up, the disk Q shifts down, and the system starts to develop multi-arm structure via swing amplification. The onset of the instability in simulations matches the theoretical prediction very well as shown in Fig. 2.4 and Fig. 2.5. The disk fragments as the two curves, Q and $Q_{\rm th}$, come very close to each other.

The influence of the stellar disk is less obvious. Its presence has a stabilizing effect on the gas disk through changing the rotation curve and a destabilizing one through the increase of the local gravitational force. The simulation results show that overall the presence of the stellar disk tends to stabilize the gas disk. But this conclusion comes with a caveat. The interaction between live stars and gas might be important. A live stellar disk itself can be unstable or marginally stable. Perturbations from the interstellar medium can trigger instabilities in the stellar disk. Since stars dominate the mass budget in Milky-Way type galaxies (more than 90 percent), and because gas is highly responsive and dissipative, the interplay between both components is one of the most interesting subjects in galactic dynamics. Tackling this problem needs elaborate initial conditions for the live stellar disk or the combined disk. We stress that the potential method developed in this Chapter is compatible with the formulation in KD95. This makes the self-consistent combined disk a natural direction for future work.

Marginally stable disks are susceptible to the process of swing amplification, a prevalent mechanism that triggers self-induced spirals. Simulations Gas2 and GasStar1 show the spirals are prominent in the regions in which the gas can respond to swing amplification. Semi-analytic result relates the most vulnerable wavelength in azimuthal direction, $\lambda_{\max}$, to the number of arms. Numerically, The natural mode of a Cartesian grid together with the swing amplification determine the dominating mode of the spiral structure. Our numerical results with or without stellar disk shows the correct characteristics of the swing amplification. It happens in marginally stable disks and the number of arm fits reasonably well to the analytic prediction. In the run of GasStar2, swing amplification eventually leads to disk fragmentation once the density becomes supercritical to the gravitational instability. However, in a sub-critical case like Gas2, the spiral structure can survive more than 3 Gyrs without fragmenting the disk, suggesting at least one mechansim is sustaining the waves. The number of arms suggests a characteristic wavelength relating to the upper limit of the mass of giant molecular clouds (Escala & Larson 2008).

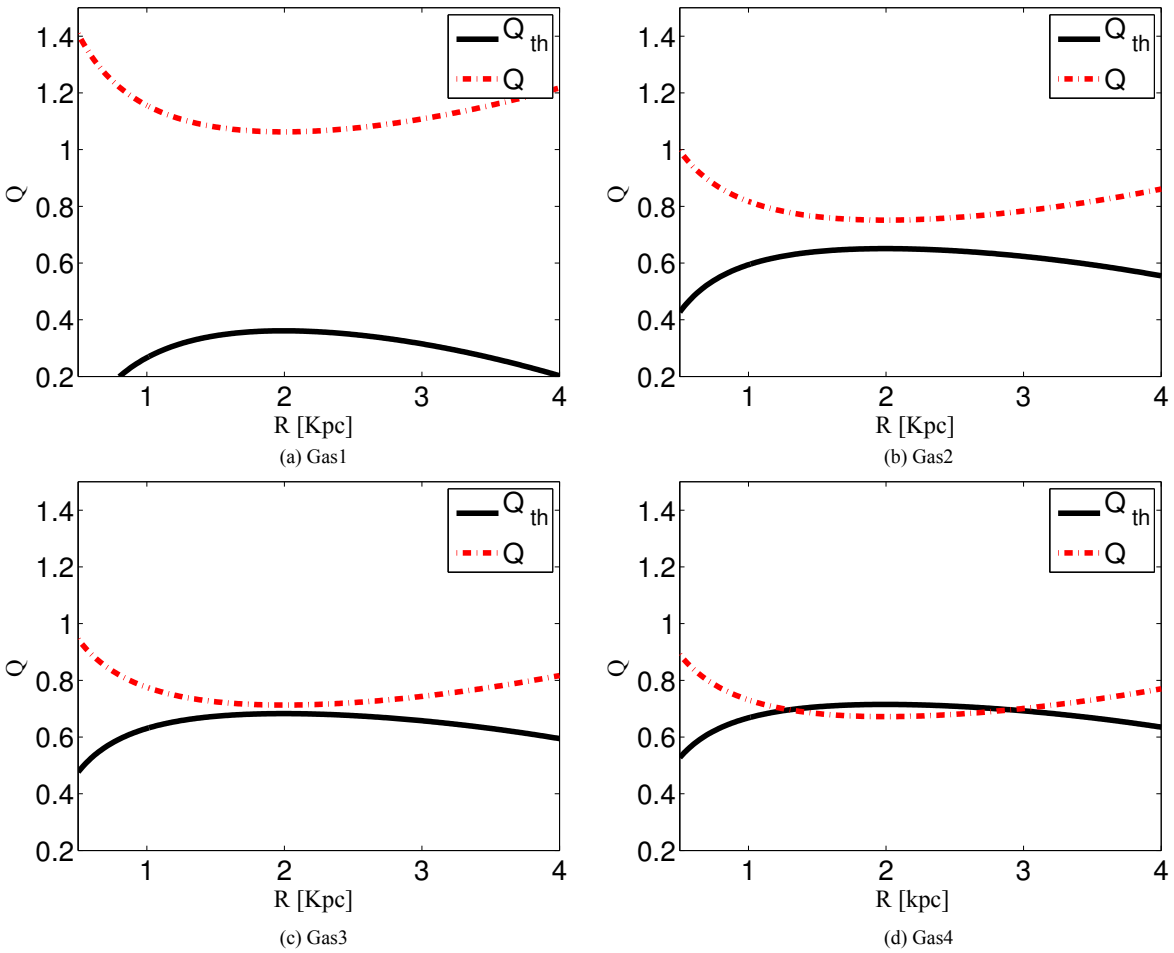

Figure 2.4: Plots (a) to (d) correspond to models from Gas1 to Gas4, respectively. In each plot, curves of the disk Q (dash-dotted) and the threshold value $Q_{\rm th}$ (solid) are put together to probe the onset of axisymmetric instability. $Q_{\rm th}(R)$ is a obtained by probing the maximum value along the neutral curve for a given radius. Information of the disk thickness has been encapsulated in the reduction factor defined by Eq. (2.36). When the two curves meet, we expect the disk fragments very fast. This figure shows that the most unstable region is about the radius $R = 2$ kpc. The fact that the $Q_{\rm th}$ curves are well below unity shows the impact of the disk thickness on the disk stability.

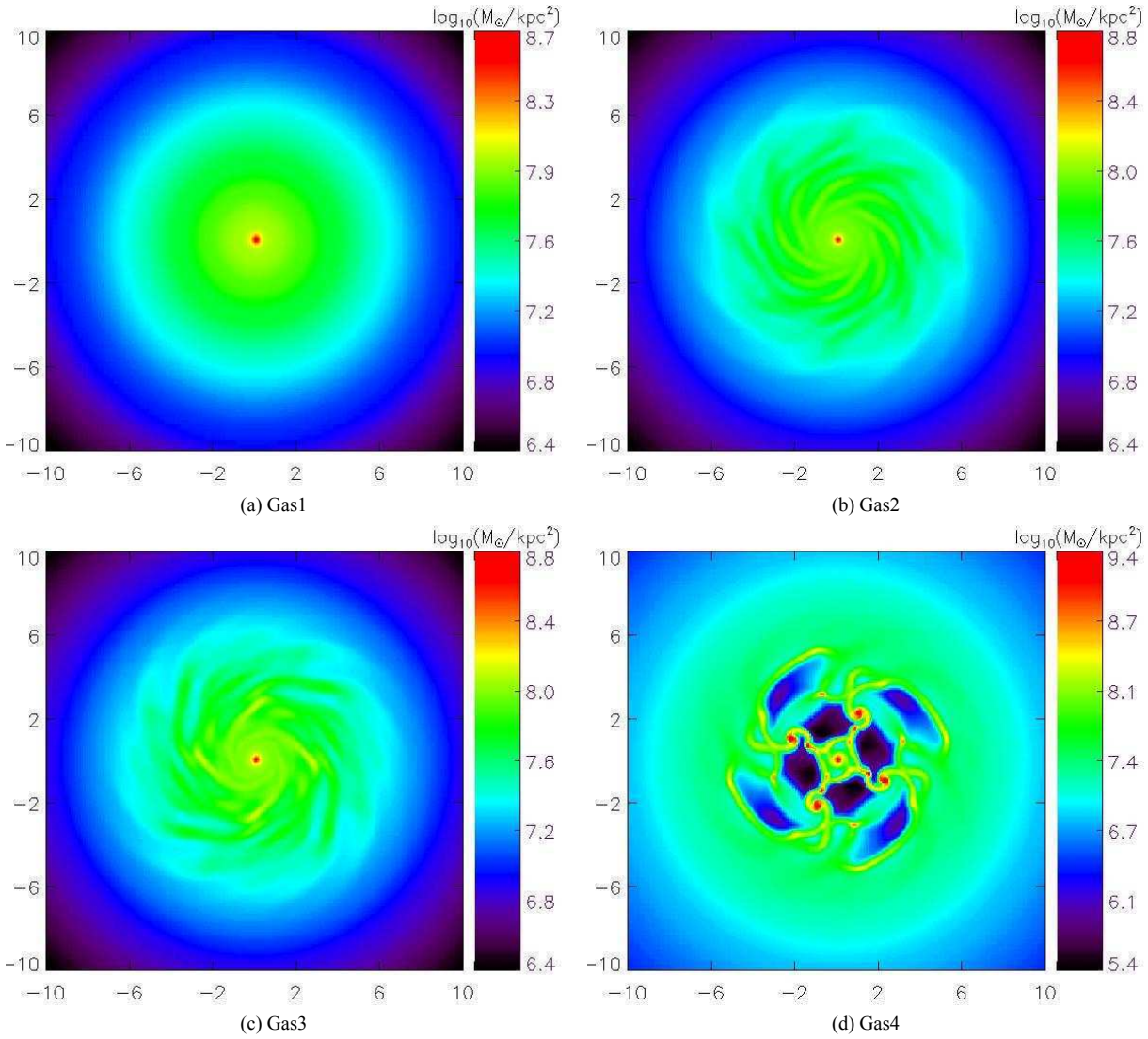

Figure 2.5: Images (a) to (d) correspond to models Gas1 to Gas4, respectively. They show the face-on surface density at $t = 750$ Myr. The size of the images are 20 kpc $\times$ 20 kpc. The gas at the most unstable radius has orbited around the center for more than four times. (a) Since the disk Q is well above the threshold value $Q_{\rm th}$, the disk is featureless. In models Gas2(b) and Gas3(c) the disk Q is approaching $Q_{\rm th}$ around $R = 2$ kpc, both disks are developing self-induced spirals due to swing amplification. (d) The disk fragments very fast once Q and $Q_{\rm th}$ intersect.

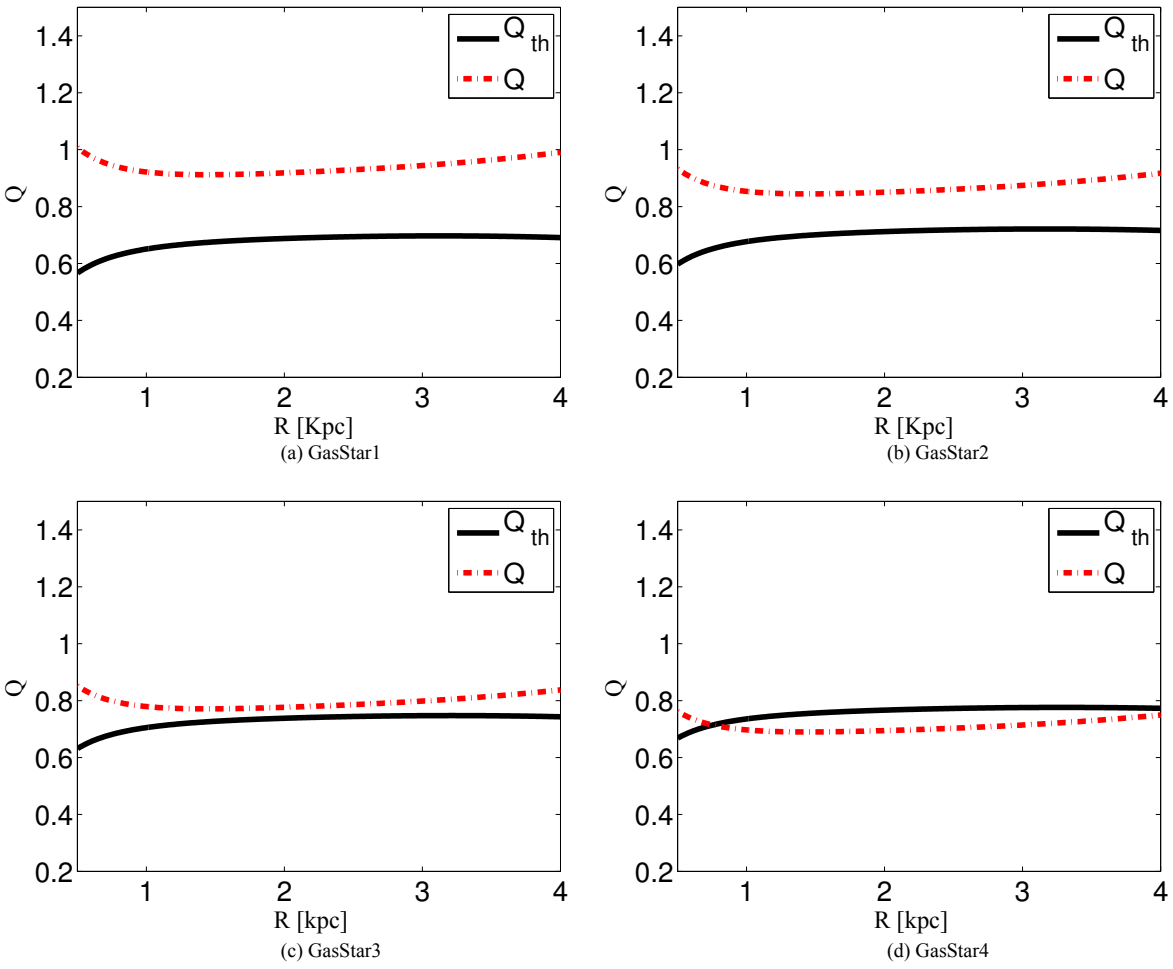

Figure 2.6: Plots (a) to (d) correspond to models GasStar1 to GasStar4, respectively.: The Q (dash-dotted) and $Q_{\rm th}$ (solid) curves of the gas disks of different temperatures. The presence the stellar potential stabilizes the disks through changing the rotation curve and destabilizing the disk by increasing local gravitational force. The effect of disk thickness is included via the reduction factor Eq. (2.35). We need to lower the temperature down to T= 7×10^3 K in order to probe the onset of axisymmetric instability. Overall, the presence of the stellar potential stabilizes the disk.

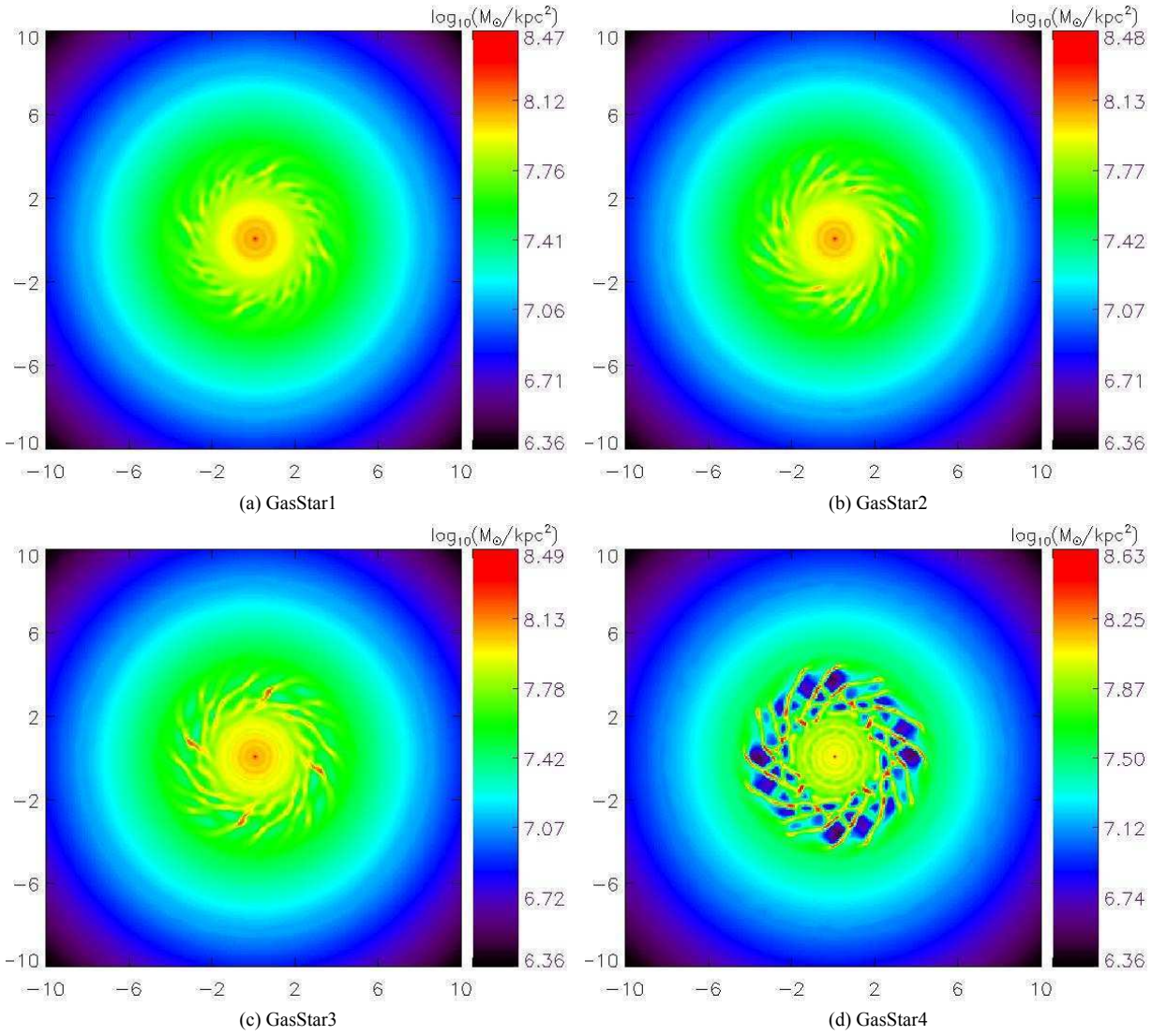

Figure 2.7: Images (a) to (d) correspond to models GasStar1 to GasStar4. They show the face-on surface density at $t = 250$ Myr. The size of the images are 20 kpc $\times$ 20 kpc. The gas at the most unstable radius has orbited around the center about two and half times. Spirals seen in model GasStar2(b) and GasStar3(c) are due to swing amplification. In (d) the disk fragments very fast mainly due to both the axisymmetric instability and swing amplification.

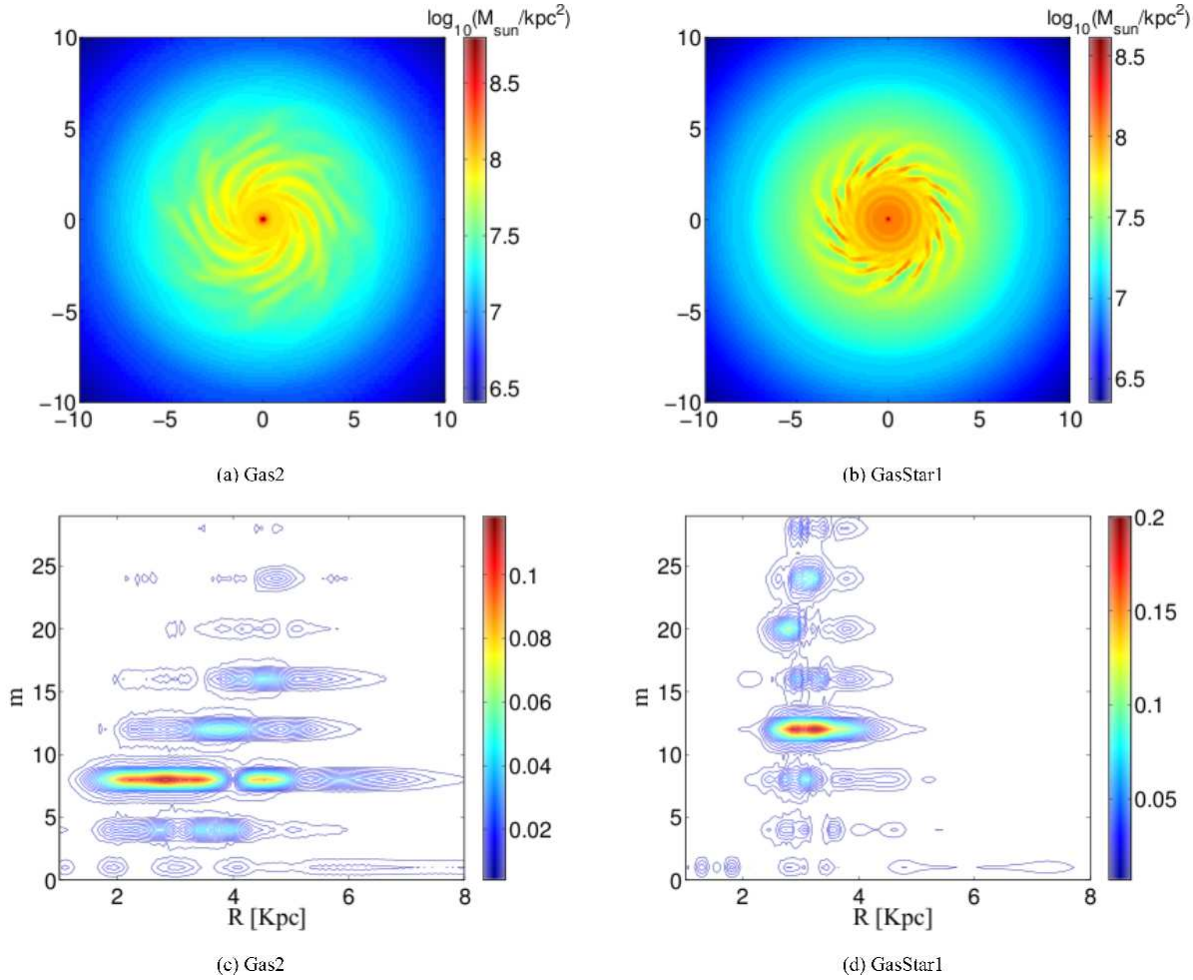

Figure 2.8: The image size in (a) and (b) is 20 kpc × 20 kpc. (a) The surface density of Gas2 at $t = 750$ Myr. (b) The surface density of GasStar1 at $t = 500$ Myr. In both cases, the inner parts of the gas disks, which have been evolved for about four orbital times, developing spiral structure. Contour plots (c) and (d) are the Fourier maps of (a) and (d), respectively. In (c) and (d), the horizontal axis represents radius, the vertical axis is the number of arms, m, obtained by Fourier analysis. The color represents the intensity of each Fourier mode, the redder the stronger.

Chapter 3

Evidence for Radial Inflow In The Extended HI Disk of M83 (NGC5236)

3.1 Introduction

A longstanding missing link associated with the evolution of disk galaxies is the replenishment of gas in order to sustain star formation over cosmological times. Molecular gas depletion times in nearby galaxies are typically 2 Gyr (Bigiel et al. 2008; Leroy et al. 2008), a number that may also be expected on theoretical grounds. Pflamm-Altenburg & Kroupa (2009) show that the gas depletion time for dwarf irregular and large disk galaxies, including the Milky Way, is estimated to be about 3 Gyr. At higher redshift, similar depletion times of $0.6-1.5$ Gyr have been measured out to $z \approx 2$ (Genzel et al. 2010). Recent work of Daddi et al. (2010a) suggests a depletion time of 0.5 Gyr for the molecular gas of near-infrared-selected (BzK) galaxies, scaled-up analogues of local spiral galaxies. For vigorously star forming merging systems, however, star formation seems to deplete the molecular gas on even shorter time scales ($\sim$ 100 Myr, Daddi et al. 2010a).

In many galaxies neutral hydrogen (HI) is found out to radii much larger than the optical extent, it therefore provides valuable information about the signature of possible gas infall. The lopsidedness and asymmetry commonly seen in the outer disks of galaxies are usually considered a result of gas accretion (Bournaud et al. 2005; Jiang & Binney 1999; Ostriker & Binney 1989; Fraternali & Binney 2008), of recent minor mergers (Zaritsky & Rix 1997) or of tidal interactions (Kornreich et al. 2002). Detection of high velocity clouds (HVCs, Miller et al. 2009), extra-planar HI clouds with low metallicities (van Woerden & Wakker 2004), anomalous kinematics (Fraternali et al. 2002) and the velocity gradient perpendicular to the galactic plane (Fraternali et al. 2005) point to a number of different mechanisms of how gas could be redistributed within galaxy disks. Although a number of different ways for fueling star formation has been proposed, the amount of infalling gas currently observed not associated with the gas disks of galaxies is still about one order-of-magnitude lower than what is needed to compensate gas consumption from presently

observed star formation. See Sancisi et al. (2008) and Fraternali (2010) for a review of this topic. Recently, Klessen & Hennebelle (2010) point out that gas accretion can be an important means of driving and sustaining turbulence in the outer disk where star-forming activity ceases.

Wong et al. (2004) examine seven nearby spirals, searching for kinematic evidences of gas infall. They place equivocal radial inflows of $\sim 5-10$ km s^{-1} in the inner regions. Based on a tilted-ring analysis, Trachternach et al. (2008) quantify the strength of non-circular motions for 19 THINGS (The HI Nearby Galaxy Survey, Walter et al. 2008) disk and dwarf galaxies. The strength is defined as the quadratically-added amplitude of all non-circular Fourier coefficients. They find that the strength of non-circular motions is generally less than 9 km s^{-1}. The apparently small values of the radial motions will be discussed in Section 3.3.1.

Recently, ultraviolet imaging with the *Galaxy Evolution Explorer* (*GALEX*) reveals massive star formation in the extreme outskirts of M83 (Thilker 2005; Bigiel et al. 2010a). Bigiel et al. (2010b) demonstrates a tight spatial correlation between the HI maps from THINGS and the far ultraviolet (FUV) maps of *GALEX* out to about 4 optical radii. A possible scenario to explain these observations is that tidal interactions compress the gas which subsequently tiggers star formation in the outer region of M83. The high resolution interferometric HI observations combined with the fact that a huge gas reservoir up to 80% of the total HI sits outside the Holmberg radius (7.3′, Huchtmeier & Bohnenstengel 1981, hereafter HB81), where HI is likely the dominant constituent of interstellar medium (ISM), makes M83 a perfect object for investigating the ongoing process of gas infall.

The outer disk of M83 is highly lopsided and asymmetric (HB81, Rogstad et al. 1974), both in the kinematics and the mass distribution. Because interferometers by design do not pick up emission on large spatial scales, we combine the THINGS VLA map with single dish data from the 100-m radio telescope of the Max-Planck-Institut für Radioastronomie at Effelseberg (HB81) in order to obtain a complete census of the atomic hydrogen across M83. This is a particular concern given the large fraction of (presumably mostly diffuse) HI in the outer parts of M83.

Fourier analysis of the line-of-sight velocity, $V_{\rm los}$, has been used to investigate the elongation of the potential (Gentile et al. 2005; Schoenmakers et al. 1997), streaming motion along bars or spirals (Wong et al. 2004; Trachternach et al. 2008) and kinematic lopsidedness (Schoenmakers & Swaters 1999). In this Chapter, we perform a detailed Fourier analysis of the line-of-sight velocity to detect possible contributions of radial gas flow to the projected velocity. This excercise will then provide us with valuable information about the kinematic structures and a straightforward way to evaluate the possible presence and strength of any radial flow for M83.

This Chapter is structured as follows. We describe the properties of the interferometric data and the single-dish data in Section 3.2. The way we do the Fourier decomposition, the entanglement of these Fourier coefficients and their contribution to the observable $V_{\rm los}$ are discussed in Section

3.3. We apply this method to search for a radial inflow in the outer disk of M83. The process of parameter survey and the results are shown in Section 3.4. We discuss the implications of the results in Section 3.5. A brief summary is given in Section 3.6.

3.2 HI maps of M83

We combine the THINGS VLA HI map from Bigiel et al. (2010a) and the single dish data described in HB81 to search for the signs of radial inflow in the HI disk of M83. In the following, we refer to the maps from the THINGS survey as 'THINGS' maps and to the maps reconstructed from the 100-m single dish radio telescope at Effelsberg as 'Effelsberg' maps.

The THINGS map covers a field-of-view $\sim 50'$ and has been corrected for primary beam attenuation (the VLA primary beam FWHM is $\sim 30'$). The 'natural' weighting scheme is applied to yield a sensitivity (1σ RMS) of 0.8 mJy/beam and a resolution of $\sim 13''$. For details of data processing, units conversion, assessment of uncertainties, etc., of the THINGS map, we refer the reader to Bigiel et al. (2010b).

Figure 3.1a shows the THINGS intensity map of M83 in units of $M_\odot$ pc^{-2} and Fig. 3.1b the map of line-of-sight velocity, $V_{\rm los}$. Before preceeding with the analysis, we note that M83 can be roughly divided into three parts by eye, an inner face-on disk ($< 5'$), a bright HI ring with a relatively large inclination ($6' < R < 12.75'$ as indicated by the two white ellipses) and a filamentary outer part ($> 12.75'$). The distinct inclinations of the inner disk and the extended disk outside the Holmberg radius (7.3′, HB81), which is shown as the white ellipse in Fig. 3.2, is intriguing. The nonparallel axis of rotation suggests that the disks may be of different origins and the presence of the filaments seen in the outer disk might be a signature of onging gas accretion. We leave the detailed discussion to Section 3.5.

Although a good correlation exists between the synthesis HI observations and the far ultraviolet (FUV) emission, which traces star formation activity, in the far outer disk of M83 (Bigiel et al. 2010a; Miller et al. 2009), interferometers by design are not able to pick up diffuse, low column density HI on very large scales. To overcome this, we incorporate the information of the single dish Effelsberg map into our analyses.

The Effelsberg map is a hybrid map combining aperture-synthesis observations (Rogstad et al. 1974, RLW hereafter) for the inner disk ($R < 15'$) and single dish Effelsberg observations for the outer disk ($R > 15'$). RLW's observation uses Owens Valley Radio Observatory with resolution $2'$ and 10.5 km s^{-1}. The Effelsberg observations have a limiting sensitivity of 6×10^{18} atoms cm^{-2}, beam size 9 arc min and a linear extent ≥ 125 kpc in diameter. In this Chapter, we adopt a distance of 4.5 Mpc for M83 (Karachentsev et al. 2004). Unfortunately, given the age of the

Effelsberg observations (done in the late 70s), the original data are not available in electronic form. We therefore rebuild the HI density map from the contour maps in HB81 (their Figs. 2 and 3). The contours are interpolated using a bilinear algorithm. The reconstructed HI column density and $V_{\rm los}$ maps are shown in Figs. 3.1c and 3.1d, respectively. We convert brightness temperatures into column densities via the following relation:

$$\Sigma_{\rm HI} = 1.460 \times 10^{-2} \int T_{\rm B} {\rm d}v, \tag{3.1}$$

with $T_{\rm B}$ [K km s^{-1}] being the brightness temperature and $\Sigma_{\rm HI}$ the column density in units M$_\odot$ pc^{-2}.

Our ability to reconstruct the Effelsberg map in the center is limited due to a lack of contours in the HB81 plots. This leads to an artificial plateau in the very center (Figs.3.1c and 3.3b). The crowded contours seen in the very center of Fig. 3.1d are separated manually. This might have an impact on the tilted-ring analysis which we will address in the respective sections. The sparse contours, especially in the southern part of the velocity map, will also contribute to the uncertainties. Nevertheless, the superposition of Fig. 3.1a and Fig. 3.1d as shown in Fig. 3.2 illustrates the power of combining single dish and interferometric data, allowing to probe the HI distribution at high resolution while recovering all of the diffuse emission. The parts where both maps overlap are the focus of this Chapter.

3.3 Fourier Decomposition

3.3.1 Axi-symmetric flow

The fact that HI can be detected in the outskirts of galaxies and that it is the dominant mass component of the interstellar medium at large radii makes it an ideal tracer for the kinematics of the outer disk. The observable, $V_{\rm los}$, is a combination of the systemic velocity, $V_{\rm sys}$, the rotation velocity, $V_{\rm rot}$, and the radial velocity, $V_{\rm rad}$:

$$V_{\rm los} = V_{\rm sys} + V_{0,\rm rot} \cos(\theta) \sin(i) + V_{0,\rm rad} \sin(\theta) \sin(i), \tag{3.2}$$

with i being the inclination angle. The subscript, 0, represents the axi-symmetric component of the velocity. The relation between the sky-coordinates, (x, y), and the polar coordinates, (R, θ), defined in the galactic plane is:

$$\cos(\theta) = \frac{-(x - x_{\rm c}) \sin({\rm PA}) + (y - y_{\rm c}) \cos({\rm PA})}{R}, \tag{3.3}$$

$$\sin(\theta) = \frac{-(x - x_{\rm c}) \cos({\rm PA}) - (y - y_{\rm c}) \sin({\rm PA})}{R \cos(i)}, \tag{3.4}$$

with (x_c, y_c) being the center of the galaxy and PA the position angle measured in the sky plane, from north to east, with respect to the receding side of the line-of-nodes.

In a tilted-ring analysis (Begeman 1989) the disk is decomposed into a series of radial annulli with a certain width. For each ring, a set of parameters, (x_c, y_c), PA, i, V_{sys}, $V_{0,rot}$, $V_{0,rad}$, are determined independently to describe the position of the ring and the kinematics of the gas. It is not possible to determine all the unknowns at once, because typically the degeneracy among these parameters is quite large. Deriving a set of values typically requires further assumptions in order to converge to a physically plausible solution. In this Chapter, the fitting is done with the nonlinear least-squares fitting function LSQNONLIN in MATLAB.

Usually, several iterations are needed to fix each one of the parameters. V_{sys} and (x_c, y_c) are usually quite stable and therefore determined first. These parameters are then fixed for the next round of fitting. The assumption behind this step is that the systemic velocity and the center of the galaxy are global parameters and thus do not vary ring by ring. With the systemic velocity and the center fixed, PA and i are determined next. Although they are relatively stable parameters, they change quite notably in the extended disks where lopsidedness, asymmetry and disk warps are often an issue. Nevertheless, they are usually fairly constant parameters inside the Holmberg radius. Finally, the rotation curve $V_{0,rot}$ is derived with all other parameters fixed. Thus this is the last step of this iterative process.

An assumption behind the whole fitting procedure is that the gas is moving on well-defined circular orbits. The local radial velocity is assumed to be a small perturbation superimposed on the rotation velocity; a result of epicyclic motions. The presence of an axi-symmetric $V_{0,rad}$ introduces a phase shift and a change in the amplitude in the following way:

$$\begin{aligned} V_{los} &= V_{sys} + \sqrt{V_{0,rot}^2 + V_{0,rad}^2}\cos(\theta - \psi)\sin(i) \\ &= V_{sys} + V'_{0,rot}\cos(\theta(\mathrm{PA}'))\sin(i), \end{aligned} \tag{3.5}$$

where $\tan(\psi) = V_{0,rad}/V_{0,rot}$ and $V'_{0,rot} \equiv \sqrt{V_{0,rot}^2 + V_{0,rad}^2}$ is the apparent rotation velocity and PA′ the apparent position angle if the fitting procedure is carried out without involving $V_{0,rad}$. Equation (3.5) shows one of the degeneracies that exist among the fitted parameters. There is no straightforward way to break this degeneracy. It also reveals that the fitting procedure described in Wong et al. (2004) tends to minimize the contribution from $V_{0,rad}$. Because $V_{0,rad}$ is not involved in their fitting procedure, most of the contribution is attributed to the rotation velocity in the first place. This might be a cause for their attempt of searching for radial inflow being inconclusive.

3.3.2 Inclusion of Harmonics

In Section 3.3.1, we have shown that the focus of classical tilted-ring analysis is on extracting the axi-symmetric azimuthal flow and the basic parameters such as PA and *i*, which are used to deproject the galaxy from the plane of the sky. However, the gas motion is complicated and is subject to the presence of bars, spirals, tidal interaction with nearby companions, non-spherical potentials, etc. Furthermore, extended disks are usually asymmetric and lopsided in both mass and kinematics. This could be a result of uneven gas accretion. To incorporate these features into the tilted-ring model, one needs to include higher harmonics.

Schoenmakers et al. (1997) apply the Fourier decomposition to the line-of-sight velocity, $V_{\rm los}$. Based on the epicyclic approximation, they link the Fourier coefficients to the non-axisymmetry of the potential of a filled gas disk and conclude a nearly symmetric potential for NGC 2403 and NGC 3198. Along the same line, Trachternach et al. (2008) examine the non-circular motion for a larger sample, 19 galaxies from THINGS, attempting to quantify the triaxial dark matter potential. Their results are consistent with a round potential, showing ~90% of galaxies having median non-circular motions of less than ~9 km s^{-1}. Wong et al. (2004) apply the same method to looking for radial gas flow for seven nearby spiral galaxies and place an ambiguous upper limit of $\sim 5-10$ km s^{-1} for the inner region of galaxies.

In this Chapter, the Fourier decomposition is made by first fitting a tilted ring model as described in the previous section and subsequently, as one step further, we decompose the Fourier coefficients that are extracted from the observable $V_{\rm los}$ into rotational and radial components. We define the following quantities:

$$V_{\rm los}(R,\theta) = c_0 + \sum_k [c_k \cos(k\theta) + s_k \sin(k\theta)], \tag{3.6}$$

$$V_{\rm rad}(R,\theta) = B_0 + \sum_k [A_k \sin(k\theta) + B_k \cos(k\theta)], \tag{3.7}$$

$$V_{\rm rot}(R,\theta) = D_0 + \sum_k [C_k \sin(k\theta) + D_k \cos(k\theta)]. \tag{3.8}$$

Equations (3.6), (3.7) and (3.8) are the Fourier decomposition of $V_{\rm los}$, $V_{\rm rad}$ and $V_{\rm rot}$, respectively.

Substituting them into Eq. (3.2) yields:

$$V_{\rm los} = c_0 + \sum_k [c_k \cos(k\theta) + s_k \sin(k\theta)] \tag{3.9}$$

$$\begin{aligned} &= V_{\rm sys} + \frac{1}{2}\Big\{ (A_1 + D_1) \\ &+(2B_0 + C_2 - B_2)\sin(\theta) + (2D_0 + A_2 + D_2)\cos(\theta) \\ &+(B_1 + C_1 + C_3 - B_3)\sin(2\theta) + (D_1 - A_1 + D_3 + A_3)\cos(2\theta) \\ &+(B_2 + C_2 + C_4 - B_4)\sin(3\theta) + (D_2 - A_2 + D_4 + A_4)\cos(3\theta) \\ &+(B_3 + C_3 + C_5 - B_5)\sin(3\theta) + (D_3 - A_3 + D_5 + A_5)\cos(4\theta) \\ &+ \cdots \Big\} \sin(i). \end{aligned} \tag{3.10}$$

There is considerable degeneracy between the observables, (c_k, s_k), and the unknown Fourier coefficients, (A_k, B_k, C_k, D_k). Without further assumptions, it is impossible to solve for the unknowns simultaneously. Due to the disk inclination, the in-plane radial and rotational motions of harmonic numbers $k-1$ and $k+1$ contribute to the observables s_k and c_k seen on the sky.

In order to apply this method, we restrict the discussion to the second harmonics, i.e., we set $(A_k, B_k, C_k, D_k) = (0, 0, 0, 0)$ for $k > 2$. Several reasons prevent us from going for higher harmonics. First, involving the next harmonics will introduce a larger degeneracy that will lead to unstable and poorly constrained results. Different initial guesses for the fitting lead to different results that render this approach inconclusive. Second, it is difficult to derive higher harmonics for the incomplete (due to limited sensitivity) high resolution THINGS data in the outskirts of M83. Third, whereas the reconstructed single dish Effelsberg map does provide a complete census of the HI distribution at large radii, the resolution is too low to meet the requirements for a decomposition into higher harmonics. With these restrictions, the relation between Eqs. (3.9) and (3.10) can be simplified in the following way:

$$\begin{aligned} V_{\rm los} &= c_0 + c_1\cos(\theta) + s_1\sin(\theta) + c_2\cos(2\theta) \\ &\quad + s_2\sin(2\theta) + c_3\cos(3\theta) + s_3\sin(3\theta) \end{aligned} \tag{3.11}$$

$$\begin{aligned} &= V_{\rm sys} + \frac{1}{2}\Big\{ (A_1 + D_1) \\ &+(2B_0 + C_2 - B_2)\sin(\theta) + (2D_0 + A_2 + D_2)\cos(\theta) \\ &+(B_1 + C_1)\sin(2\theta) + (D_1 - A_1)\cos(2\theta) \\ &+ (B_2 + C_2)\sin(3\theta) + (D_2 - A_2)\cos(3\theta) \Big\} \sin(i) \end{aligned} \tag{3.12}$$

By comparing Eqs. (3.7) and (3.8) with Eq. (3.2), one can immediately identify B_0 and D_0 with $V_{0,\rm rad}$ and $V_{0,\rm rot}$, i.e., the axi-symmetric components of the flow. However, Eq. (3.12) states that the apparent axi-symmetric components, s_1 and c_1, are entangled with the second harmonics. It

also reveals that the systemic velocity can be contaminated by the presence of lopsidedness, i.e., an $m = 1$ component. Nevertheless, if one assumes a model for the systemic velocity, $V_{\rm sys}$, then the coefficients (A_1, D_1) can be solved for by comparing c_0 to c_2. Similarly, (B_2, C_2) and (A_2, D_2) can be found using the observables (s_1, s_3) and (c_1, c_3), respectively. The only degeneracy in this case is in the term (B_1, C_1), which corresponds to s_2. One further assumption or a model for the potential is required to disentangle them, such as the epicyclic approximation. In this Chapter, we attribute s_2 equally to B_1 and C_1, i.e., we assume that the rotational and the radial motions will have similar values for this component.

Despite this degeneracy, this new method has several advantages over previous approaches: first, instead of attributing s_1 completely to the radial velocity, as is done by Wong et al. (2004), we distribute it to both, rotational and radial velocities. After all, as gas gets disturbed it can move in both directions. Second, this procedure allows us to construct residual $V_{\rm rad}$ and residual $V_{\rm rot}$ maps simultaneously. The kinematics of gas can be rather complicated: e.g., the radial velocity might be part of epicyclic motions, which will not contribute to potential net radial inflow, or the gas may exchange angular momentum. As a result, gas gaining angular momentum will be moving outward, while gas losing angular momentum will be moving inward. The residual maps provide crucial information about the gas movement in different directions. Third, including harmonics up to second order already allows us to study the basic flow patterns caused by tidal interactions ($m = 1$), uneven gas accretion ($m = 1$), and two-fold structures such as bars or two-arm spirals ($m = 2$).

3.4 Application to M83

3.4.1 The Method

The fact that M83 is a low-inclination galaxy means that its rotation curve and associated parameters are difficult to derive, i.e., the low inclination introduces large uncertainties in the rotational velocity. Thus, the rotation curve of M83 is poorly constrained in the literature. To get around this problem, instead of extracting a set of fit parameters with large uncertainties, our approach is to examine a range of model rotation curves ($V_{0,\rm rot}$) and the corresponding fit parameters (PA, i, $V_{\rm sys}$, $V_{0,\rm rad}$) to derive the best possible estimate of the real rotation curve. Following the work of HB81, we adopt a Brandt-type flat rotation curve:

$$V_{0,\rm rot}(R) = \begin{cases} V_{\rm max}\dfrac{r}{(1/3 + (2/3)r^n)^{3/(2n)}} & R < R_{\rm max} \\ V_{\rm max} & R \geq R_{\rm max} \end{cases}, \tag{3.13}$$

with $R_{\rm max} = 4.5'$ being the radius where the rotation curve reaches the peak rotation velocity, $V_{\rm max} = 160, 180, 200$ km s^{-1}, $r \equiv R/R_{\rm max}$ and $n = 0.8$ a shape parameter controlling the rising part of the rotation curve. The rotation curve for the three models is shown in Fig. 3.3a. Among them, the model with $V_{\rm max} = 180$ km s^{-1} suggested in HB81 is adopted as our fiducial case. This choice will then be justified in Section 3.5. Note that unlike HB81, we keep the rotation curve flat in the outer disk based on the fact that de Blok et al. (2008) find no unambiguous evidence for declining rotation curves in any of the 19 THINGS galaxies in their sample. Similar to Schoenmakers et al. (1997), our fitting procedure starts with the conventional tilted-ring model followed by the Fourier decompostion along each ring. Using a range of prescribed rotation curves not only helps us to stabilize the fitting procedure (the degeneracy is reduced), it also brackets the potential uncertanties in the rotation curve. We look for the common features that emerge from these models.

As described in Schoenmakers et al. (1997), in order to retain the physical c_2 and s_2 terms which appear in Eq. (3.11), we keep the center position (R.A., Decl.) = (13h37m00s.9, $-29°51'57''$) (J2000; Walter et al. 2008) fixed for the Fourier decomposition. With the given center position and the prescribed rotation curve, we obtain the fit parameters $V_{\rm sys}$, PA, i, $V_{\rm rad}$ via the tilted-ring analysis as follows:

(i) $V_{\rm sys}(R)$ is determined while leaving all other parameters (PA, i, $V_{0,\rm rot}$, $V_{0,\rm rad}$) unconstrained.

The systemic velocity as a function of radius is found in this step and is shown in Fig. 3.4a. The red curve represents the results derived from the Effelsberg map, while the blue one indicates the results based on the THINGS map. The horizontal axis represents the galactocentric radius defined in the galactic plane for the fiducial case. The other two models show very similar behavior for $V_{\rm sys}$. The inner region ($R < 12.5'$) shows that the systemic velocity is approximately constant at $V_{\rm sys} = 505 \pm 1.3$ km s^{-1} for the Effelsberg map and at $V_{\rm sys} = 515.5 \pm 5$ km s^{-1} for the THINGS map. This is consistent with values 506 km s^{-1} found by HB81, 505 km s^{-1} by Comte (1981), 516 km s^{-1} quoted by de Vaucouleurs et al. (1991), 513 ± 2 km s^{-1} by Koribalski (2004) and 513 ± 2 km s^{-1} by (Miller et al. 2009).

Although our values seem to lie in the range reported in the literature, a systematic discrepancy ~ 10 km s^{-1} exists between our interferometric and the single dish map. In the outer region ($R > 12.5'$), the systemic velocity decreases with a rate of ~ -3.1 km s^{-1} arcmin^{-1}. The total drop in $V_{\rm sys}$ is more than 35 km s^{-1} at the radius of $25'$. Matthews et al. (1998) find that $\sim 77\%$ of late-type galaxies are lopsided. In particular, the extended disk of M83 appears to be heavily lopsided both in the HI distribution and the gas kinematics (HB81). Equation (3.10) hints that the drop in apparent $V_{\rm sys}$ could be contaminated by the terms, (A_1, D_1), associated with the lopsidedness.

In this Chapter, we view the systemic velocity as a constant and attribute the drop in $V_{\rm sys}$ to the

lopsidedness. The constant systemic velocity seen in the inner region leads us to adopt $V_{\rm sys} = 505$ km s^{-1} for the Effelsberg map and $V_{\rm sys} = 515$ km s^{-1} for the THINGS map.

(ii) With fixed $V_{\rm sys}$ and $V_{0,\rm rot}$ (D_0) as described by Eq. (3.13), PA and i are fixed, too. Note that $V_{0,\rm rad}$ is not fixed yet in this iteration, as involving $V_{0,\rm rad}$ leads to unstable results.

(iii) Subsequently we determine $V_{0,\rm rad}$ (B_0) from Eq. (3.2).

(iv) With a fixed set of parameters ($V_{\rm sys}, B_0, D_0, {\rm PA}, i$), the remaining Fourier coefficients are derived from Eq. (3.12).

Inclination and PA for the fiducial case are shown in Figs. 3.4b and 3.4c, respectively. The blue curves are the results extracted from the THINGS map and the red ones are from the Effelsberg map. As shown in Fig. 3.1b, the incomplete data in the outskirts of the THINGS map makes the fitting unreliable in this range. Thus, we only extract the fit parameters from the THINGS map itself for the area inside the radius $R < 12.5'$ (shown as the right vertical line). The black dash-dotted curve shown in Fig. 3.4b is the result by shifting the red curve upward by 3 degree. The black dash-dotted curve, which represents an extension of the blue curve, suggests that the disk can be divided into three distinct areas as indicated by the vertical lines, an inner disk ($R < 5.5'$), a transition zone ($5.5' < R < 12.5'$) and an outer disk ($R > 12.5'$). The inner disk and the outer disk have a well-defined and nearly flat inclination. Surprisingly, this nicely matches in the radial range between $6'$ and $12.5'$ (as indicated by the white ellipses in Fig. 3.1a) which coincides with the bright HI ring around the Holmberg radius. The implications of the misaligned direction of spin and the presence of ring will be discussed further in Section 3.5.

Except for a small shift in inclination, Fig. 3.4b together with Fig. 3.4c show that the PA and the inclination derived from the two different maps are in excellent agreement. It seems to be reasonable to 'extrapolate' the inclination and the PA for THINGS map by using the results from the Effelsberg map. Specifically, for the region outside the radius $R = 12.5'$, we have ${\rm PA}_{\rm THINGS} = {\rm PA}_{\rm Effelsberg}$ and $i_{\rm THINGS} = i_{\rm Effelsberg} + 3^\circ$. The results of this operation for our three different models are shown in Figs. 3.5a and 3.5b.

Eventually, the mass-weighted radial velocity, $\overline{v}_{\rm rad}$, and the mass flux, $\dot{\rm M}$, are evaluated in the following way:

$$\dot{\rm M}(R) \equiv \frac{{\rm d}{\rm M}}{{\rm d}t} = \int R\Sigma(R,\theta)V_{\rm rad}(R,\theta){\rm d}\theta, \tag{3.14}$$

$$\overline{v}_{\rm rad}(R) \equiv \frac{\dot{\rm M}(R)}{\int R\Sigma(R,\theta){\rm d}\theta}. \tag{3.15}$$

Note that the mass flux is evaluated pixel-by-pixel according to Eq. (3.14).

3.4.2 Results

In this Section, we describe the results of our analysis. We will discuss the implications of our findings in Section 3.5.

The overlap of Figure 3.1a and 3.1d shown in Figure 3.2 allows to compare structures in surface density with those in the velocity field. While the star forming disk ($< 5'$) is showing a normal circular motion, the twist in contours beyond the optical disk has a good correlation with the ring and the spiral features.

The presence of the ring structure is best visible in Fig. 3.3b, where the surface density as a function of radius is shown for the Effelsberg map (red line) and the THINGS map (blue line). We stress again that the flat part seen in the Effelsberg profile is an artifact due to the lack of small scale information. Note that the THINGS curve lies well below the Effelsberg one, suggesting the interferometry only picks up a small fraction of the diffuse gas in the extended disk. Second, a prominent ring structure is visible in the radial range from $6'$ to $\sim 12.5'$ (as indicated by the two vertical black lines in Fig. 3.3b). The column density peaks around $R = 10'$ and the structure can be further divided into an inner-declined region ($6' < R < 10'$) and an outer-declined region ($10' < R < 12.5'$). The inner-declined region matches nicely with bump in PA as seen in Fig. 3.4c. The ellipses shown in Fig. 3.1a mark the corresponding area of the ring. Outside the ring, the blue curve level off at 1 $M_\odot$ pc^{-2}. Third, as shown in Fig. 3.4b, the outer disk ($R > 12.5'$) and the inner disk ($R < 5.5'$) have a well-defined and flat inclination. The ring coincides nicely with the transition zone ($5.5' < R < 12.5'$) of the inclination shown in Fig. 3.4, suggesting a possibly important role of the ring for the gas kinematics in M83.

Figure 3.5 and Fig. 3.6 show (a) PA, (b) inclination, (c) $\overline{v}_{\rm rad}(R)$ and (d) $\dot{\rm M}(R)$ for the THINGS map and the Effelsberg map, respectively. In all models, the size of the radial bins used for the Fourier analysis, i.e., the width of the tilted rings, is $0.25'$. In each plot, the results of three different rotation curves with $V_{\rm max} = 160, 180, 200$ km s^{-1} are presented. In the outer disk, the radial shift seen in Figs. 3.5 and 3.6 is due to the different inclinations corresponding to the different models. A more inclined ring has a shorter minor axis projected on the sky and therefore introduces a radial shift along the minor axis.

In Fig. 3.5, the vertical lines mark the boundary ($R = 12.5'$) inside which PA and inclination are derived from the THINGS map itself while for the outer part we infer these quantities from the Effelsberg map as discussed in the previous Section. The Fourier coefficients are fitted for the harmonics $m = 0, 1, 2$ for the radial range to the left of the vertical line, while only the $m = 0, 1$ modes are considered for the outer region. This is due to the missing data points of the THINGS map in the outer disk. Inclusion of the harmonic $m = 2$ is unstable to Fourier decomposition for the THINGS map. In Fig. 3.6, however, we shows the result of deriving Fourier coefficients for

$m = 0, 1, 2$ over the entire Effelsberg map.

The Fourier decomposition described in the previous Section allow us to construct a map of $V_{\rm rad}$ and $V_{\rm rot}$ simultaneously. Figures 3.7a/3.7c and Figs. 3.7b/3.7d show the residual maps of $V_{\rm rad}/V_{\rm rot}$ for THINGS and Effelsberg map, respectively. The residual $V_{\rm rad}$ map is constructed via Eq. (3.7), while the residual $V_{\rm rot}$ is obtained from Eq. (3.8) with the contribution from $V_{0,\rm rot}$ (D_0), defined by Eq. (3.13), being removed. Given the fact that trailing arms are found to be ubiquitous in disk galaxies (de Vaucouleurs 1958; Pasha & Smirnov 1982; Pasha 1985), we also assume that the spirals appear in the THINGS map are trailing, i.e., the gas is rotating clockwise on the sky. This assumption combined with the observed $V_{\rm los}$ helps us to determine the back and the front sides of M83. The black ellipses in Fig. 3.7 are the same as the white ellipses shown in Fig. 3.1a, marking the ring structure for the fiducial case, which has $V_{0,\rm max} = 180$ km s^{-1}. Negative values seen in the $V_{\rm rad}$ maps indicate radial inflow, positive values radial outflow. Negative values shown in the residual $V_{\rm rot}$ maps indicate that the gas rotates slower than the bulk motion of the gas, positive values indicates faster rotation. We discuss the implications of these maps in the next Section.

3.5 Discussions

3.5.1 The HI Ring As An Angular Momentum Barrier

In this Chapter, we interpret the HI ring as a natural consequence of the conservation of angular momentum. The angular momentum carrying infalling gas spirals inwards until it hits its Kepler orbit. At this point, the gas cannot move further inward. This would naturally explain why and how the prominent HI ring forms. A direct and compelling kinematic evidence comes from Fig. 3.4b, where the ring itself serves as a transition zone connecting the outer disk and the inner disk, which have distinct inclinations. The misalignment of the rotation axis suggests that the filaments seen in the outer disk are very likely of intergalactic origin, not tidally stripped off from the inner disk.

Evidence supporting the hypothesis that gas flows further inwards from the ring to yet smaller radii comes from Eq. (3.5) and the shift in PA as indicated by the two short horizontal lines shown in Fig. 3.4c. As discussed in Section 3.3.1, the presence of the axi-symmetric radial velocity, $V_{0,\rm rad}$, shifts the actual position angle and changes the amplitude of apparent $V_{\rm rot}$. Assuming that the actual PA of the bump part is inferred from the bulk motions extracted from the Effelsberg data (red line), the presence of the radial velocity shifts the apparent PA as derived from the THINGS map toward 243° according to the blue curve at $R = 7.5'$. We thus get the following

relations for the fiducial model:

$$\sqrt{V_{0,\mathrm{rot}}^2 + V_{0,\mathrm{rad}}^2} = 180, \ [\mathrm{km\ s^{-1}}] \tag{3.16}$$

$$\tan(\psi) = \tan(236^\circ - 243^\circ) = \frac{V_{0,\mathrm{rad}}}{V_{0,\mathrm{rot}}}. \tag{3.17}$$

Solving these two equations numerically, one gets $V_{0,\mathrm{rad}} = -21.6$ km s^{-1} and $V_{0,\mathrm{rot}} = 178.7$ km s^{-1}. Comparing Fig. 3.3b and Fig. 3.4c, we find that the bump in the PA model lies in the inner-inclined region, i.e., between $R = 6'$ to $9'$. If we take the surface density 1.7 M$_\odot$ pc^{-2} also from $R = 7.5'$, using Eq. (3.14) yields an infall rate of 2.3 M$_\odot$ yr^{-1}. Note that this crude estimate does not take into account the diffuse gas recovered from the Effelsberg map. This inferred infall rate fits excellently to the star formation rate, 2.5 M$_\odot$ yr^{-1} of M83 (Walter et al. 2008; Kennicutt 1998). This is an example illustrating that the potential radial flow can be substantially underestimated by the tilted-ring analysis.

We have estimated the gas infall rate from the ring to the star-forming disk. To sustain the HI ring structure, gas accretion from outer disk must be able to compensate the gas consumption. If we assume that the gas consumed by star formation inside the ring is at a rate of 2.5 M$_\odot$ yr^{-1}, the globally averaged star formation rate (Walter et al. 2008). As mentioned above, the ring is formed by gas infall from the outskirts due to the conservation of angular momentum. The mass (THINGS map only) enclosed by the ring is 7.3×10^8 M$_\odot$. For the fiducial model, to form the ring in one orbital time, i.e., 450 Myr at $R = 10'$, one needs averaged infall rate of 4.1 M$_\odot$ yr^{-1} from the outskirts. This number also fits very well to the number, 2.5 ± 1.5 M$_\odot$ yr^{-1}, as inferred in the next Section.

3.5.2 Radial Inflow In The Outer Disk

Before applying the Fourier decomposition to either Eq. (3.11) or Eq. (3.12), one needs to determine values for position angle and inclination. The position angle and inclination shown in Figs. 3.5a and 3.5b are used for the Fourier decomposition for the THINGS map. The values for the radial range to the right of the vertical line are inferred from the Effelsberg map. Figure 3.5c shows the averaged radial velocity for the THINGS map and Fig. 3.5d the corresponding radial mass flux. In all models, we see a prominent radial inflow corresponding to the radii where the filaments in the outer disks are found. Depending on the models, the averaged radial velocity ranges from -5 to -60 km s^{-1}, which contributes a gas infall rate ranging from 0.5 to 4.0 M$_\odot$ yr^{-1}. The corresponding radial velocity and the radial mass flow for Effelsberg map are shown in Figs.3.6c and 3.6d, respectively. It shows a radial velocity ranging from -3 to 5 km s^{-1} and a radial mass flow from -1 to 2 M$_\odot$ yr^{-1}. The difference in the averaged radial velocity between the two maps indicates that the motion of the filaments seen in the THINGS map deviates signif-

icantly from the bulk motion, that is traced by the much lower resolution Effelsberg map data. To understand this in detail, we will focus in the following on the residual maps shown in Fig. 3.7.

The black ellipses shown in Fig. 3.7 mark the location of the ring structure ($6' < R < 12.75'$), which is consistent with the transition zone ($5.5' < R < 12.5'$) defined in Fig. 3.4. We reiterate that in the THINGS map, only $m = 0, 1$ is applied to the area ouside the ring. The lopsidedness ($m = 1$) causes negative values on the east side and positive on the other side. The infalling gas from the extreme outer disk is carrying its angular momentum towards its Kepler orbit. In order for the gas to be able to proceed to the inner disk, it must give some angular momentum to other gas particles that consequently move outwards. Therefore, an analysis involving higher harmonics is necessary to study possible mechanisms that lead to the angular momentum exchange. The area with negative values in both $V_{\rm rad}$ and the residual $V_{\rm rot}$ represent ranges where the angular momentum of the gas will be too small to allow the gas to remain at this particular radius. Gas in such regions will move inwards until it reaches its Kepler orbit. Gas in areas with opposite signs in $V_{\rm rad}$ and the residual $V_{\rm rot}$ might take part in epicyclic motion. Gas in areas with positive values in both $V_{\rm rad}$ and the residual $V_{\rm rot}$ might be a result of angular momentum exchange. Here, gas is moving outwards towards larger radii. It is interesting to see that the gas near the ring shows a typical signature of epicyclic motion, i.e., a 90° shift in phase between $V_{\rm rad}$ and the residual $V_{\rm rot}$.

A strong lopesidedness, $m = 1$, is seen in the outer disk of both THINGS and Effelsberg maps. Figure 3.7a shows gas infall with $V_{\rm rad} \sim -90$ km s^{-1} in the north-west corner and $V_{\rm rad} \sim 30$ km s^{-1} in the south-east corner. Compared to the residual $V_{\rm rot}$ shown in Fig. 3.7c, this implies that the gas in the north is moving inwards while the gas in the south-west is moving outwards. It is the non-zero mass-weighted radial velocity, ~ -30 km s^{-1} , that leads to a net inflow. On the other hand, for the Effelsberg map, only a small value of mass-weighted velocity is found for Fig. 3.7b, resulting in no obvious contribution to the gas inflow.

These results lead to several conclusions. First, as discussed in Section 3.3.1, the fitting procedure described in Section 3.4.1 can potentially eliminate the presence of axisymmetric radial flow. However, in the above, the asymmetry of $V_{\rm rad}$ found in the outer disk of THINGS map suggests an axisymmetric radial flow of -30 km s^{-1}. This is because the fit parameters for the outer disk in the THINGS map are inferred from the Effelsberg map. The motions of filaments inferred from the THINGS map deviate from the bulk motion inferred from the Effelsberg map, suggesting that the streaming flow plays an important role in channeling gas inwards. Adopting the fit parameters from single-dish data help us probe the presence of streaming motion seen in the inteferometry data. Second, with this averaged axisymmetric infall velocity -30 km s^{-1}, it takes about 720 Myr for the gas at the tip of north-west corner to travel 22 kpc to reach the HI ring, i.e., the filaments seen in the extended disk are likely transient. Third, deeper interferometric observations might help to allow to include the second harmonic in the analysis of the outer disk. The presence of the second harmonic might have an impact on the movement in the south-east filament.

3.5.3 The Inner Disk and The Transition Zone

Figures 3.5c and 3.5d show that on average the inner disk ($< 5'$) has a radial velocity of ~ -4 km s^{-1} and a mass inflow of 0.2 M$_\odot$ yr^{-1}. Note that the counterparts shown in Fig. 3.6c are virtually zero. This is expected because (i) the $V_{0,\rm rad}$ is eliminated in the fitting process as discussed in Section 3.3.1 (ii) for each ring, the azimuthally uniform mass distribution yields higher harmonics which make no contribution to the net inflow.

As shown in Fig. 3.3b, the transition zone can be further divided into an inner-inclined region ($6' < R < 10'$) and an outer-inclined region ($10' < R < 12.75'$), measured from the peak of the HI ring at about $R = 10'$. On the one hand, and as discussed in Section 3.5.1, the shift of PA appearing in the inner-inclined region might be a result of an axisymmetric radial inflow. The gas infall leads to a decreasing gas surface density at smaller radii. The cause of the inflow is unclear. On the other hand, we view the gas accumulating in the outer transition zone as result of the conservation of angular momentum. One might expect the gas in this range to stay there for some time before being channelled further inwards. Therefore, the ring might be a relatively static structure. However, as shown in Figs. 3.5c and 3.6c, the movement of the outer-inclined region appears to be model dependent and therefore uncertain in both maps. We obtain an outflow in the model with $V_{\rm max} = 160$ km s^{-1}, and inflow with $V_{\rm max} = 200$ km s^{-1} and a relative static ring with $V_{\rm max} = 180$ km s^{-1}. The model with a static ring justifies the choice of the fiducial model, $V_{\rm max} = 180$ km s^{-1}, $n = 0.8$, $R_{\rm max} = 4.5'$, if one views the ring as a result of conservation of angular momentum.

3.6 Summary

In this Chapter, we discussed evidence for an radial inwards gas flow in the extended disk of M83. We combine information extracted from interferometric data (THINGS map) as well as single dish data (Effelsberg map) to search for evidence of gas accretion of intergalactic origin. While the THINGS map offers a detailed picture of the small-scale structure of the HI gas in M83, the Effelsberg map provides a complete census of the diffuse HI emission and the bulk motions on larger scales. The Fourier analysis introduced in this Chapter is proven to be useful for extracting more information about the gaseous kinematics. We summarize our findings as follows:

1. M83 can be divided in three kinematically distinct parts, an inner disk, a ring structure (transition zone) and an outer disk. We interpret the ring as a natural result of conservation of angular momentum. This interpretation together with the fact that more than 80% of HI

gas sits outside the Holmberg radius motivate us to search for evidence of gas accretion onto the extended disk of M83.

2. The conventional tilted ring analysis used in Schoenmakers et al. (1997), Wong et al. (2004), Trachternach et al. (2008) and this Chapter tends to eliminate the contribution from the axisymmetric radial motion by introducing a phase shift and by changing the amplitude of apparent rotation velocity. Nevertheless, in Section 3.5.1, we interpret the angle shift in PA as the presence of the radial motion, which contributes a radial mass inflow of 2.3 $M_\odot$ yr^{-1} at the radius $R = 7.5'$, which excellently fits to the observed star formation rate, 2.5 $M_\odot$ yr^{-1} (Walter et al. 2008).

3. The PA and inclination used to extract the radial flow in the outer disk of THINGS map are inferred from the Effelsberg map, which offer the gaseous bulk motion on larger scales. It turns out that the motion of the filaments seen in the THINGS map are falling towards the ring with an avearged radial velocity ranging from -5 to -60 km s^{-1}, offering a net mass inflow of 2.5 ± 1.5 $M_\odot$ yr^{-1}. For the Effelsberg map, however, due to the low radial velocity over the entire map, no clear sign of inflow or outflow is found.

4. In Section 3.5.2, we infer that the filaments are falling inwards with an axisymmetric velocity of -30 km s^{-1}. This infalling filaments will then compensate the mass loss of the ring, making the filements in the extended disk transient structures.

5. From Fig. 3.7, we realize that the gas infall is far from uniform over the disk. The gas motion is complicated. The mechanisms that facilitate the exchange of angular momentum inside the ring is unclear. Detailed numerical simulations are required to understand the interaction between the diffused gas and the structures. Based on our results, we believe that streaming motion is the most likely and efficient way of chanelling gas toward the star forming disk.

6. We conclude that M83 is a growing disk galaxy. The huge gas reservoir in the outskirts is feeding this galaxy in the form of filament.

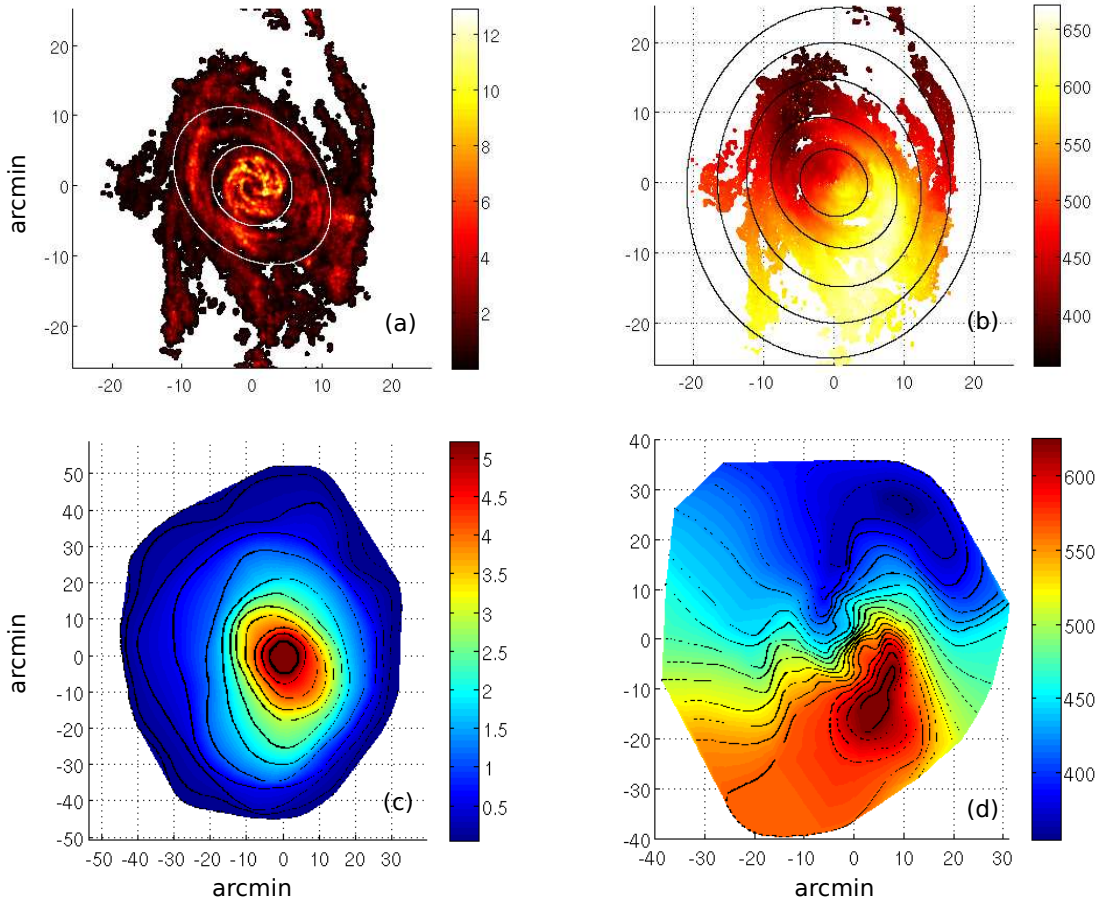

Figure 3.1: (a) The zeroth moment in units of $M_\odot$ pc^{-2} of the THINGS map. The white ellipses correpond to the black vertical lines ($R = 6', 12.75'$) shown in Fig. 3.3b, which define the region of the bright HI ring. (b) The first moment in units of km s^{-1} of the THINGS map. Each black ellipse is a result of a tilted circular ring at radii 5′, 10′, 15′, 20′, 25′, with a PA and an inclination extracted from the tilted-ring analysis. To associate structures with the corresponding radii, these ellipses serve as a coordinate system for the fiducial model with $V_{\rm max}$ = 180 km s^{-1}. (c) Reconstructed HI intentisty map in units of column density $M_\odot$ pc^{-2} of the Effelsberg map. (d) Reconstructed line-of-sight velocity, $V_{\rm los}$ [km s^{-1}], of the Effelsberg map. The contours shown in (c) and (d) are extracted from HB81 and are used to reconstruct the Effelsberg map.

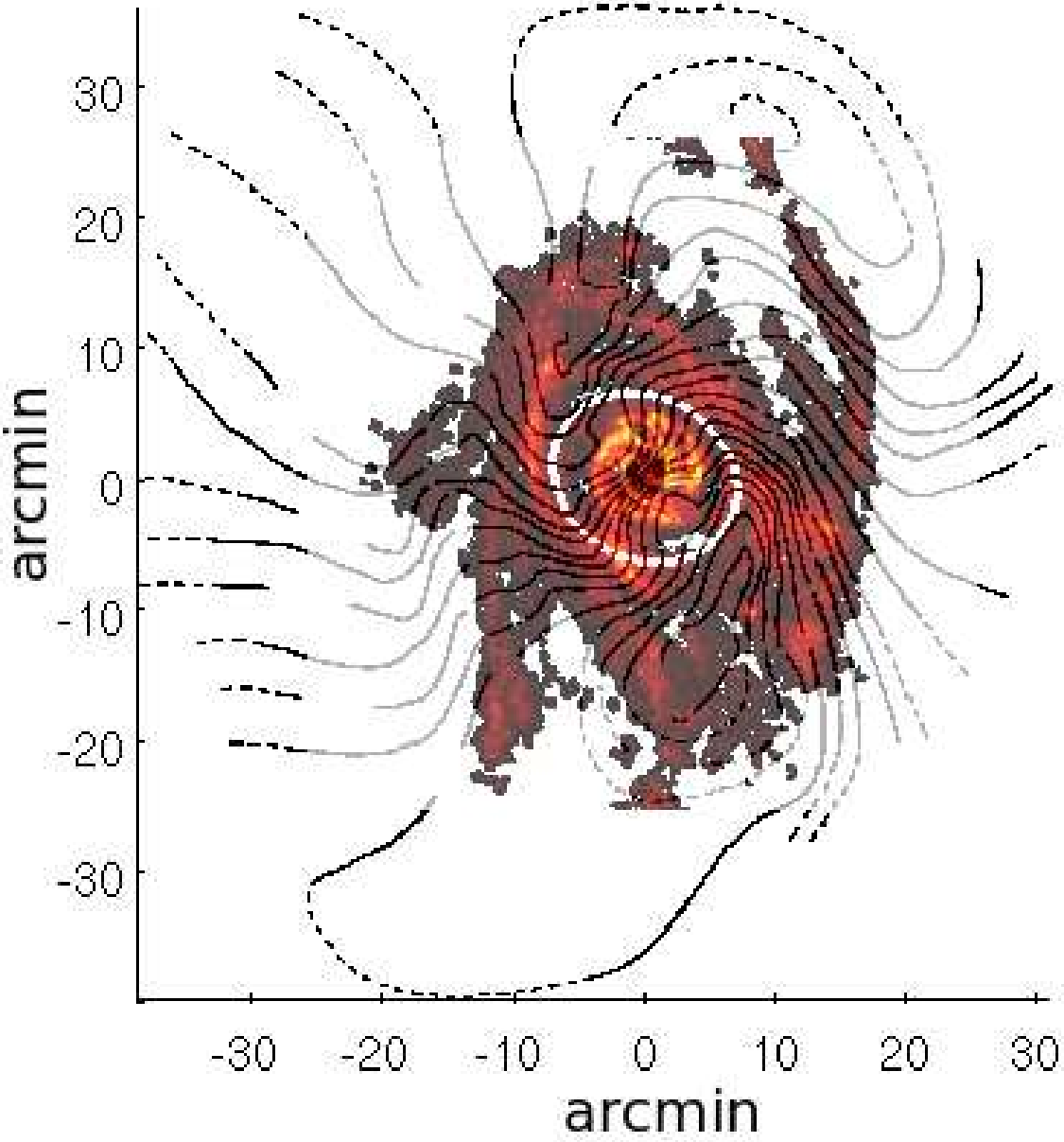

Figure 3.2: V_{los} contours from the Effelsberg map superimposed on the THINGS intensity map. The coincidence between the bending of the contours and the structures, i.e., the ring and the spirals, outside the Holmberg radius (shown as the white ellipse) motivates the search for gas inflow signatures based on HI kinematics.

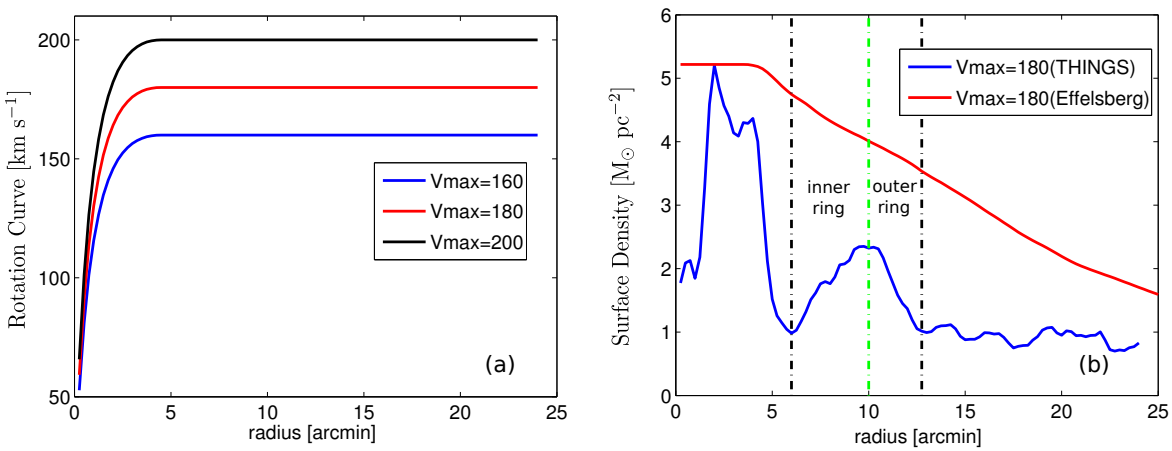

Figure 3.3: (a) The Brandt-type flat rotation curves as described in Eq. (13). Due to the low inclination of M83, we bracket the real situation with a range of different rotation curves and corresponding fit parameters from the tilted ring model. We assume $n = 0.8$, $R_{\rm max} = 4.5'$, $V_{\rm max} = 160, 180, 200$ km s^{-1}. As suggested in HB81, we take the model with $V_{\rm max} = 180$ as our fiducial case, which will then be justified in Section 3.5. (b) The averaged surface density of the THINGS map (blue curve) and of the Effelsberg map (red curve). They are extracted from the fiducial model. The black vertical lines situated at 6′ and 12.75′ define the region of ring structure, which is also shown as the area enclosed by the white ellipses in Fig. 3.1a and the black ellipses in Fig. 3.7. The green vertical line marks the location of the density peak and further divides the ring into an inner ring and an outer ring.

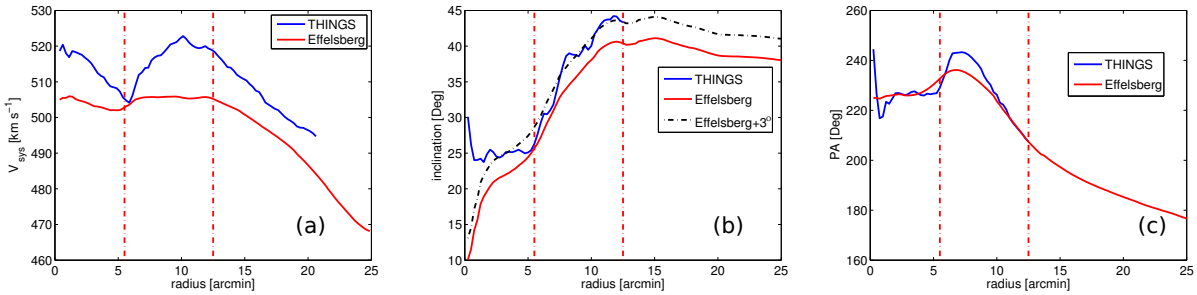

Figure 3.4: (a) System velocity extracted from the first step of Fourier decomposition described in Section 3.4.1. (b) The inclination and (c) the PA of the fiducial model, which has $V_{\rm max}$ = 180 km s^{-1}, for the THINGS map (blue curve) and the Effelsberg map (red curve). For the blue curve in (b) and (c), due to the lack of information in the outskirts of THINGS map, PA and inclination angles can be robustly derived only inside 12.5′. The area between the vertical lines at R = 5.5′ and 12.5′ is the transition zone, inside/outside which the disk has a nearly flat inclination. In (b), the black dash-dotted curve is a result of shifting the red curve upwards by 3 degree. This offset might be due to either the different spatial resolution of the two maps or the fact that the single dish map picks emission on larger spatial scales as well, possibly tracing slowly rotating gas above/below the midplane, which is thought to be the cause of the vertical velocity gradient found by Fraternali et al. (2005).

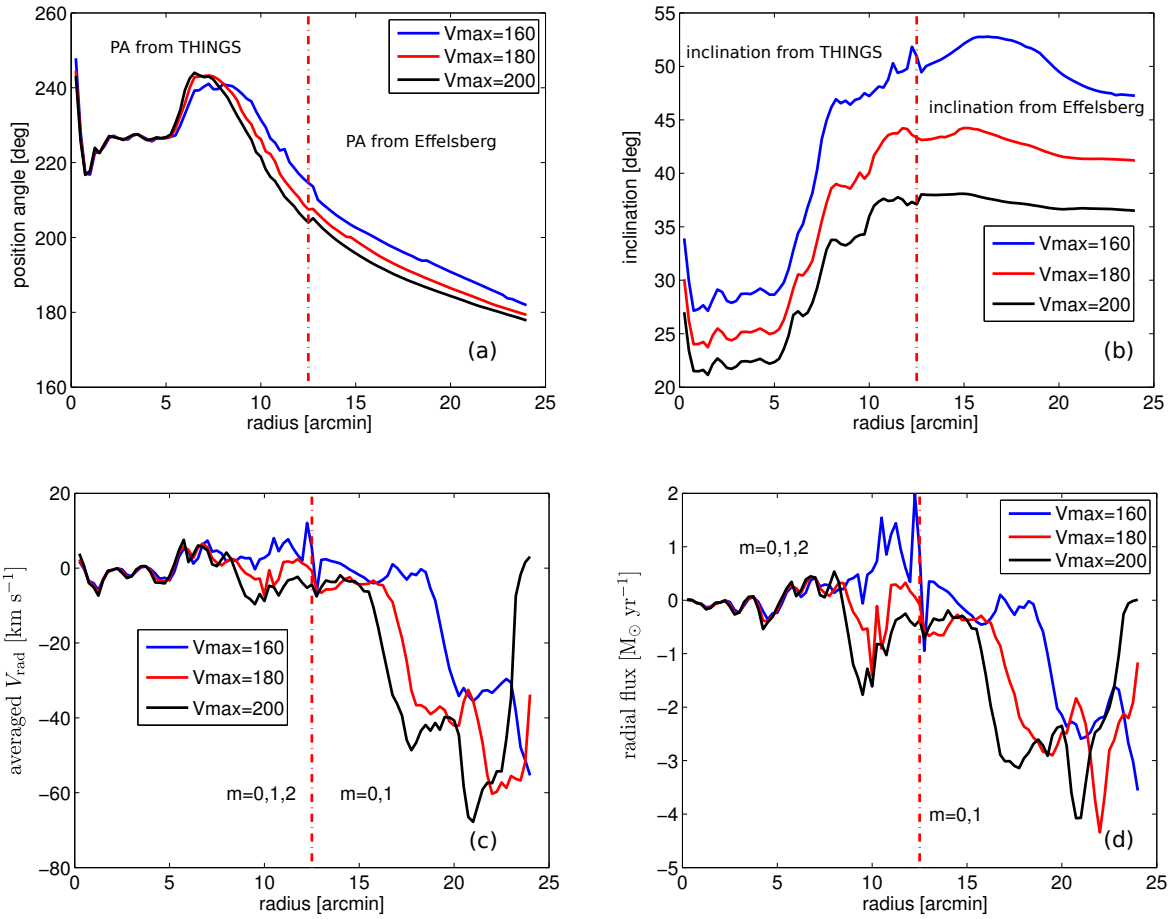

Figure 3.5: (a) PA and (b) inclination models used to infer radial motion of the gas in the THINGS map. (c) The inferred radial velocity. (d) The inferred radial mass flow. PA and inclination inside the vertical line ($R = 12.5'$) are extracted from the THINGS map, while in the other part we extrapolate these quantities from the Effelsberg map. The Fourier coefficients are fitted for the harmonics $m = 0, 1, 2$ for the radial regime to the left of the vertical line, while only $m = 0, 1$ for the outer parts of the map. In the outer disk, the radial shift is due the different inclinations corresponding to the different models. In all models, the common features are the prominent radial inflow in the outer disk, epicyclic motion in the transition zone (where the HI is organized into a ring like structure, see also Fig. 3.7 and an indication of moderate radial inflow in the inner disk.

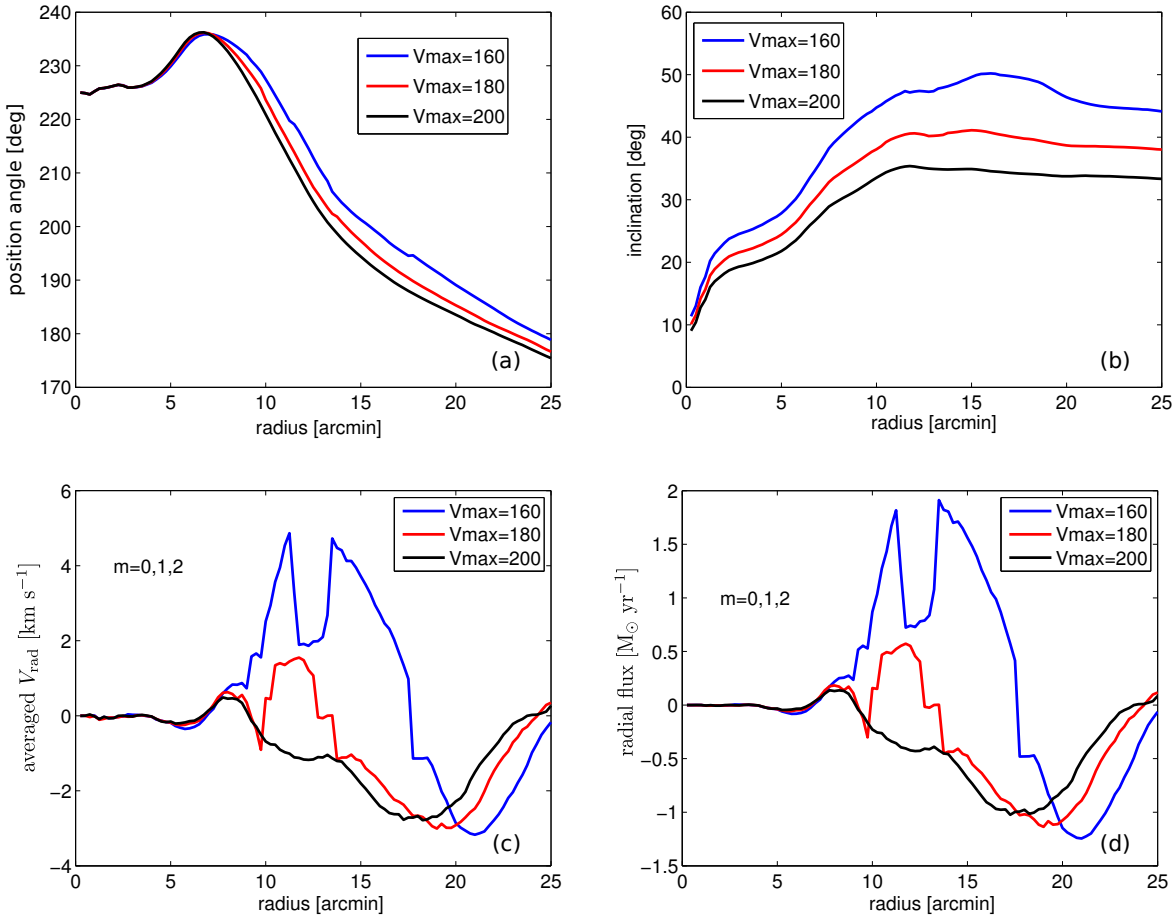

Figure 3.6: (a) PA and (b) inclination models used to infer radial motion of the gas in the Effelsberg map. (c) The inferred radial velocity. (d) The inferred radial mass flow. As opposed to the results based on the THINGS map shown in Fig. 3.5, these data show a much weaker sign of radial gas motion. The main features of these radial distributions, however, are very similiar to those based on the THINGS map. We find a radial flow with average radial velocity ranging from -3 to 5 km s^{-1} outside the Holmberg radius. No clear sign of radial motion is seen in the Effelsberg map.

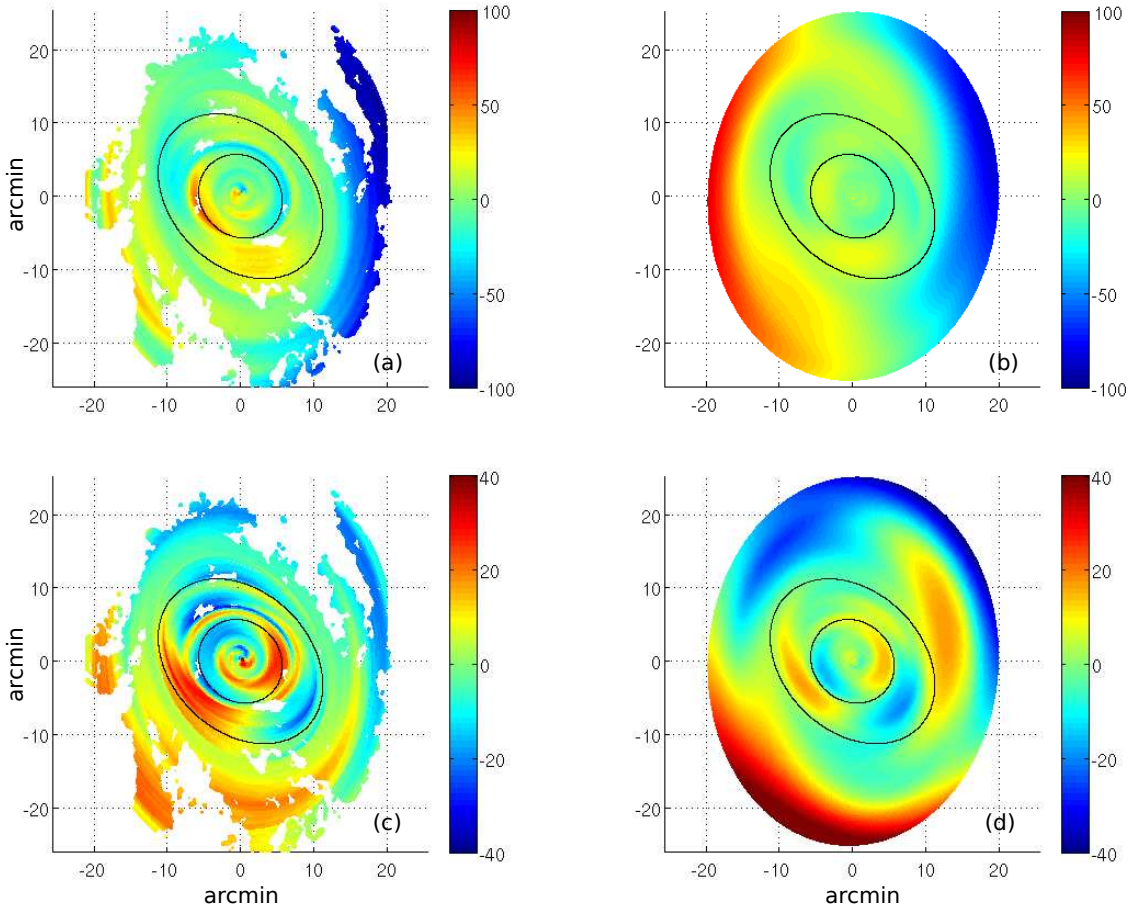

Figure 3.7: (a) $V_{\rm rad}$ for the THINGS map. (b) $V_{\rm rad}$ for the Effelsberg map. (c) Residual $V_{\rm rot}$ for the THINGS map. (d) Residual $V_{\rm rot}$ for the Effelsberg map. The black ellipses mark the location of the ring structure($6' < R < 12.75'$), which is consistent with the transition zone ($5.5' < R < 12.5'$) defined in Fig. 3.4.

Chapter 4

The Impacts of Spiral Density Waves On Gas Motions

4.1 Introduction

The majestic spiral arms observed in disk galaxies are composed of different constituents. In optical, the narrow luminous arms are due to the bright young stars which recently disperse the molecular cocoons from which they are born. Photographs taken in near infrared display the smooth, broad, sinusoidal older population which is the main body of the disk. In radio wavelength, 21 cm emissions from HI gas can be observed all the way out to the entended disk, making it an ideal tracer to study the gas dynamics and the mass distribution. The tight correlation between the luminous arms and the stellar arms indicates that the stellar dynamics and the gas dynamics are not completely separable.

The linear theory of density waves developed since 60s (Toomre 1964; Lin & Shu 1964) is meant to account for the formation of smooth sinusoial-varying stellar spirals. A number of theoretical works consistent with the quasi-stationary spiral structure (QSSS) framework has been carried out to investigate the gas response to the density waves. Roberts (1969) studies the nonlinear gas response to the superimposed gravitational field of linear spiral waves of stars and finds the shock solutions. Shu et al. (1972) propose a scenario that clouds of sub-critical mass get compressed to super-critical mass as passing through galactic shocks, ensuing the collapse of clouds and triggering the formation of stars. In this scenario spiral shocks play an important role on the process of star formation and on the formation of giant molecular clouds (GMCs). Searching for the evidence of the presence of shocks attracts a lot of attention since then. Velocity fields of spiral galaxies probed by CO, H_α and HI emission have shown strong streaming motions and velocity jumps across spirals (Shetty et al. 2007; Roberts & Stewart 1987; Visser 1978a,b). The presence of phase-lag between dust lanes in spiral arms and the ionized gas downstream to the shock (Tamburro et al. 2008; Roberts 1969) is also predicted in Roberts' picture. Following the

same line of Roberts (1969), Shu et al. (1973) study the ultra-harmonic resonances to understand the multiple-arm phenomenon. Woodward (1975) carries out one-dimensional time-dependent calcultions and finds the 4:1 resonances discussed in Shu et al. (1973). He concludes that unless the self-gravity is important, it is unlikely to explain the formation of spurs in terms of overlapping ultra-harmonics. Balbus (1988) attributes the substuctures to the growth of gravitational instabilities in preferred directions.

Although these works based on the assumption that spirals is tightly wound seem to be able to account for the formation of narrow dust lanes and luminous arms, near-infrared images taken by Spitzer Infrared Nearby Galaxies Survey (SINGS; Kennicutt et al. 2003) reveal a weath of substructures in dust, which is carried along with gas motions. Gas motions in real spiral galaxies is proved to be far more complicated. Secondary structures now coined with the name 'spurs' and 'feathers' emerging from the primary shock is prominent and pervasive over the disk. Numerical studies need to be conducted in order to fully understand the impacts of density waves on gas motions.

Kim & Ostriker (2002a) perform numerical simulations including self-gravity and magnetic fields to study the origin of spurs. They attribute the growth of spur to the so-called magneto-Jeans instability, an interplay between self-gravity, epicyclic motions and magnetic fields. Chakrabarti et al. (2003) perform two-dimensional self-gravitating simulations to study the role of ultra-harmonic resonances. They demonstrate that these features will be enhanced by the self-gravity of gas disk. The leading structures (referred to 'spur' in that paper) emerging from the primary shock are interpreted as a result of ultra-harmonic resonances. The wiggle instability found in Wada & Koda (2004), which is reminiscent of spurs protruding perpendicularly to the shock front observed in nearby spiral galaxies, suggests that spiral shock is potentially a major means of tapping turbulent energy from the huge energy reservoir stored in galactic rotation. They associate the wiggle instability with the Kelvin-Helmholtz instability resulted from the post-shock shearing flow. Kim et al. (2006) investigate the spiral shock evolution in a stratified disk. They conclude that the nonsteady flapping motions in the radial-vertical plane can effectively transform some of the rotational energy into random gas motions. They also conclude that the self-gravity and the magnetic fields play little role in this process. Dobbs & Bonnell (2006) perform non-selfgravitaing simulations using particle hydrodynamics (SPH) to study the spurs and feathers in spiral galaxies. They conclude that these substructures are natural results of sheared divergent flow. The necessary condition for this mechanism to work requires gas temperature less than 1000 K. Although the wiggle instability has been observed and proposed as a potentially major source of driving turbulence, its origin and efficiency are not well understood.

Recently, the second moment observed by The HI Nearby Galaxy Survey (THINGS, Walter et al. 2008) is interpreted as the presence of turbulence. Turbulence in the interstellar medium (ISM) is pervasive and plays an important role on regulating star formation on both large and small

scales (Mac Low & Klessen 2004). Turbulence decays very fast on a timescale comparable to one crossing time. One or more mechanisms have to be able to continuously pumping energy in order to sustain turbulence. Tamburro et al. (2009) attribute the velocity dispersion within the galactocentric radius r_{25} to the stellar feedback and to the magneto-rotational instability (MRI; Balbus & Hawley 1991, 1998; Sellwood & Moore 1999) for the regions beyond r_{25}, where the star formation is no longer active.

Spiral density waves as a means of powering the observed ISM turbulence on large scale has been proposed in Zhang (2002). CO and [C_I] observations for Carina molecular cloud complex suggest that spiral shocks may play an important role in the energy balance of molecular clouds. In this scenario, energy injected from large scales $\sim$ 1 kpc cascades downward to smaller scales. Energy injection from spiral shocks is estimated to be of the correct order to produce the observed size-line width relation for molecular clouds (Zhang et al. 2001).

It has long been recognized that in a compressible flow vorticity is not continuous across a shock (Truesdell 1952; Lighthill 1957; Hayes 1957; Kevlahan 1997). The idea that vorticity generated by shocks has been applied to explain many phenomena in different astrophysical contexts. Doroshkevich (1973), Binney (1974) and Chernin (1993) propose that the rotation of protogalaxies may originate from the vorticity created by shocks in the early universe. Fleck (1991) and Chernin & Efremov (1995) propose that galactic spiral shocks are responsible for the rotation of GMCs. In particular, Chernin & Efremov (1995) relate the spin of GMCs which have retrograde rotation with respect to the galactic rotation to large-scale spiral shocks. Kornreich & Scalo (2000) theoretically study the internal motions induced by the passage of a shock through a cloud. They conclude that interstellar shocks can pump enough energy to sustain supersonic internal motions in cold interstellar medium. Bonnell et al. (2006) numerically demonstrate that the internal motions of GMCs can be caused simply by the passage of an initially clumpy ISM through the spiral shock without resorting to any other external driving source. The observational, theoretical and numerical studies mentioned above suggest that the relationship between galactic shocks and ISM turbulence requires more attention.

It is well known that the presence of trailing spiral density waves transfers angular momentum outwards in stellar disks (Lynden-Bell & Kalnajs 1972). Gravitational torques excerting on stars reshape the distribution of stars and the angular momentum of disks on secular time scales (Lynden-Bell & Kalnajs 1972; Bertin 1983; Gnedin et al. 1995; Zhang 1996, 1998, 1999; Foyle et al. 2010). The gravitational torques excerted by stars also work on gas, transferring the angular momentum of gas disks outwards and driving gas flow inwards. Athanassoula (1992) studies the gas flow and the shape of dust lanes around galactic bars. The mass-weighted radial velocities she found range from -1 to -6 km s^{-1} depending on the models. Levy et al. (1996) study the angular momentum and the mass transfer of gas disks under the influence of external barred potential. They interpret the gas inflow as a result of angular momentum transfer from the

inner disk inside corotation to the outer disk. Transporting angular momentum outwards leads to the growth of the outer radius of the disk. Jogee et al. (2005) study the circumnuclear regions of a sample of barred galaxies. They conclude that over a galaxy's lifetime, a galaxy can experience numerous times of bar-driven gas inflow that results in the central mass concentration. Shetty et al. (2007) study the gas kinematics in the spiral arms and the interarms of M51 (NGC 5194). The radial and tangential streaming motions of M51 support the existence of spiral shock. They attribute the change of sign in the flux-weighted (mass-weighted) average radial velocity to the radially varying position angle and disk inclination, i.e., a warped or a twisted disk. Hunt et al. (2008) and Haan et al. (2009) study the gas inflow rate for galaxies selected from the NUclei of GAlaxies sample (NUGA). They find the gas inflow ranges from 0.01 to 50 $M_\odot$ yr^{-1} to fuel the galactic nuclear activity. Many works mentioned above is dedicated to stellar disks or gas motions in barred galaxies, the role played by spiral density waves, on the contrary, is less recognized and therefore becomes one of objectives in this Chapter.

In this Chapter, the impacts of density waves on gas motions are studied in detail. A global non-selfgravitating two-dimensional simulation with a very high spatial resolution is carried out with the adaptive mesh refinement magnetohydrodynamics code RAMSES (Teyssier 2002). A rigid-rotating spiral potential of stellar origin is superimposed on the axisymmetric background potential, which sustains the flat rotation curve. The gas is evolved isothermally with a temperature 10^4 K. Without the complex from stellar feedback, self-gravity, magnetic fields, we stress the pure hydrodynamic impacts of density waves.

This Chapter is structured as follows. In Section 4.2, the numerical model and the relevant parameters are presented. In Section 4.3, We quantify the level of velocity dispersion along the line-of-sight by tilting the two-dimensional disk plane with a moderate inclination. The results will be compared with observations. In Section 4.4, the evolution of radial velocity and angular momentum is quantified and studied. The generation of vortensity is discussed and evaluated in Section 4.5. A close look at the flow pattern around the shock and its implications to the formation of substructures is presented in Section 4.6. Discussions are put in Section 4.7. We summerize our results in Section 4.8.

4.2 The Model and Parameters

Two-dimensional, non-selfgravitating numerical simulations are performed to investigate the impacts of spiral density waves on gas motions. The initial surface density is exponential and is characterized by a scalelength $R_\mathrm{d} = 15$ kpc for warm HI gas. The gas disk is embedded in an

axisymmetric static potential, $\Phi_{\rm stat}$, which is described in cylindrical coordinates, (R, ϕ):

$$\Phi_{\rm stat}(R) = -V_0^2 \ln(a + R), \tag{4.1}$$

with $V_0 = 220$ km s^{-1} being the maximum value of rotation velocity and $a = 0.6$ kpc a parameter controlling the rising rate of the inner rotation curve.

A persistent, rigid-rotating, logarithmic density wave of stellar origin is then superimposed on the $\Phi_{\rm stat}$. The potential of this external field reads (Roberts 1969):

$$\Phi_{\rm sp}(R, \phi, t) = \Phi_{\rm sp,0}(R) \cos\left[m\left(\phi + \frac{1}{\tan(i)} \ln R - \Omega_{\rm p} t\right)\right], \tag{4.2}$$

with $\Phi_{\rm sp,0}$ being the strength of spiral, $m = 2$ the number of arm, t the time, $\Omega_{\rm p} = 20$ km s^{-1} kpc^{-1} the pattern speed and $i = 17^\circ$ the pitch angle. The strength is chosen to be 18% of the background radial force defined by (Shetty & Ostriker 2006):

$$\frac{\Phi_{\rm sp,0}(R) m}{V_{\rm rot}^2(R) \tan(i)} = 18\%, \tag{4.3}$$

with $V_{\rm rot}(R)$ being the rotation curve derived from Eq. (4.1).

The chosen strength is based on observations for spiral galaxies. In near infrared light, the amplitude of the smooth, sinusoidal arms composed of stars is somewhere between 18% and 60% (Rix & Zaritsky 1995) with respect to the azimuthal averaged surface bright. Recent observations suggest an average strength of 30% (Zibetti; private communication). In this Chapter, we adopt the conservative strength 18%. Although it is the lower bound of the range, this amplitude is stronger than the values commonly used in the literature. Thus, we expect that the gas response to the superimposed 'perturbation' spirals will be highly nonlinear and violent. The result is beyond the scope of linear analysis and is best studied numerically.

In the beginning of simulation, the external spiral perturbation grows adiabatically, i.e., the force increases gradually and stay at a constant strength after one orbital time ($\sim$ 280 Myr evaluated at the co-rotation). This simulation starts with a warm gas disk of temperature $T = 10^4$ K and is evolved isothermally. The computational box is 100 kpc on a side. Fourteen levels of refinement are used to cover the computational domain. To have the best spatial resolution for the inner disk, the 14th level, which corresponds the physical size of 6 pc, is forced to cover uniformly over the central region of 30 kpc in diameter. With this simple two dimensional setup we are allowed to reach a spatial resolution much higher than the observational one (THINGS, Walter et al. 2008), which ranges from 100 pc to 500 pc depending on the distance of galaxies.

The solid curve shown in Fig. 4.1 represents the angular speed, Ω, as a function of radius. $\Omega \pm \kappa/4$ are shown as the dashed curves, while $\Omega \pm \kappa/2$ are the dash-dotted curves. κ denotes the

	i	$<\sigma>$	Morph.	SFR
	(°)	[km s^{-1}]	Type	[M$_\odot$ yr^{-1}]
Obj. Name	(1)	(2)	(3)	(4)
NGC 628	7	8.0	S?	1.21
NGC 5194	42	17.7	Sbc	6.05
NGC 3351	41	10.6	Sb	0.71
NGC 4736	41.4	12.0	Sab	0.43
NGC 7793	50	11.4	Scd	0.51

Table 4.1: THINGS Target Galaxies. Spiral galaxies from THINGS explored by Tamburro et al. 2009. (1) inclination angle (de Blok et al. 2008); (2) HI mass-weighted median of the HI velocity dispersion; (3) morphological Hubble type (LEDA); (4) Star formation rate (SFR) (Lee 2006; Walter et al. 2008).

epicyclic frequency. The horizontal line represents the pattern speed $\Omega_p = 20$ km s^{-1} kpc^{-1}. The intersections of these curves with the pattern speed mark the locations of resonances, in the order of increasing radius, ILR 2:1 (2.6 kpc), ILR 4:1 (6.7 kpc), co-rotation (10.7 kpc), OLR 4:1 (14.6 kpc) and OLR 2:1 (18.5 kpc).

Since the spiral potential streches from the galactic center all the way to the outskirts of the disk, we can not avoid the mixing of resonance waves and forcing waves. Resonance waves are excited by Lindblad resonances. They are generated around the radii of resonances and propagate freely throughout the disk. The behavior of resonant waves is governed by the dispersion relation. On the other hand, the forcing wave is the type of wave investigated by Roberts (1969). Gas reacts to the external force, behaving like a forcing pendulum and evolves into the grand-design spiral shocks due to the nonlinear development. The interaction of these two type of waves can be seen in the later stage of evolution and will be discussed in Section 4.6.

4.3 Velocity Dispersion

Based on the second moment defined in Walter et al. (2008), thermal broadening, turbulence and beam smearing can all contribute to the apparent velocity dispersion. We notice that eight out of the eleven galaxies studied by Tamburro et al. (2009) are inclined more than 40°. For the sake of clarity, the data of five selected spiral galaxies in that paper are listed in Table 4.1. Among them, NGC 5194 (M51) is an extreme case with a high HI velocity dispersion. It has a relatively high inclination and is turning gas into stars at a high rate. This is probably due to the

tidal interaction with its companion NGC5195. NGC 628 is the most face-on disk galaxy in this sample. Although NGC 628 has a relatively high star formation rate (SFR) compared to the rest of galaxies apart from NGC 5194, it has the least velocity dispersion. NGC 3351, NGC 4736 and NGC 7793 have a relatively high inclination and a high velocity dispersion despite their low SFR. From this table, we have the following conclusions. First, the velocity dispersion is not positively correlated with SFR. Galaxies with higher star formation rate are not necessarily to have a higher velocity disperision. In fact, except NGC 5194, an anti-correlation is found between them. Second, galaxies with higher inclination tends to have a higher velocity dispersion. We incline our 2D disks with a moderate inclination angle 42° to examine how much the in-plane motions will be observed as turbulence along the line-of-sight.

4.3.1 The Generation of Synthesis Map

To compare the two-dimensional numerical results with the synthesis maps produced by interferometry, one needs to (i) project the in-plane motions along the line-of-sight for a given position angle and disk inclination (ii) downgrade the numerical resolution to match the observation one. In this Section, the spatial resolution of the two-dimensional maps is downgraded from 6 pc to 300 pc. Disk inclination, incl = 42°, is chosen to mimic the inclination of NGC 5194. We then do 'observation' for the numerical results and study the impacts of the density waves on the observed velocity dispersion.

Projecting the in-plane velocity along the line-of-sight (LoS) is done by (de Blok et al. 2008):

$$v_{\rm LoS} = -v_x \sin(\rm incl) \cos(\rm PA) + v_y \sin(\rm incl) \sin(\rm PA), \tag{4.4}$$

with v_x, v_y being the velocity field defined in the plane of galaxy and PA the position angle. The downgrade procedure is done as follows. The high resolution maps are covered with super-cells. Each super-cell consists of several micro-cells. For instance, a super-cell of 300×300 pc^2 contains 50×50 micro-cells of the size 6×6 pc^2. Thus for each super-cell we are able to define quantities such as the total mass (the zero moment), the mass-weighted LoS velocity (the first moment) and the mass-weighted LoS velocity dispersion (the second moment) as described in Walter et al. (2008) and (Tamburro et al. 2009). We define the 'observables' as follows:

$$I_{\rm sup} = \sum_j I_j, \tag{4.5}$$

$$v_{\rm sup} = \frac{1}{I_{\rm sup}} \sum_j v_{{\rm LoS},j} I_j, \tag{4.6}$$

$$\sigma^2_{\rm sup} = \frac{1}{I_{\rm sup}} \sum_j (v_{{\rm LoS},j} - v_{\rm sup})^2 I_j, \tag{4.7}$$

where $I_{\rm sup}$, $v_{\rm sup}$ and $\sigma_{\rm sup}$ denote the zeroth-, the first- and the second-moment of super-cells, respectively. I_j represents the mass/intensity of single micro-cell and j runs over all the micro-cells contained in a super-cell.

4.3.2 The Line-of-Sight Velocity Dispersion

We quantify the velocity dispersion under the influence of density waves. Figure 4.2 shows the evolution of the surface density (first row), line-of-sight velocity dispersion (second row) and the iso-velocity contours (third row) at t = 300 (first column), 450 (second column), 650 Myr (third column). When producing the maps of dispersion velocity in the second row, we adopt a thermal broadening of 8 km s^{-1}. The galactic planes shown in Fig. 4.2 are inclined with incl = 42°.

In Fig. 4.2a, the spiral potential has reached its full strength and the spiral shock is fully developed. The leading substructures, which are described as 'spurs' in Chakrabarti et al. (2003), protruding from the main shock are clearly seen in the inner disk. Overall, at this point, the flow pattern is still laminar. However, as shown in Fig. 4.2d, along the shocks the velocity dispersion can reach on average 10 km s^{-1} and even 25 km s^{-1} at some locations. Note that this dispersion velocity is purely due to the streaming motion in the post-shock regions. Further downstream to the shock, the flow pattern becomes smooth again. Thermal broadening is the major contributor to the velocity dispersion. The bending of the iso-velocity map (spider diagram) shown in Fig. 4.2g shows that the oblique shock deflects the incident flow with a sharp angle in post-shock regions. The streamlines of gas behind the shock change rapidly on the scales smaller than the size of super-cell and therefore contribute a substantial portion of velocity dispersion along the shock. Note that only a moderate inclination is needed to obtain this result.

In Figs. 4.2b and 4.2c, spiral shocks are no longer stable, developing chaotic substructures reminicent of the infrared images of M51 pictured by Spitzer space telescope (SINGS; Kennicutt et al. 2003). The flow is disturbed by the nonsteady shocks. The huge energy reservoir stored in rotation motions is transformed into local turbulent energy. Over time, the interarm gas is getting more chaotic. However, as shown in Fig. 4.2h and 4.2i, the overall flow pattern does not change

very much compared to Fig. 4.2g. This shows that the turbulent energy is only a small fraction of the total kinetic energy.

In figure 4.3, the mass-weighted velocity dispersion is calculated for the disk within a radius of 9 kpc over a period of 1.6 Gyr. The blue curve represents the kinematic velocity dispersion, $\sigma_{\rm kin}$. The red curve is the total velocity dispersion, i.e., $\sigma^2_{\rm tot} = \sigma^2_{\rm th} + \sigma^2_{\rm kin}$, where the thermal broadening with $\sigma_{\rm th} = 8$ km s^{-1} is taken into account. In the beginning 300 Myrs, as the strength of the spiral is turned on adiabatically, the thermal broadening dominates the turbulent energy. At $t = 330$ Myr, the shocks become unstable. Wiggle instabilities develop from the inner disk to the outer disk. The kinematic velocity dispersion keeps growing steadily over the next one Gyr. Eventually, it saturates at $\sigma_{\rm kin} = 11$ km s^{-1} and $\sigma_{\rm tot} = 13$ km s^{-1}. These result shows that the turbulence driven by nonsteady shocks alone can explain the observed level of velocity dispersion.

4.4 Angular Momentum Transport and Radial Motions

The presence of density waves not only tap turbulent energy from regular motions, it also redistributes the angular momentum and the mass over the disk. Figures 4.4 and 4.5 show the evolution of mass and angular momentum distribution as a function of radius. To avoid the boundary effect, which propagates with the sound speed (10 km s^{-1}), we trace the evolution of the disk within a radius of 35 kpc for 800 Myr.

Figure 4.4a shows the evolution of annular mass distribution and Fig. 4.4b the evolution of accumulated mass distribution. We notice that the evolution of the disk seems to be separated by the corotation ($R = 10.7$ kpc), around which the spiral shock vanishes. The total mass enclosed within corotation drops very little over time. Inside the corotation, the gas is transported toward the center of the galaxy, while for the region between corotation and OLR ($R = 18.5$ kpc), gas is efficiently transported to the outer disk. Once the wiggle instability sets in at $t = 330$ Myr, the gas distribution inside the corotation is far from uniform. Gas starts to converge or diverge at certain radii. In all, the gas distribution changes dramatically in a few hundred Myrs, a relatively short time scale compared to the secular evolution of stellar disk. Note also that after an evolution of 800 Myr, the gas distribution beyond $R = 33$ kpc remains intact.

Figure 4.5 shows the evolution of (a) annular angular momentum and (b) accumulated angular momentum. Overall, the angular momentum inside OLR (18.5 kpc) is efficiently transported to the outer disk. The disk inside corotation is losing and redistributing its angular momentum. Although the annular angular momentum beyond $R = 33$ kpc remains intact, from Fig. 4.5b, it seems that the gas disk is extracting angular momentum from the superimposed external spiral

potential. Nevertheless, the loss of angular momentum of the stellar density waves is insignificant to have a clear impact on the pattern speed, Ω_p. It is interesting to notice that in the outer disk, the mass distribution shown in Fig. 4.4a coincides with the distribution of angular momentum shown in Fig. 4.5a. On the contrary, this is not the case for the disk inside corotation. We discuss the implication of this result in Section 4.7.

Figure 4.6 shows the evolution of (a) mass-weighted radial velocity and (b) mass-weighted radial velocity in time-radius plane. Figure 4.6a is the horizontal cuts of Fig. 4.6b at $t = 0, 300, 600, 800$ Myr. Before the wiggle instability sets in, gas inside the corotation is moving inward with radial velocities $\sim -3 \pm 2$ km s^{-1}, while the gas between corotation and OLR (18.5 kpc) is moving outward subsonically ~ 5 km s^{-1}. However, the gas beyond the OLR is oscillating with supersonic speeds ranging from -20 to 20 km s^{-1}. This phenomenon is best visualized in Fig. 4.6b. Once the wiggle instability sets in at $t = 330$ Myr, the gas motion is severely disturbed in the inner disk. The sign of radial motion in the inner disk ($R < 5$ kpc) changes with radius.

4.5 Generation of Vortensity

Figure 4.7 shows the evolution of vorticity, $\omega \equiv \nabla \times \mathbf{v}$, with $\mathbf{v}$ being the in-plane velocity field, at t =300, 450, 650 Myr. The spur-like substructure protruding almost perpendicular to shocks is commonly seen in real spiral galaxies via the emissions of dust (Spitzer's 24 μm, Kennicutt et al. 2003) or HI (Visser 1978a,b). More precisely, eddies which are counter-rotating (retrograde) with respect to the spin of large scale flow are emerging from shocks.

In this Section, we justify the generation of negative vorticity semi-analytically. We stress that in a compressible flow, vorticity itself is not a conserved quantity. It is the vortensity or the potential vorticity, ω/Σ, with Σ being the surface density, that is conserved in a 2D smooth flow. However, with the presence of discontinuity, e.g., shocks, niether the vorticity nor the vortensity is conserved. Therefore, the Eq. (2.4) in Balbus (1988) and the Eq. (11) in Shetty et al. (2007) do not apply to a flow with shocks. Therefore, the dynamical impact of generated vortensity needed to be quantified and examined.

In Section 4.3, we have shown that density waves are capable of extracting turbulent energy from the regular rotation motions. For many reasons, vortensity turns out to be well suited to quantify this process. First, vortensity is a local quantity, measuring the circulation of every point, monitoring the flow change on small scales. Vortices are usually considered as a precursor of turbulence, representing the energy injection from large scales into small scales. Second, vortensity is a conserved quantity in a 2D smooth flow. This allow us to quantified the dynamical impact which is purely from shocks.

In general, the dynamics of vortensity in an invicid flow is governed by:

$$\frac{\mathrm{D}}{\mathrm{D}t}\left(\frac{\omega}{\rho}\right) = \left(\frac{\omega}{\rho}\cdot\nabla\right)\mathbf{v} - \frac{1}{\rho^3}\nabla\rho\times\nabla p, \tag{4.8}$$

with ρ being the volume density, p the pressure and $\mathrm{D}/\mathrm{D}t$ the material derivative. The baroclinic term, $\nabla\rho\times\nabla p$, on the right represents that the vortensity can be produced by the misalignment between the density gradient and the pressure gradient. This term is gone for barotropic gas in which pressure is a function of volume density. The first term on the right will vanish as well if the flow is two-dimensional. Thus, for a smooth, compressible, two-dimensional, barotropic flow, all terms on the right are gone, i.e., ω/ρ is a conservative quantity if we move along with a fluid parcel. In other words, for a flow in steady state, the iso-vortensity contours trace the streamlines.

However, the derivative in Eq. (4.8) breaks down as the fluid comes across a shock. Rankine-Hugoniot jump conditions has to be invoked to replace the derivative normal to the shock. Hayes (1957) gives out a general formulation to evaluate the vorticity generation by a curved shock in a non-uniform flow. Recent work by Kevlahan (1997) takes another route of derivation and reaches the same results. Following the notations used in Kevlahan (1997), we write down the main result as follows:

$$\delta\omega = \frac{\mu^2}{1+\mu}\frac{\partial C_\mathrm{r}}{\partial S} - \frac{\mu}{C_\mathrm{r}}\left[\left(\frac{\mathrm{D}\mathbf{v}}{\mathrm{D}t}\right)_s + \frac{C_\mathrm{r}^2}{1+\mu}\frac{1}{\rho}\frac{\partial\rho}{\partial S}\right] + \mu\omega, \tag{4.9}$$

with $\delta\omega \equiv \omega_\mathrm{b} - \omega_\mathrm{a}$ being the vorticity difference behind and ahead the shock, $\partial/\partial S$ the tangential derivative along the shock front, $C_\mathrm{r} = C - A$ the relative velocity between the shock speed, C, and the flow velocity normal to the shock front, A. The shock strength, μ, is defined by:

$$\mu = \frac{\rho_\mathrm{b}}{\rho_\mathrm{a}} - 1, \tag{4.10}$$

with ρ_b and ρ_a being the gas density behind and ahead the shock, respectively. Hereafter, quantities without subscript take the pre-shock values. To evaluate the jump of potential vorticity we have:

$$\delta\left(\frac{\omega}{\rho}\right) = \frac{\omega_\mathrm{b}}{\rho_\mathrm{b}} - \frac{\omega_\mathrm{a}}{\rho_\mathrm{a}} = \frac{\delta\omega}{\rho_\mathrm{b}} - \mu\frac{\omega_\mathrm{a}}{\rho_\mathrm{b}}. \tag{4.11}$$

Inserting Eq. (4.9) into Eq. (4.11) , the jump in vortensity then reads:

$$\begin{aligned}\delta\left(\frac{\omega}{\rho}\right) &= \frac{\mu^2}{(1+\mu)^2}\frac{1}{\rho}\frac{\partial C_\mathrm{r}}{\partial S} \\ &\quad -\frac{\mu}{1+\mu}\frac{1}{C_\mathrm{r}\rho}\left[\left(\frac{\mathrm{D}\mathbf{v}}{\mathrm{D}t}\right)_s + \frac{C_\mathrm{r}^2}{1+\mu}\frac{1}{\rho}\frac{\partial\rho}{\partial S}\right].\end{aligned} \tag{4.12}$$

For polytropic gas, $p = K\rho^{\gamma}$, with K being a constant and γ the polytropic index, Eq. (4.12) can be reduced to:

$$\delta\left(\frac{\omega}{\rho}\right) = \frac{\mu^2}{(1+\mu)^2}\frac{1}{\rho}\frac{\partial C_{\rm r}}{\partial S} - \frac{\frac{1}{2}(\gamma-1)\mu^2}{1-\frac{1}{2}(\gamma-1)\mu}\frac{1}{C_{\rm r}(1+\mu)\rho}\left(\frac{{\rm D}\mathbf{v}}{{\rm D}t}\right)_s . \tag{4.13}$$

Applying Eq. (4.13) to isothermal gas, where $\gamma = 1$, the baroclinic term on the right vanishes. The jump in vortensity across a shock for isothermal gas reads:

$$\delta\left(\frac{\omega}{\rho}\right) = \frac{\mu^2}{(1+\mu)^2}\frac{1}{\rho}\frac{\partial C_{\rm r}}{\partial S}. \tag{4.14}$$

This shows that the vortensity is not conserved as a gas flow passes through shocks. The jump in vortensity comes from the variation in the relative velocity, $C_{\rm r}$, along the shock.

To evaluate the generation of vortensity through Eq. (4.14), one needs to establish local coordinates along the spiral shock as shown in Fig. 4.8. The black arc is a part of a galactocentric circle and the dashed curve represents a section of a logarithmic spiral shock. $\hat{n}$ defines the normal unit vector with respect to the shock front, pointing the downstream side. The spiral tangent $\hat{s}$ is defined by $\hat{z} = \hat{s} \times \hat{n}$, with $\hat{z}$ the unit vector of rotation axis. The angle i between spiral tangent and the azimuthal unit tangent, $-\hat{\phi}$, then defines the pitch angle. In this cartoon, we assume the spiral shock is trailing, i.e., the mean flow is counterclockwise.

In addition to establishing the local coordinates, evaluating Eq. (4.14) also requires the information about the pitch angle of shock, i, shock strength, μ, relative velocity, $C_{\rm r}$, and the surface density ahead the shock, $\Sigma_{\rm a}$. Note that here we should replace the volume density, ρ, appearing in Eq. (4.14) with surface density, Σ. In Fig. 4.9a, we trace the location of shocks after an evolution of 300 Myrs. For the first order, the shock is well fitted with a logarithmic spiral (red line) of a pitch angle $i = 15°$, which is tighter than the superimposed one $i = 17°$. This is better visualized in log-polar coordinates $(\phi, \log R)$ as shown in Fig. 4.9b (Elmegreen et al. 1989). In this plot, logarithmic spirals become straight lines and the slope corresponds to the pitch angle. The spiral shock is offset and the phase lags behind the potential trough of the superimposed potential. This is also predicted by the semi-analytic work of Roberts (1969) although the WKB approximation is adopted there, i.e., the spiral has to be tightly wound. The pitch angle of the spiral shock does not change with time as the shock is developing, i.e., the pitch angle is well-defined over time until instability sets in. The shocks become weaker and eventually vanish as approaching the corotation (10.6 kpc). This is expected because the relative speed between the gas flow and the external perturbation becomes subsonic around the corotation. Interestingly, the ripple seen in Fig. 4.9b grows with time and has dynamical impact on the formation of substructure. This will be discussed in the next Section.

With the information shown in Fig. 4.8 and Fig. 4.9, we are ready to evaluate the generation of potential vorticity via Eq. (4.14). We extract the information we need after an evolution of 200 Myr. By this time, the shock is well-developed and well-defined as shown in Fig. 4.10a. Given the pitch angle of the shock, the velocity field can be decomposed into two components. One is perpendicular to the shock ($\hat{n}$ component, i.e., Fig. 4.10b) and the other is the parallel component ($\hat{s}$ component). Subsequently, we make azimuthal cuts for both surface density, Σ, and perpendicular velocity, A. We identify the quantities $\Sigma_{\rm a}$ and $A_{\rm a}$ just ahead the shock. This is done for radii ranging from 1 kpc to 8 kpc as shown in Fig. 4.11. Along the shock, the top panel of Fig. 4.11 shows the values of $\Sigma_{\rm a}$, the middle panel $A_{\rm a}$ and the bottom panel μ as defined in Eq. (4.10).

Evaluating Eq. (4.14) involves the tangential derivative, $\partial A_{\rm a}/\partial S$. To do this numerically, we smooth the $A_{\rm a}$ shown as the red line in the middle panel of Fig. 4.11 before the actual calculation. Because the pattern speed and the shape of spiral shock are well-defined, $\partial C/\partial S$ can be evaluated analytically. Putting $\Sigma_{\rm a}$, μ and $\partial(C-A)/\partial S$ together into Eq. (4.14), we have the result shown in Fig. 4.12. Note that we have replaced the volume density ρ with the surface density Σ in Eq. (4.14). The red line there represents the intrinsic disk vortensity if the disk is undisturbed.

From Fig. 4.12, first, we notice that in the inner disk ($1 < R < 3$) spiral shock is generating both positive and negative vortensity comparable to the intrinsic values (red line) evaluated as the disk is undisturbed. The variation in A_a is large as shown in Fig. 4.11b. This can be observed also in Fig. 4.10b, where the velocity component perpendicular to the shock front seems to be modulated with a standing wave. This might be a result of the interaction between the resonance waves emitted from ILR (2.6 kpc) and the forced waves. If we go further out ($3 < R < 8$), on average, the spiral shock is generating positive vortensity. Vortensity once created from the shock will continue to stay in the smooth region as described by Eq. (4.8) and interact with each other until they encounter the next shock, i.e., the effect of vortensity generation can be added up with time. As shown in Fig. 4.1, the angular speed increases with decreasing radius. This means that the gas in the inner disk is disturbed by shocks more than that in the outer disk and has more chances to accumulate generated vortensity. This is why the wiggle instability happens first in the inner disk. Second, the width of the fast ripple seen in Fig. 4.12 is about 100 pc, which is well resolved by the numerical resolution (6 pc). This gives the characteristic scale on which the vortices are generated by the curved shock.

This result shows that although by eye the flow looks laminar as shown in Fig. 4.10a, in fact, eddies on small scales have been continuously generated and enhanced along the shock. This is a clear sign of energy injection from large scales into small scales. Over time, the generated vortensity can not be ignored compared to the intrinsic vortensity, which is calculated from the initial condition. Obviously, the variation in $A_{\rm a}$ has a direct impact on generating negative vortentisty/vorticity.

4.6 Substructures and streaming motions

In this Section, we study the origin of leading structures protruding from the primary shocks as shown in Fig. 4.10a, of the ripple in pitch angle as seen in Fig. 4.9b and of the oscillation in shock strength seen in the bottom panel of Fig. 4.11.

The ripple in the pitch angle of shock as shown in Fig. 4.9b grows with time. This has a dynamical impact on the streaming flow. To understand this we study the post-shock flow pattern as shown in Fig. 4.13. We follow the picture described in Vishniac (1994) and set up coordinates (x, y) along a straight shock as indicated by the grey-dashed line. On top of it a sinusoidal displacement indicated by the red curve is superimposed and is described by $y = A\sin(kx)$, with A being the amplitude of the displacement and k the wave number. Given the pre-shock velocity $\mathbf{v} = v_x\hat{x} + v_y\hat{y}$ (the blue arrows), where $\hat{x}$ and $\hat{y}$ represent the unit vectors in x and y, we study the post-shock streaming motions (the black arrows).

To apply the Rankine-Hugoniot jump conditions, the pre-shock velocity is decomposed into $\mathbf{v} = v_\perp\hat{n}_\perp + v_\parallel\hat{n}_\parallel$, with $\hat{n}_\perp$ and $\hat{n}_\parallel$ being the perpendicular and the parallel unit vector with respect to the shock front, respectively. The posk-shock streaming motion is expressed with a prime $\mathbf{v}' = v'_\perp\hat{n}_\perp + v'_\parallel\hat{n}_\parallel$. The relation between $\mathbf{v}$ and $\mathbf{v}'$ can be found in Appendix A.7.

We assume that the velocity change in the pre-shock region due to the bending of the shock is relatively minor compared to the background flow. This is valid when the amplitude of the ripple is relatively small compared to the wavelength. We further assume that the flow is in a quasi-steady state, changing slowly relative to the dynamical time. The resulting flow pattern in the post-shock region then looks like the black solid arrows shown in Fig. 4.13 reminiscent of the nonlinear thin shell instability (NTSI) discussed in Vishniac (1994). We leave the discussion regarding NTSI to Section 4.7.

Figure 4.14a is an example showing how a small ripple in pitch angle deflects the streamling flow. The arrows there represent the directions of the streamlines, which is calculated via Eqs. (A.30) and (A.31), in the post-shock area. Note that the scales of x-axis and y-axis are not equal in order to illustrate the idea clearly. In this case, the wavelength and the amplitude are set to be $\lambda = 1$ kpc and $A = 0.015$ kpc, respectively. The incident flow comes in with the velocity $v_x = -172$ and $v_z = 53$ km s^{-1}, i.e., an incident angle of 73° corresponding to the pitch angle 17°.

From Fig. 4.14a, first, we notice that the small ripple in pitch angle leads to the separation or aggregation of streamlines because of the different incident angles with respect to the curved shock. The aggregation of streamline is clearly seen in Fig. 4.14b. These streamlines are set off along the x-axis with a uniform spacing 50 pc. Comparing to Fig. 4.10a, we are able to identify that the leading arm structure is simply the result of congestion of streamlines. Furthermore,

because the incident angle with respect to the shock is changing due to the presence of ripple in pitch angle, the shock strength is expected to oscillate along with the ripple. One can envision that the resulting shock is stronger on the head-on side and weaker on the leeside as shown in Fig. 4.15, where the blue curve represents the shock and the dash-dotted line the Mach number, $M_{\rm a}$, of the perpendicular velocity with respect to the shock. This explains the variation of shock strengh seen in the bottom panel of Fig. 4.11. The variation in shock strength can be easily a factor of two even with a small amplitude in ripple. The shock vanishes when the $v_\perp$ on the leeside becomes subsonic.

The analysis in Appendix A.7 breaks down at the sonic point, which is before the sigularity of Eq. (A.31). This is because the shock no longer exists when $v_\perp$ is subsonic. The breakdown of Eq. (A.31) at the sonic point implies that the ripple in pitch angle cannot grow arbitrarily. The denominator of Eq. (A.31) indicates that the variation of shock strength is very sensitive to the wavelength. Shorter wavelengths cause the shock strength to oscillate more violently. This explains why the wiggles always develop from smaller scales.

The cartoon shown in Fig. 4.13 combined with the post-shock flow pattern in Fig. 4.14a gives the clue on how the retrograde eddies (negetive vortices) seen in Fig. 4.7b and Fig. 4.7c are generated. The post-shock flow is deflected radially inward, following the curve of ripple, depositing linear momentum in the convex part of shock (with respect to the incident flow). The change in linear momentum then exerts a force on the shock, pushing the valley (with respect to the post-shock flow) backward and therefore enhancing the ripple. Furthermore, Coriolis force also tends to turn the radially inward flow retrogradingly. All these effects make the generation of negative vortices a natural result.

We can have a close look at this phenomenon from the results of simulation as shown in Fig. 4.16 where the surface density (contours) is overlapped with the velocity residual (arrows) after subtracting the mean velocity of these images. Both images show a square of 1×1 kpc^2 excerpted from the full disk in order to study the flow pattern around the shocks. The mean velocity of both images is counterclockwise. The contours represent the iso-density, the redder the denser. The locations where the residual velocity converges coincide with the high densities, e.g., shocks and spurs. Figure 4.16b, unlike the velocity field seen in Fig. 4.16a, shows a pattern of negative vorticity. A spur emerges at the sharp corner as a result of the crowded streamlines as discussed in Fig. 4.14a.

4.7 Discussions

4.7.1 Velocity Dispersion

Without energy sources from stellar feedback, self-gravity and magnetic fields, we have shown that the presence of nonsteady spiral shock alone is able to drive velocity dispersion with a level comparable to the second moment observed in THINGS maps (Walter et al. 2008). Kim et al. (2006) perform three-dimensional, magnetized, self-gravitating simulations for a local section of a stratified disk. They investigate the interstellar turbulence driven by the flapping motions in the radial-vertical plane. They find that most of the turbulent energy is in-plane ($\langle\sigma_x\rangle \sim \left\langle\sigma_y\right\rangle \sim 2\langle\sigma_z\rangle$). The presence of the self-gravity and magnetic fields contributes little to the random motions. To 'observe' the in-plane turbulence, one needs to tilt the galactic disk with an inclination in order to measure along the line-of-sight. In Section 4.3, we conclusively show that a moderate inclination is enough to contribute a substantial portion of observed HI turbulence. This result can account for the positive correlation between the disk inclination and the observed velocity dispersion.

These two- and three-dimensional works seems to support the galactic shock pump scenario proposed by Kornreich & Scalo (2000). In their picture, galactic shocks can be of different scales ranging from superbubbles down to the protostellar winds. The anisotropy in turbulent energy is due to the anisotropy in the energy reservoir, i.e., most of the energy is stored in the in-plane rotation motions. Although this mechanism has been proposed almost one decade ago, we are the first to quantify this scenario and compare our results to the observation data on the galactic scale. While in this Chapter we stress that shock driven turbulence should not be overlooked, we do not attempt to degrade the importance of other energy sources, i.e., stellar feedback, magnetic fields and so on. For instance, in M51, we believe that both stellar feedback and shock driven turbulences are important. However, it requires further detailed simulations involving stellar feedback to quantify which mechanism dominates the budget of turbulent energy in different environments, i.e., star-burst galaxies and galaxies with normal star formation rate like our Milky Way.

4.7.2 Nonsteady Shocks

It is evident that a nonsteady shock efficiently stirs the flow locally and randomizes the regular rotation motion. Wada & Koda (2004) attributes the 'wiggle instability' (spurs) to the Kelvin-Helmholtz instability (KH instability, hereafter). Kim & Ostriker (2002a) propose that the magneto-Jeans Instability (MJI, hereafter) is responsible for the growth of perturbation since

the magnetic tension forces from embedded field lines tend to counteract the Coriolis forces, which serve as a stable agent for disk stability. Recall the role played by the epicyclic frequency in Toomre's criterion $Q = c_s\kappa/(\pi G\Sigma)$.

Kim & Ostriker (2006), in their shearing box simulations, show that a magnetized spiral shock in a thin disk is unstable to MJI in both two- and three-dimensional calculations, while the wiggle instability is suppressed in their three dimensional models. However, their results cannot be compared directly to the work of Wada & Koda (2004) for the following reasons. First, the strength of spiral perturbation adopted in Kim & Ostriker (2006) (5 to 10%) is much weaker than that used in Wada & Koda (2004)($\sim$ 110%). The observation strength (18%~60%, Rix & Zaritsky 1995), however, is much stronger than the former but much weaker than the later. Second, as we will discuss below, a full-disk simulation is critical to capture the secular evolution of the streaming lines, which in turn has dynamical impact on the formation of wiggle instability. Nevertheless, in the following, by a simple Galilean transformation we argue that KH instability described in Wada & Koda (2004) is not likely to be responsible for the wiggle instability.

We use the same picture argued in Wada & Koda (2004) as shown in Fig. 4.17. First, if we ignore the curvature of the shock, in the outer disk, the velocity field appears to be uniform in the pre-shock region because of the flat rotation curve. A streamline entering at point A is deflected with a post-shock velocity $\mathbf{v}$ and is accelerated to $\mathbf{v}'$ at point B. At point C, the deflected post-shock velocity is the same as A due to the uniform pre-shock velocity and the straight shock. If we sit in an inertial frame within which the tangential velocity with respect to the shock vanishes, the velocity field will then look like the red arrows. In this frame, we do not expect the KH instability to occur despite the black arrows seen before the Galilean transformation indeed indicate a velocity gradient (shear) in the direction normal to the shock. Second, even if the KH instability does happen as described in Wada & Koda (2004), the post-shock flow as shown in Fig. 4.17 suggests prograde vortices rather than retrograde ones. Third, the curvature of the shock increases with decreasing radius, the wiggle instability occurs first in the inner disk, ignoring the curvature of the shock in the inner disk needs to be justified.

Vishniac (1994) studies the nonlinear instability in shock-bounded slabs, which is called nonlinear thin shell instability (NTSI). The displacement is enhenced because the positive momentum with respect to the incident flow tends to accumulate in the valley of the ripple, i.e., the concave part with respect to the incident flow. In the case of shock bounded slabs, this mechanism has to compete with two stabilizing effects. One is the ram pressure arising from the head-on impact of the confined flow. The other comes from the fact that the post-shock subsonic flow tends to diverge on the convex surfaces and converge on the concave surfaces.

In many ways the flow pattern underlying the spiral shocks discussed in this Chapter is different from the scenario discussed in Vishniac (1994). First, the shock is highly oblique with a very

large incident angle, i.e., a small pitch angle. Thus the post-shock flow is still hightly supersonic. Second, in a frame co-rotating with the pattern speed, the flow is subject to the Coriolis force. This force will then lead the radial inflow to rotate retrogradingly. Third, the post-shock flow encounter the subsequent shock on a regular basis because of the circular motion. The generated vorticity discussed in Section 4.5 will then be added up everytime the flow passes through the curved shocks.

In Fig. 4.14, we have shown that the small ripple in pitch angle is responsible for the convergence and the divergence of streamlines. The diverging supersonic flow works like a converging-divering nozzle, exerting a thrust backward on the shock. The diverging supersonic gas is accelerated, gaining angular momentum. On the other hand, convering supersonic gas is decelerated, pulling the shock further downstream. Unlike the subsonic post-shock flow discussed in Vishniac (1994), which tends to stabilize the growth of ripple, the supersonic post-shock flow enhances and deforms the shocks as seen in Fig. 4.16b. However, as discussed in Section 4.6, the ripple cannot grow arbitrarily since it has a huge impact on the strength of the shock. The substructures are then the natural results of the deformation of shock, Coriolis force and the negative vorticity generated by the oscillation in A_a. In this picture, the growth of ripple is limited and localized, making the shock unsteady rather than an unstable runaway.

4.7.3 Angular Momentum Transport and Radial Motions

For gaseous disks, it has long been recognized that the gaseous spiral density waves excited by periodic external perturbers can transpoart angular momentum outward (Goldreich & Tremaine 1979, 1980). This theory has been successfully applied to explain the formation of Saturn's ring (Goldreich & Tremaine 1978a,b; Shu et al. 1985a,b). For more general disks, theoretical works of Yuan & Kuo (1997) and Griv et al. (2008) show that density waves carrying negative angular momentum excited at ILR can transport mass inward, while the waves carrying positive angular momentum excited at OLR can transfer mass outwards. Their works are based on asymptotic approximation, i.e., tightly wound spirals.

A number of numerical works has been performed for two-dimensional non-selfgravitating disks to understand the interaction between the barlike potential and the gaseous disk (Huntley et al. 1978; Sanders & Tubbs 1980; Schempp 1982; Athanassoula 1992; Levy et al. 1996). Athanassoula (1992) find that although the variation in radial velocity can be very large (± 120 km s^{-1}), the mass weighted radial velocity can be only $-1 \sim -6$ km s^{-1}. Contrast to many works done for barred galaxies, the role played by stellar spiral density waves on gasdynamics is less recognized.

As shown in Section 4.4, the gas disk suffers a dramatic redistribution in mass on a very short time scale. In particular, the gas between corotation and OLR gains radial momentum and moves

outward as a density wave with supersonic speeds as shown in Fig. 4.6. This explains why the mass distribution in the outer disk coincides with the angular momentum distribution. These supersonic waves quickly dissipate their energy during the outward moving and decrease their angular velocity due to the conservation of angular momentum. Eventually, the gas reverses their radial velocity back toward the center of the galaxy. It is interesting to see that the gas inside OLR is accumulated just outside the OLR, moving back and forth in the outer disk. The peroid of cycle roughly fits the epicyclic frequency estimated at $R = 25$ kpc (~ 500 Myr).

As shown in Fig. 4.6, in the inner disk, once the wiggle instability sets in, the sign of radial velocity changes with radius. This phenomenon is observed for M51 and is interpreted as a result of a warped or a twisted disk (Shetty et al. 2007). However, in our simulation, this can be also interpreted as a result of wiggle instability.

4.8 Summary

We perform a two-dimensional, unmagnetized, non-selfgravitating simulation to investigate the impacts of spiral density waves on gas motions. An exponential gas disk is initialized with a temperature 10^4 K and is evolved isothermally. A stellar density wave with a strength 18% the background radial force is superimposed as the a rigid-rotating perturber. We follow the nonlinear response of the gas to quantify the velocity dispersion, angular momentum transport, radial motions and the generation of vortensity. We qualitatively describe the formation of leading substructures, the enhancement of ripple in pitch angle and its impact on shock stability. We summarize the main results as follows:

1. We downgrade the numerical resolution from 6 pc to 300 pc to mimic the observational spatial resolution of THINGS. Line-of-sight velocity dispersion as defined in Walter et al. (2008) is calculated for the simulated spiral galaxy tilted with a moderate inclination 42°. We conclude that the presence of the nonsteady spiral shocks is capable of tapping turbulent energy comparable to the observed level of velocity dispersion from the rotation motions.

2. The presence of the stellar spiral density waves can change the gaseous surface density profile dramatically on a relatively short time scale (a few hundred Myr). Our simulation confirms that the gas nonlinear response to the superimposed stellar spiral density wave tends to transport angular momentum outward. Before the wiggle instability sets in, the gas inside corotatin steadily moves inward by expanding the outer radius of the disk. Once the wiggle instability occurs, the gas in the inner disk is severely disturbed, resulting in the

sign change in the radial velocity. This result leads to the gas compression and relaxation over different radii.

3. Based on the work of Kevlahan (1997), we derive the formulation to evaluate the generation of vortensity along a logarithmic shock. We stress that the vortensity is not conserved with the presence of shocks. We quantify the generation of vortensity semi-analytically and find that both positive and negative vortices can be generated along shocks as also seen in the later stage of evolution shown in Fig. 4.7. The generation of vorticity is not ignorable compared to the intrinsic vortensity calculated from the initial condition.

4. In the picture of Vishniac (1994), we analyze the dynamical impacts of the small ripple seen in pitch angle. The interaction between density waves emitted from ILR and the spiral shocks initiates the ripple in pitch angle, which then enhances itself due to the supersonic post-shock flow pattern. However, the analysis in Appendix A.7 shows that the amplitude of the ripple cannot grow arbitrarily. The shock strength is shown to be very sensitive to the wavelength and the amplitude of ripple in pitch angle. We also correlate the flow converging and diverging in the post-shock region to the leading structure which is usually interpreted as the 4:1 resonance. In this Chapter, we consider the formation of spurs and negative vortices as a result of the conspiracy between the shock deformation, the generation of negative votensity and the Coriolis force.

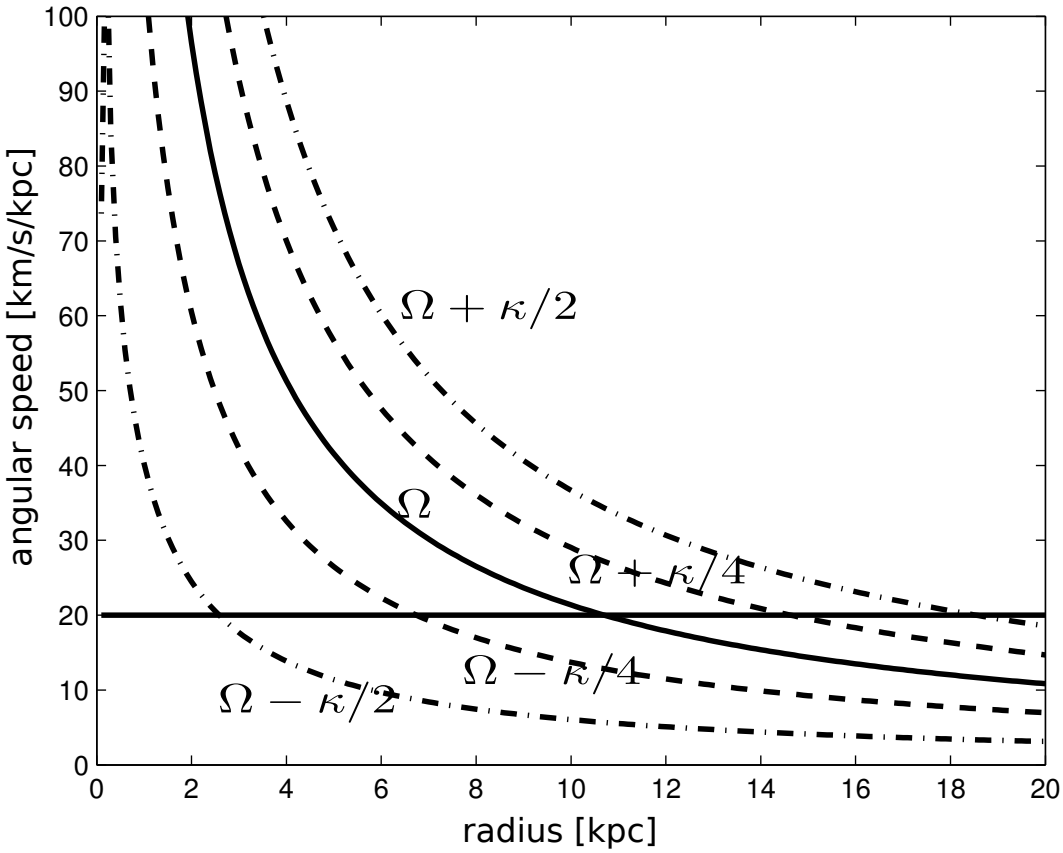

Figure 4.1: The solid curve represents the angular speed, Ω, as a function of radius. $\Omega \pm \kappa/2$ are shown as the the dash-dotted lines, while $\Omega \pm \kappa/4$ the dashed lines. The pattern speed, $\Omega_p = 20$ km s^{-1} kpc^{-1}, is shown as the horizontal line. The intersections marks the locations of resonances (from left to right) ILR 2:1 (2.6 kpc), ILR 4:1 (6.7 kpc), co-rotation (10.7 kpc), OLR 4:1 (14.6 kpc) and OLR 2:1 (18.5 kpc).

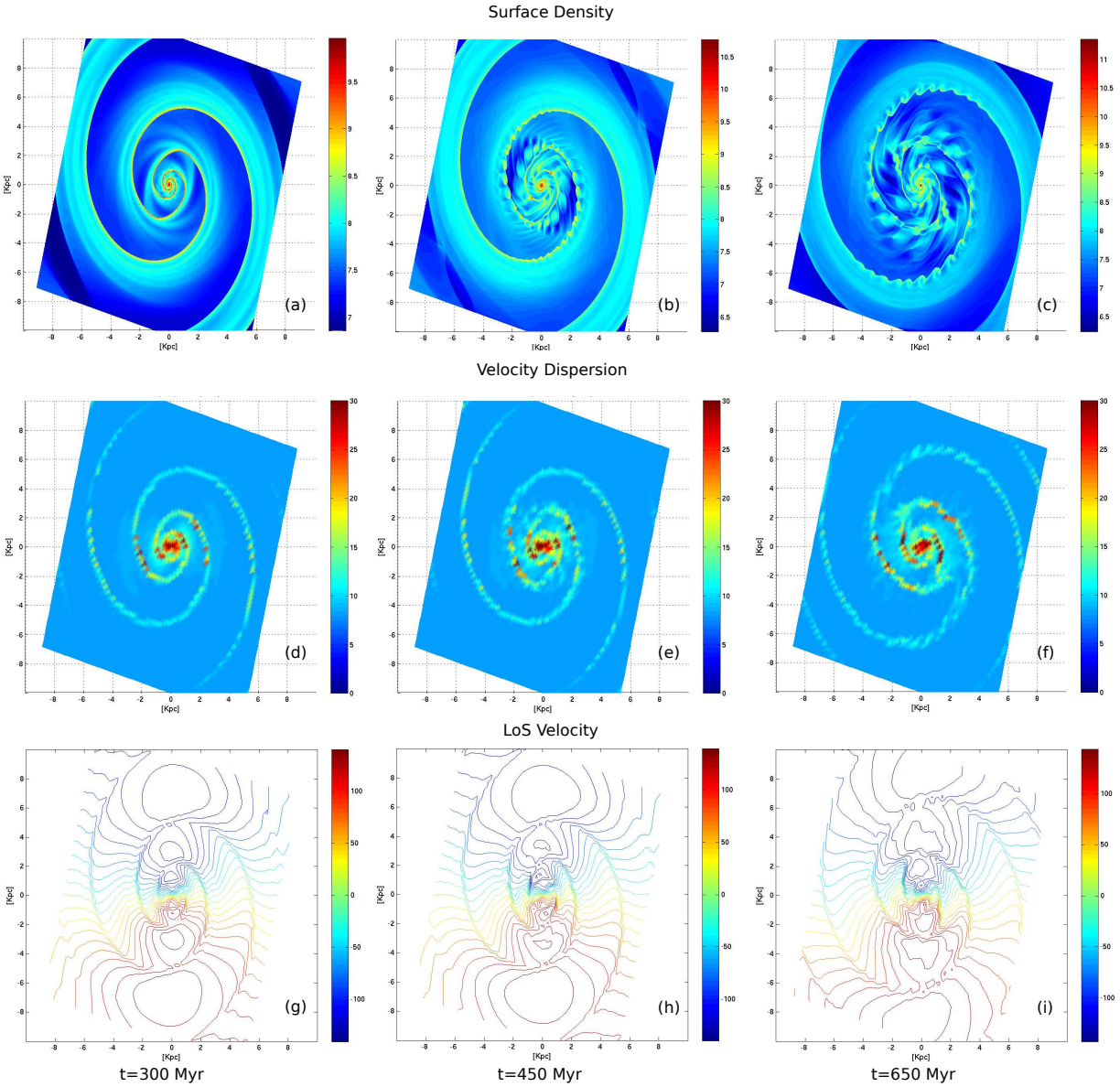

Figure 4.2: The evolution of the surface density (first row), line-of-sight velocity dispersion (second row) and the iso-velocity contours (third row) at $t = 300$ (first column), 450 (second column), 650 Myr (third column). Note that since the self-gravity of gas is not included in our calculation, the unit of mass is scale free. A thermal broadening of 8 km s^{-1} is adopted when producing the map of velocity dispersion.

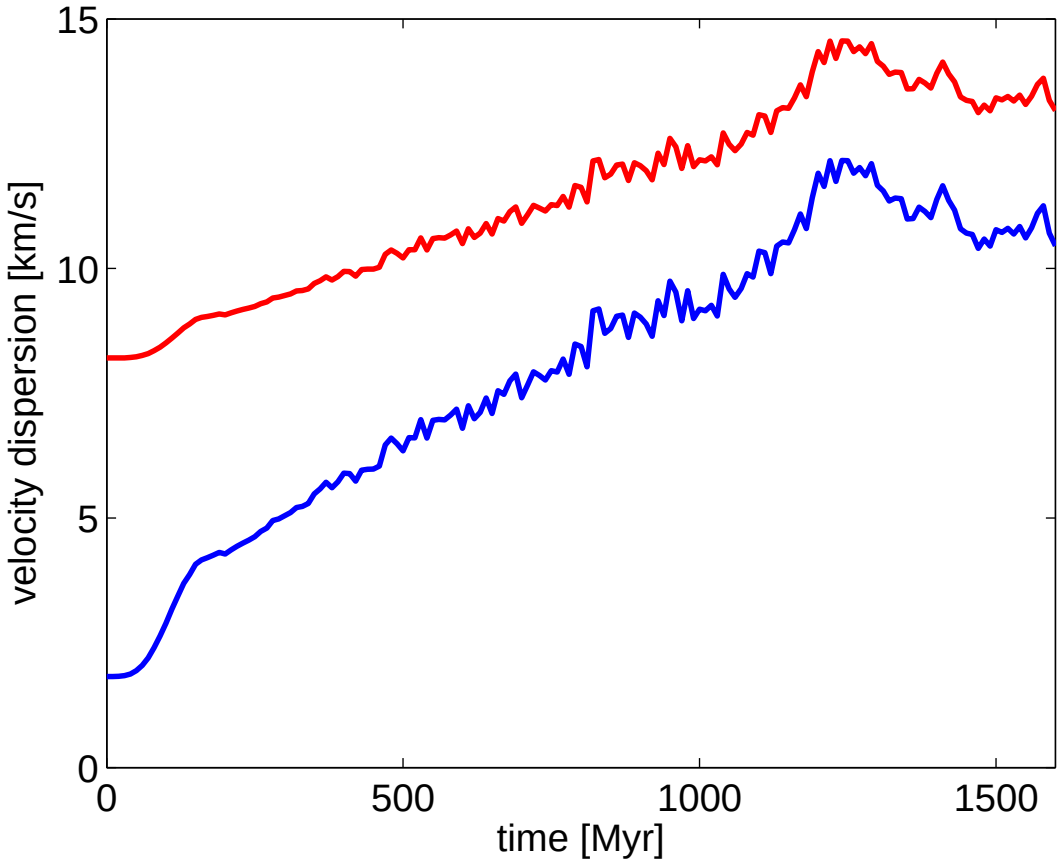

Figure 4.3: The mass-weighted line-of-sight velocity dispersion. The blue curve is the kinematic velocity dispersion, $\sigma_{\rm kin}$, calculated for the disk within $R = 9$ kpc. The red one is the result total velocity dispersion $\sigma^2_{\rm tot} = \sigma^2_{\rm th} + \sigma^2_{\rm kin}$, involving a thermal broadening of $\sigma_{\rm th} = 8$ km s^{-1}. The kinematic velocity dispersion saturates at 11 km s^{-1} and 13 km s^{-1} for the total velocity dispersion after an evolution of 1.3 Gyr. These results fit observations very well.

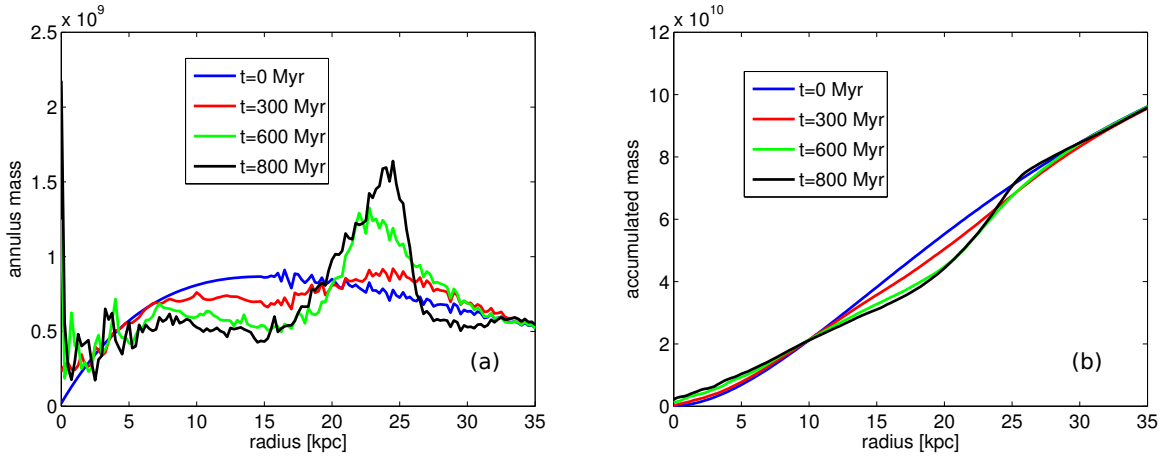

Figure 4.4: Evolution of (a) radial mass and (b) accumulated mass distribution. From (b), the evolution of mass seems to be separated by the corotation (10.7 kpc), where the spiral shock vanishes. The total mass enclosed inside the corotation drops very little. While the gas between corotation and OLR (18.5 kpc) is efficiently transferred to the outer disk, gas inside corotation is transported towards galactic center.

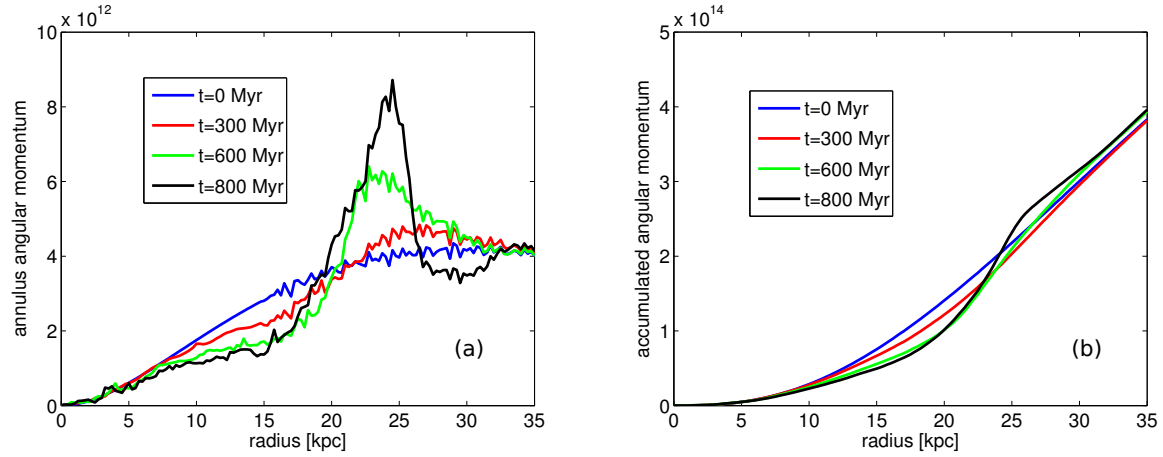

Figure 4.5: Evolution of (a) annular angular momentum and (b) accumulated angular momentum. From (b), overall the total angular momentum enclosed inside the OLR (18.5 kpc) is efficiently tranferred to the outer disk. Gas inside the corotation is experiencing the losing and the redistribution of angular momentum. Comparing (a) with Fig. 4.4a, while the mass distribution coincides with the angular momentum distribution in the outer disk, it is not the case for the inner disk.

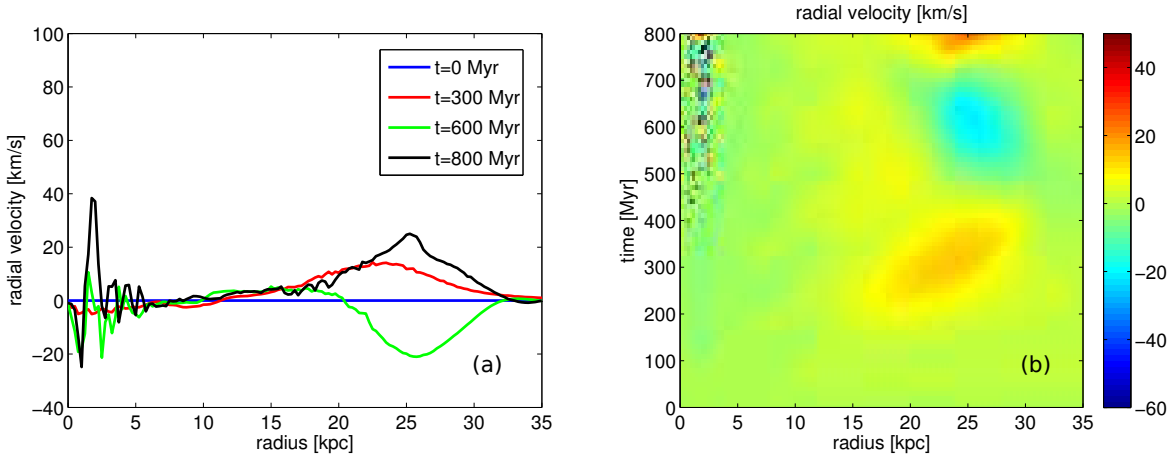

Figure 4.6: Evolution of (a) mass-weighted radial velocity and (b) mass-weighted radial velocity in time-radius plane. (a) is simply the horizontal cuts from (b) at $t = 0, 300, 600, 800$ Myr. Before the wiggle instability sets in, gas is moving inward inside the corotation with a speed $\sim -3 \pm 2$ km s^{-1}, moving outward subsonically for the region between corotation and OLR. The radial motion beyond OLR is supersonic (± 20 km s^{-1}) and oscillates with time. This is best visualized in (b). Once the wiggle instability sets in at $t = 330$ Myr, the gas motion is severely disturbed in the inner disk. The sign of radial motion in the inner disk changes with radius.

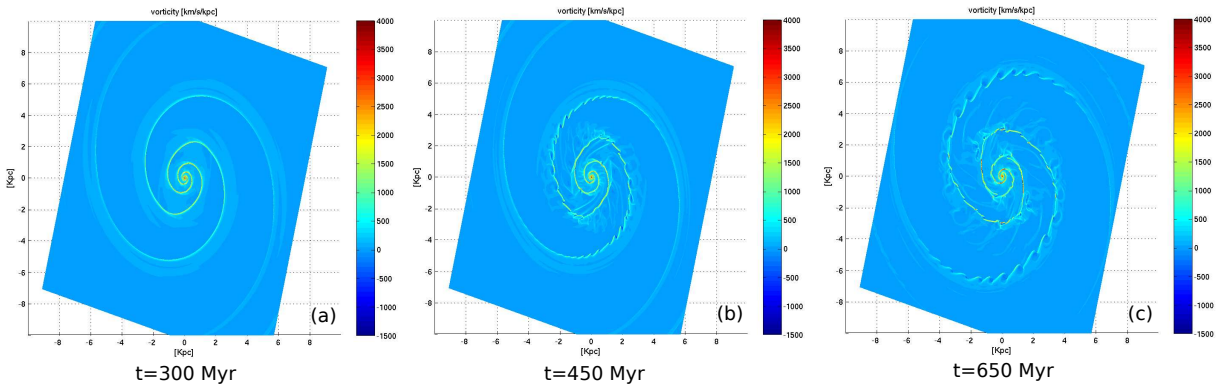

Figure 4.7: Evolution of vorticity in units of km s^{-1} kpc^{-1} at $t = 300, 450, 650$ Myr. In (b) and (c), after the wiggle instability sets in, the spiral shocks are distorted. The retrograde vortices (the deep blue) are created along the shocks and dissipate in the interarm region due to the post-shock expansion. Vorticity is not a conserved quantity in a compressible flow.

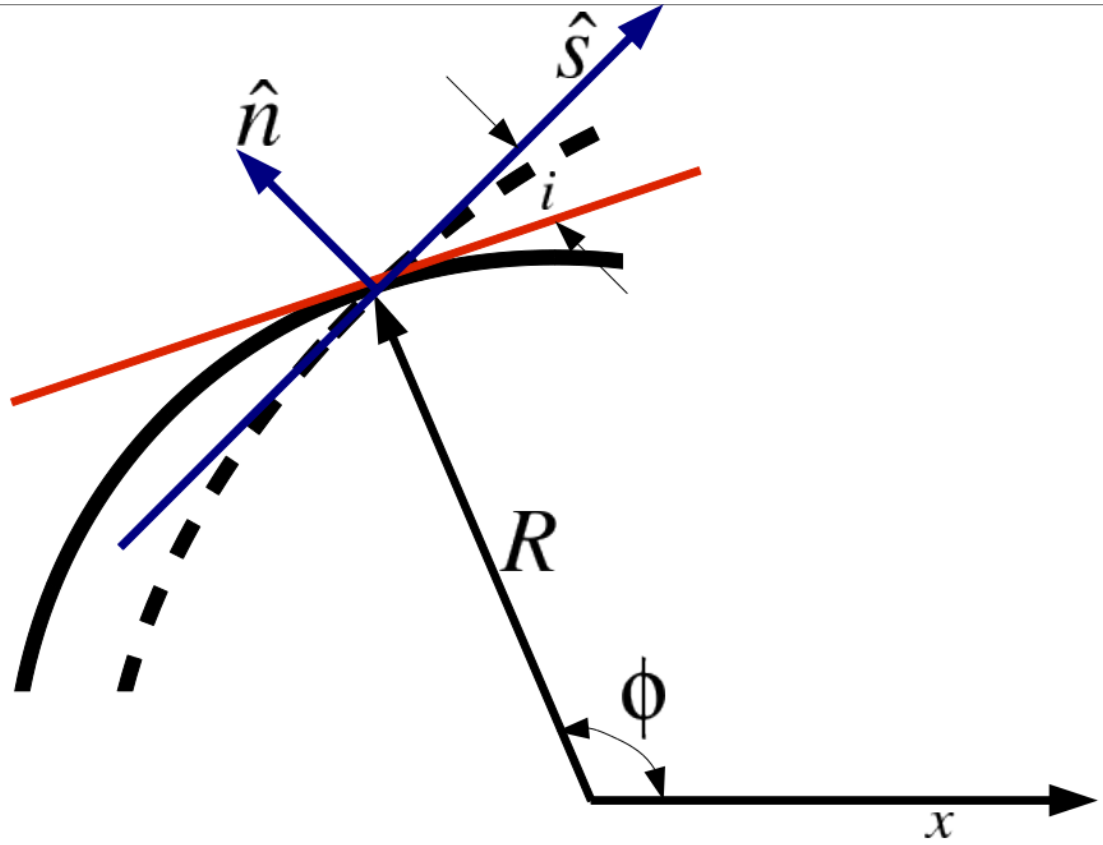

Figure 4.8: The black arc is part of a circle and the dashed curve represents a section of a logrithmic spiral. The angle difference between $\hat{s}$ and the azimuthal tangent $-\hat{\phi}$ defines the pitch angle i. $\hat{n}$ represents the unit normal vector to the shock front pointing the downstream side. $\hat{s}$ is defined by $\hat{z} = \hat{s} \times \hat{n}$.

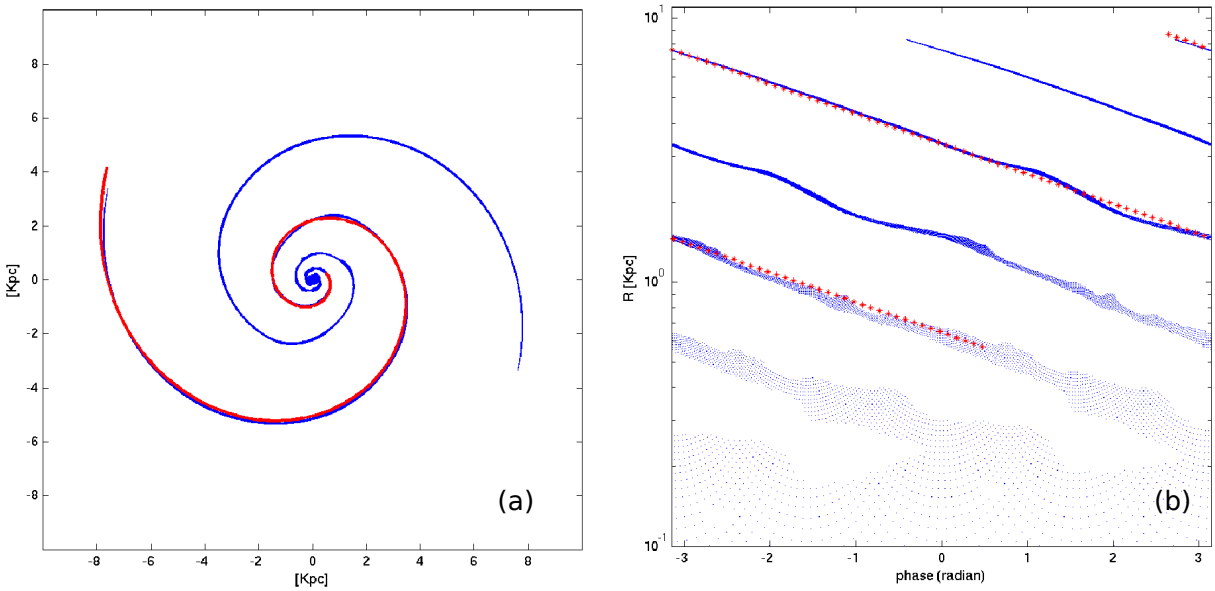

Figure 4.9: $t = 300$ Myrs. In (a) we trace the location of the spiral shocks. The red line is a logarithmic spiral with a pitch angle of $i = 15°$, a bit smaller than the imposed spirals, which have $i = 17°$. The pitch angle of a logarithmic spiral is better seen in a phase-log(R) diagram as shown in (b). Again, the red stars corresponds the fitting curve in (a). The oscillation of the pitch angle in the inner spiral is due to the interaction between the ILR resonance and the external forcing as discussed in Sec. 4.6 . This has a dynamical impact on the streaming motion.

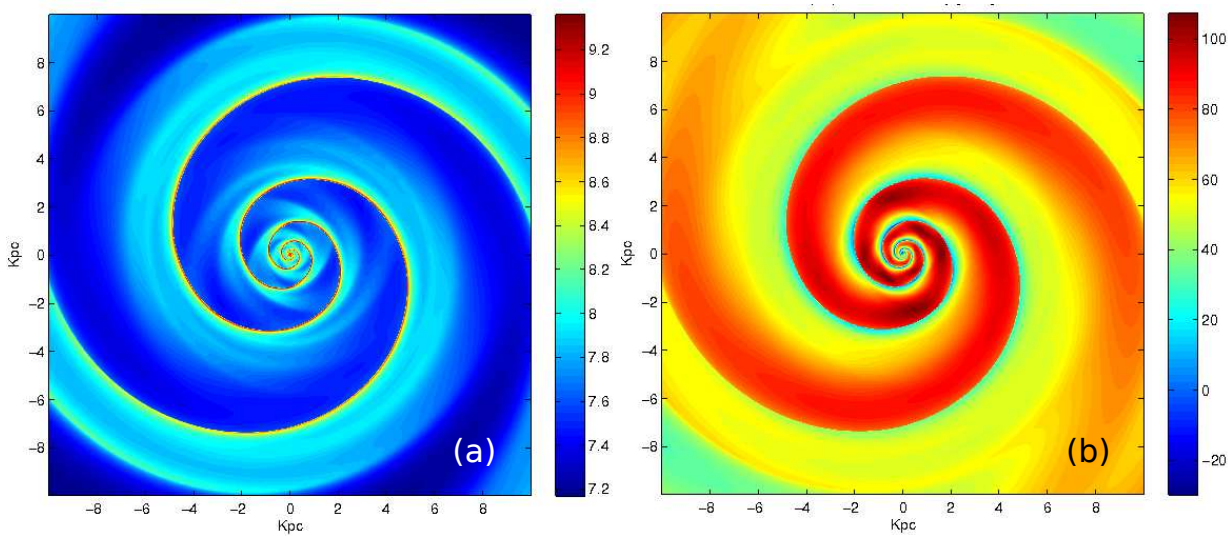

Figure 4.10: $t = 200$ Myr. (a) The surface density shows a pair of well-defined spiral shock and substructures like spurs or branches. (b) With a well-defined pitch angle (see Fig. 4.9), we obtain the perpendicular component of the velocity field with respect to the shock. We find that the velocity field is modulated by the 2:1 resonance, which is located at 2.6 kpc. The ILR might be responsible for the oscillation as seen in the pitch angle.

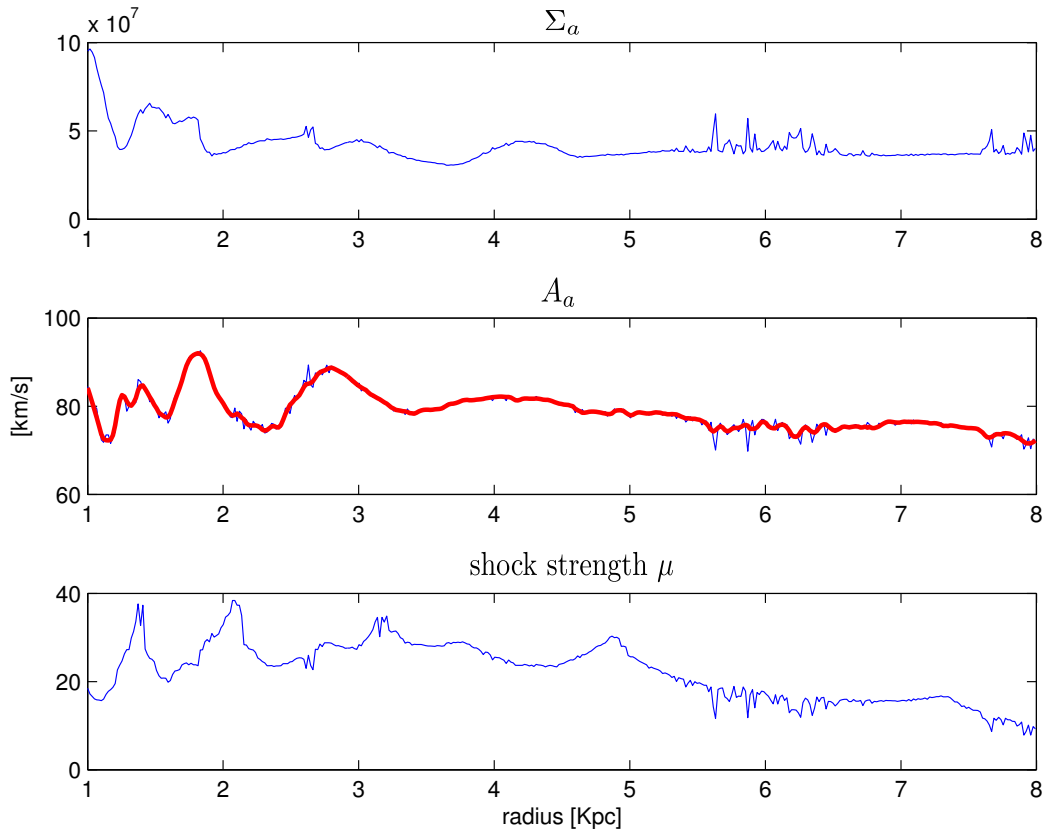

Figure 4.11: t = 200 Myrs. We choose this time because the shock is well-developed. During developing period of time, the pattern speed and the pitch angle of the shock are well-defined. To evaluate the generation of vorticity via Eq. (4.14), one needs three pieces of information as shown from the top to the bottom panels. *Top*: Surface density right ahead the shock, Σ_a. *Middle*: Velocity component normal to the shock front ahead the shock, A_a. *Bottom*: The strength of the shock, μ. Because performing numerical derivative directly from the raw data can be noisy due to the finite numerical resolution in space, we smooth the A_a before the evalutation of Eq. (4.14). The result is shown as the red curve in the middle panel.

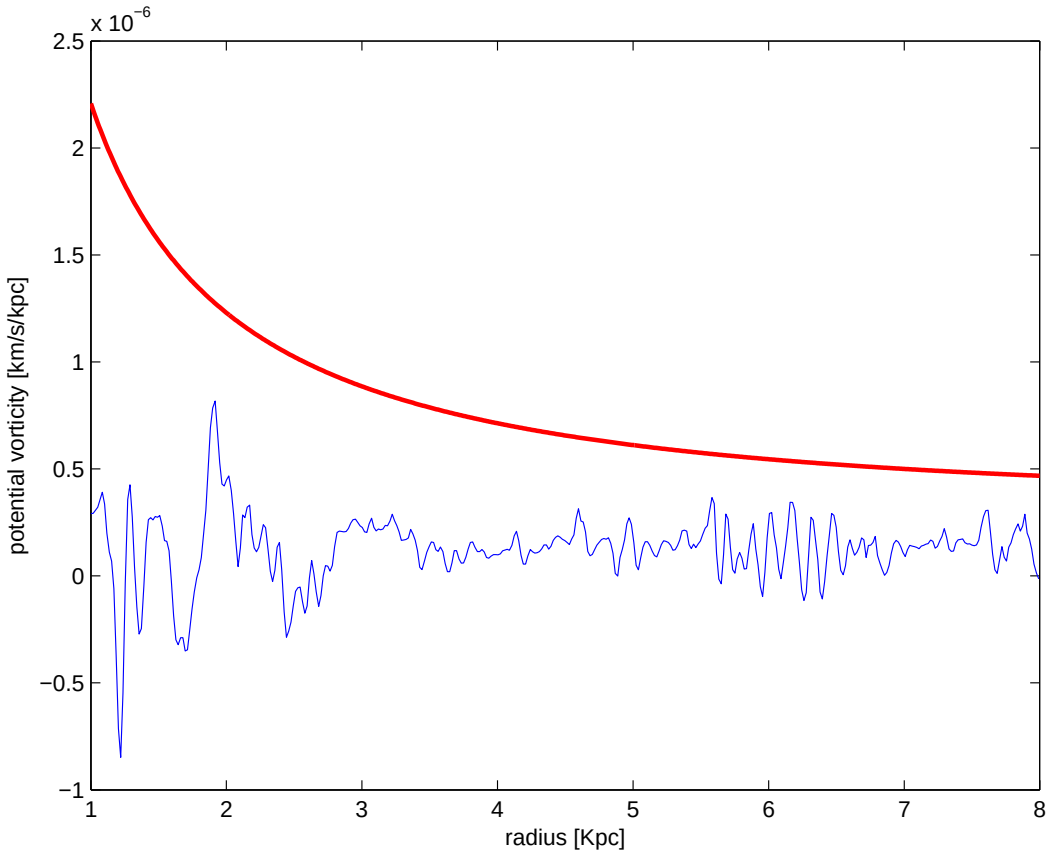

Figure 4.12: The red curve represents the intrinsic vortensity evaluated from the initial condition. The blue curve is the generated vortensity evaluated via Eq. (4.14) at $t = 200$ Myr. It shows the shock is generating both positive and negative vortensity comparable to the intrinsic one in the inner disk ($R < 3$ kpc), while on average positive for the outer disk ($3 < R < 8$ kpc). It seems that there is a characteristic size, ~ 100 pc, on which the vortensity is created.

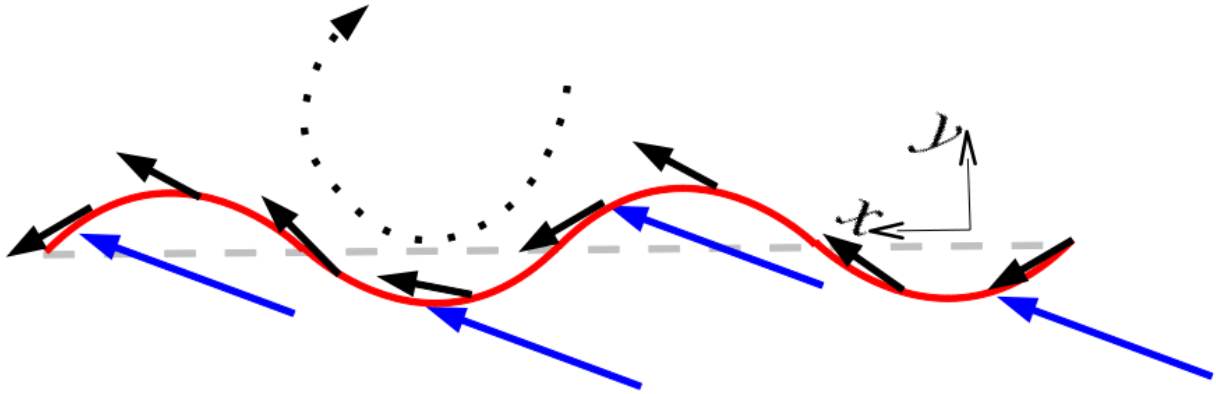

Figure 4.13: This cartoon illustrates the impact of the tiny ripple in pitch angle on the post-shock flow. The original straight shock (grey-dashed line) is somehow displaced into a sinusoidal one (red-curve), representing a small ripple in pitch angle. The blue arrows represents the directions of the incident supersonic flow and the black arrows the directions of the post-shock flow.

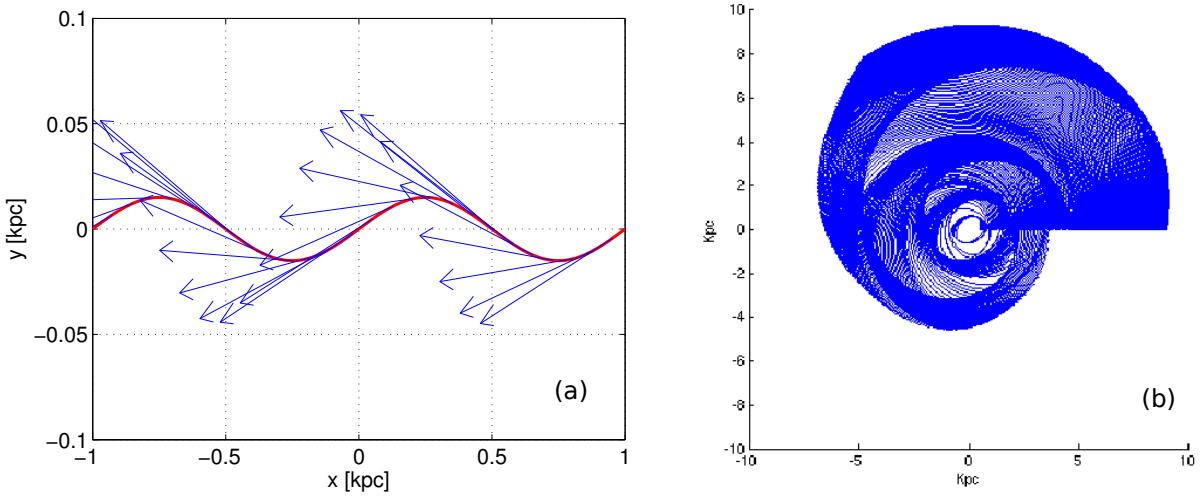

Figure 4.14: $t = 200$ Myr.(a) The arrows represents the directions of post-shock flow obtained by Eqs. (A.30) and (A.31). The red curve is a distorted shock. The incident flow (not shown in the figure) comes in with a incident angle of 73°,i.e., pitch angle 17°, with respect to the undistorted straight shock (see also Fig. 4.13). (b) Separation and aggregation of streamlines. Streamlines are set off along the x-axis with a uniform spacing 50 pc. The leading structures seen in Fig. 4.10a is simply the crowding of streamlines and has nothing to do with 4:1 resonance.

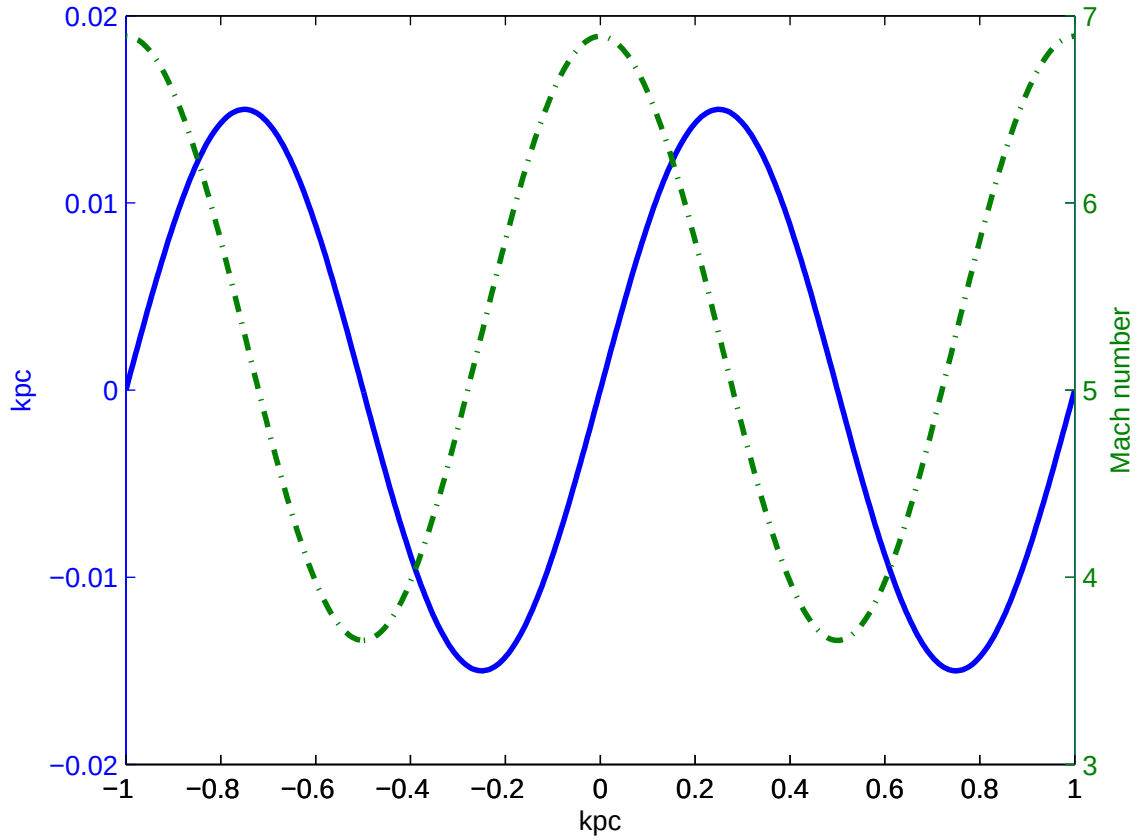

Figure 4.15: The blue curve is the distorted shock. The configuration of the incident flow is the same as shown in Fig. 4.13. The dash-dotted line represents the Mach number, M_a, of the perpendicular component of incident velocity. As expected, the resulting shock is stronger on the head-on side and weaker on the leeside. Note that the scales of x-axis and the left y-axis are not equal. The amplitude of the ripple is only 1.5% of the wavelength ($\lambda = 1$ kpc). However, the resulting variation in shock strength is large.

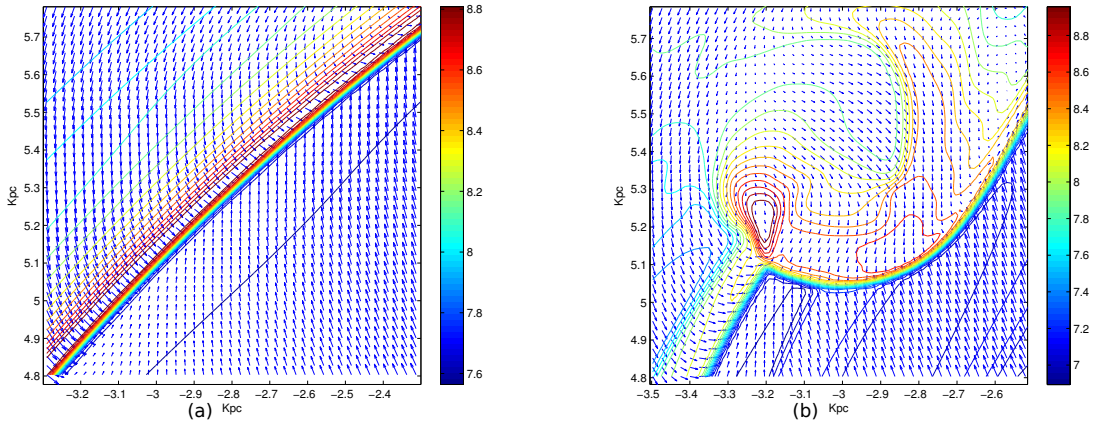

Figure 4.16: The surface density (contours) is overlapped with the velocity residual (arrows) after a subtraction of the mean velocity of the images. A square of 1×1 kpc^2 is excerpted around the shock area at (a) $t = 200$ and (b) $t = 650$ Myr in order to closely observe the flow pattern.

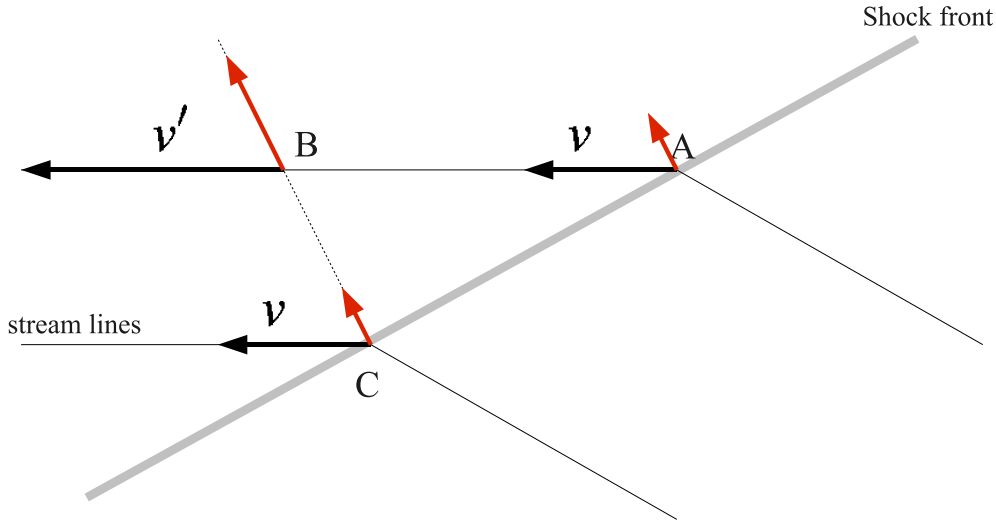

Figure 4.17: The picture of an oblique shock (Wada & Koda 2004). We apply this picture to the outer disk where the flow ahead the shock is nearly uniform. As described by WK04, gas is accelerated from A toward B (black arrows). Therefore, a velocity gradient exist between B and C (black arrows) leading to the KH instability. However, if we sit in a inertial frame within which the tangential velocity vanishes, the flow pattern in the post-shock looks like the red arrows. By doing Galilean transformation, velocity gradient does not exist and the KH instability would not happen. We can also apply the same picture to the inner disk where the rotation curve rises alomst linearly as the case discussed in the Appendix of WK04. In this case, the incident velocity at point A will be a bit higher than that at point C and therefore increases the velocity gradient between points B and C. If the KH instability do happen, intuitively the vortices created in this flow pattern should be prograde in the same sense of global rotation rather than the retrograde vortices seen in Fig. 4.16b.

pagenumberingarabic setcounterpage1

Chapter 5

Summary and Outlook

5.1 Summary

In this thesis, we investigate many aspects of the evolution of disk galaxies theoretically, numerically and observationally. In Chapter 2, we find that initializing a three-dimensional gas disk which is in hydrodynamic equilibrium is not a trivial task. No trivial and simple method is found in the literature. Therefore, we put forward a new systematic way of setting up galactic gas disks based on the assumption of detailed hydrodynamic equilibrium. To do this, we need to specify the density distribution and the velocity field which supports the disk. In Section 2.2, We show that the required circular velocity has no dependence on the height above or below the midplane so long as the gas pressure is a function of density only. The assumption of disks being very thin enables us to decouple the vertical structure from the radial direction. Based on that, the equation of hydrostatic equilibrium together with the reduced Poisson equation leads to two sets of second-order non-linear differential equation, which are easily integrated to set-up a stable disk. We call one approach 'density method' and the other one 'potential method'.

In Section 2.3, the methods developed in Section 2.2 are implemented with the adaptive mesh refinement (AMR) magnetohydrodynamics code RAMSES (Teyssier 2002). A three-dimensional, gravitationally stable disk is evolved for five orbital time without a clear sign of change in its configuration. This result confirms the effectiveness of our methods.

Gas disks in detailed balance are especially suitable for investigating the onset of the gravitational instability. In Section 2.4, we revisit the question of global, axisymmetric instability using fully three-dimensional disk simulations. The impact of disk thickness on the disk instability and the formation of spontaneously induced spirals is studied systematically with or without the presence of the stellar potential. In our models, the numerical results show that the threshold value for disk instability is shifted from unity to 0.69 for self-gravitating thick disks and to 0.75 for combined stellar and gas thick disks.

In Section 2.5, the methods are applied to investigate the phenomenon called 'swing amplification' (Toomre 1981) which occurs in a marginally stable disk. With a proper disk initialization, for the first time, we are able to numerically address and confirm this phenomenon for a three-dimensional disk. The simulation results show that self-induced spirals occur in the correct regions and with the right numbers as predicted by the analytic theory. This result suggest that our disks have correct dynamical properties.

In Chapter 3, we find the longstanding missing link that associates the evolution of disk galaxies with the replenishment of gas in order to sustain star formation over cosmological times. The radial gas inflow is confirmed in the extreme outer disk of M83 (NGC5236). In Section 3.2, we combine the information extracted from the synthesis interferometric maps from THINGS with that from the single dish data reconstructed from the contour maps obtained by the 100-m radio telescope of the Max-Planck-Institut für Radioastronomie at Effelsberg in late 70s to search for the sign of mass inflow.

In Section 3.3, a series of tilted rings are deployed over the disk for Fourier analysis. As is done in Schoenmakers et al. (1997), for each ring, a tilted-ring model followed by a Fourier decomposition is applied. However, we take one step further to their work, the Fourier decomposition introduced in this paper directly decomposes the line-of-sight velocity into the rotational and the radial Fourier components, giving more details about the gaseous kinematics.

In Section 3.4, the method developed in Section 3.3 is applied to study the kinematics of M83. Due to the low inclination of M83, a parameter survey is conducted to bracket the kinematic uncertainties. With the results shown in Section 3.4, for the first time, we are able to build the sequence of gas accretion from the extreme outer disk to the inner star forming disk. Intergalactic gas accretes in the form of filaments with an infall rate of 2.5 ± 1.5 $M_\odot$ yr^{-1}. The accreting gas hits the Keplarian orbit at $R = 10'$ and forms the bright HI ring seen in the THINGS map due to the conservation of angular momentum. The phase shift appearing in the position angle is interpreted as the presence of radial inflow, contributing a mass inflow of 2.3 $M_\odot$ yr^{-1} at the radius $R = 7.5'$, which fits excellently to the observed star formation rate 2.5 $M_\odot$ yr^{-1} (Walter et al. 2008). Note that the Holmberg radius is at $R = 7.3'$. Thus, we believe that in M83 the gas is channelled inwards to feed the star forming disk by means of streaming motion, i.e., the cold mode accretion.

In Chapter 4, we perform a two-dimensional, unmagnetized, non-selfgravitating simulation to investigate the impacts of density waves of stellar origin on gas motions. Although many similar works has been carried out in the literature, many aspects studied in this Chapter are less recognized and quantified. In Section 4.2, we describe the model parameters used for the simulation. We stress that the strength of spiral arm used in this Chapter is based on observation results (Rix & Zaritsky 1995).

In Section 4.3, we examine the dispersion velocity for the galaxy sample studied by Tamburro et al. (2009). We find that the correlation between between disk inclination and velocity dispersion is stronger than that between star formation rate and velocity dispersion. Galaxies having larger disk inclination tend to have larger velocity dispersion. To understand that, we deliberately downgrade the numerical spatial resolution to match the obeservation one. Based on the definition of velocity dispersion defined in Walter et al. (2008), we calculate the velocity dispersion along the line-of-sight. We find that nonsteady spiral shocks can efficiently tap turbulent energy from regular rotation motions. The level of velocity dispersion driven by nonsteady shocks fits excellently to the observations.

In Section 4.4, we find that the presence of spiral density waves can change the distribution of gas surface density and angular momentum on a relatively short time scale compared to the secular evolution time scale of stellar disk. Angular momentum is transported from inner disk toward the outer disk. The nonsteady shocks severely stir the radial motions of gas, resulting in the sign change in the radial velocity. This result has been observed by Shetty et al. (2007).

In Section 4.5, we quantify the vortensity generation along spiral shocks. We analytically demonstrate that vortensity is not a conserved quantity in a compressible flow with shocks. We quantitatively show that the vortensity created by galactic shocks is not negligible compared to the intrinsic disk vortensity. An important result is that both negative and positive vortices can be created in galactic shocks.

In Section 4.6, We consider the small ripple in pitch angle as a result of interaction between the inner Lindblad resonance and the forced shock waves. We show that this small ripple has huge impacts on the shock strengh and the post-shock flow, which is then responsible for the formation of substructures and the shock deformation. In this thesis, we view the spurs as a result of the conspiracy between the shock deformation, the generation of negative votensity and the Coriolis force. We also argue that the Kelvin-Helmholtz instability described in Wada & Koda (2004) is not likely responsible for the formation of spurs.

5.2 Outlook

In this thesis, many aspects of gas evolution in disk galaxies are investigated. These studies open many lines of future works.

As already mentioned in Chapter 2, the method we develop for initializing an three-dimensional equilibrium gas disk fits to the framework developed for collisionless particles (Shu 1969; Kuijken & Dubinski 1995). A natural and ongoing next step is to develop a systematic way for initializing a composite disk in which live stellar disk, live stellar bulge and live dark matter

halo can evolve with gas disk. The lack of a proper way for initializing a composite disk in the literature hinders our way to address many questions. One of the most basic ones is Rafikov's criterion for composite disk stability. Although this criterion has been used to account for the star formation rate observed in nearby galaxies (Leroy et al. 2008; Hunter et al. 1998; Blitz & Rosolowsky 2004; Yang et al. 2007), how do different components react to this instability is unclear. We expect the stellar disk and the gas disk will response in a very different way. This question cannot be addressed without a composite disk which is initialized in detailed balance.

Following the study of Rafikovs criterion, the interaction between the gas disk and the live stellar disk now can be systematically and self-consistently investigated. Although the spiral or bar formation in a live stellar disk has been studied for many years, the interaction between live stellar spiral/bar and gas disk has not been closely inspected. We can try to address the following questions. How does the presence of gas disk affect the evolution of stellar structures? How does the angular momentum exchange between gas and stars? What is the lifetime of stellar spirals or bars with or without the presence of gas disk? How does the gas react to the live stellar structures?

The alignment of magnetic field ranging from several kpc down to the dense core of molecular clouds shows that the magnetic field may have a profound impact on galaxy evolution (Beck et al. 1996; H.B. Li , private communication). We can study how the combined disk organizes and amplifies the magnetic fields, i.e, galactic dynamo. It will be also interesting to look into how the magnetic fields affect star formation in a self-consistent composite disk.

Another ongoing work is associated with the large-scale structure and star formation observed in the extreme outer disk of M83 (Thilker 2005; Bigiel et al. 2010a). The filaments there might be a result of galactic dynamo or simply of the gravitational wake left behind the path of a dwarf satellite, which is interacting with M83. Because the density enhancement is small 5% of the averaged surface density, violent interaction cannot be the cause. Even puzzling, how can the massive stars form in such a barren area? We address these questions by applying the equilibrium disk developed in Chapter 2.

Gas accretion observed for M83 should not be an unique event in the Universe. The method described in Chapter 3 build a stereotype for searching gas accretion and should be applied to a larger sample of disk galaxies. The upcoming single dish observations for nearby galaxies, which are already included in THINGS sample, will provide an excellent opportunity to extend our understanding of intergalactic gas accretion.

A nature line following the work of Chapter 4 is to extend the simulation to three-dimension. However, to have a spatial resolution comparable to the two-dimensional work, this extension seems to be too computationally expensive to be practical. We have developed a technique called 'zoom-in' box allowing us to trace the impacts of spiral density wave on gas motions in

a three-dimensional simulation. Contrast to the shearing box simulating a small section of the whole disk, we take the advantage of AMR putting more resolution on the regions of our interest. The region can be a comoving box or a comoving long arc. The advantage of this technique is that we can feed the zoom-in box with a realistic boundary condition, which is naturally obtained from the global evolution of disks.

Appendix A

Appendix

A.1 The Derivation of Rotation Velocity

Equation (2.11) can be re-written as

$$\begin{aligned} p(R,z) &= \rho(R,z)\,\frac{p(R)}{\rho(R)}\bigg|_{z=0} - \rho(R,z)\int_0^z \frac{p}{\rho^2}\frac{\partial\rho}{\partial z}\mathrm{d}z \\ &- \rho(R,z)[\Phi(R,z) - \Phi(R,z=0)], \end{aligned} \tag{A.1}$$

where we have replaced $\Phi_z = \Phi(R,z) - \Phi(R,z=0)$. Inserting Eq. (A.1) in Eq. (2.1) involves a partial derivative to the integral, let us prepare it first:

$$\begin{aligned} &\frac{\partial}{\partial R}\left(\int_0^z \frac{p}{\rho^2}\frac{\partial\rho}{\partial z}\mathrm{d}z\right) = \int_0^z \frac{\partial}{\partial R}\left(\frac{p}{\rho^2}\frac{\partial\rho}{\partial z}\right)\mathrm{d}z \\ &= \int_0^z \left\{\frac{\partial^2}{\partial R\partial z}\left(\frac{p}{\rho^2}\rho\right) - \frac{\partial}{\partial R}\left[\rho\frac{\partial}{\partial z}\left(\frac{p}{\rho^2}\right)\right]\right\}\mathrm{d}z \\ &= \int_0^z \left\{\frac{\partial}{\partial z}\left[\frac{p}{\rho^2}\frac{\partial\rho}{\partial R} + \rho\frac{\partial}{\partial R}\left(\frac{p}{\rho^2}\right)\right] - \frac{\partial}{\partial R}\left[\rho\frac{\partial}{\partial z}\left(\frac{p}{\rho^2}\right)\right]\right\}\mathrm{d}z \\ &= \frac{p(R,z)}{\rho(R,z)}\frac{\partial\ln\rho(R,z)}{\partial R} - \frac{p(R,z=0)}{\rho(R,z=0)}\frac{\partial\ln\rho(R,z=0)}{\partial R} \\ &\quad + \int_0^z \left\{\left(\frac{\partial\rho}{\partial z}\right)\frac{\partial}{\partial R}\left(\frac{p}{\rho^2}\right) - \left(\frac{\partial\rho}{\partial R}\right)\frac{\partial}{\partial z}\left(\frac{p}{\rho^2}\right)\right\}\mathrm{d}z \end{aligned} \tag{A.2}$$

With Eq. (A.2), the first term of Eq. (2.1) then becomes:

$$
\begin{aligned}
\frac{1}{\rho(R,z)}\frac{\partial p(R,z)}{\partial R} &= \frac{\partial}{\partial R}\left(\frac{p(R,z=0)}{\rho(R,z=0)}\right) \\
&- \left[\frac{\partial\Phi(R,z)}{\partial R} - \frac{\partial\Phi(R,z=0)}{\partial R}\right] \\
&+ \frac{p(R,z=0)}{\rho(R,z=0)}\frac{\partial \ln\rho(R,z=0)}{\partial R} \\
&- \int_0^z \left\{\left(\frac{\partial\rho}{\partial z}\right)\frac{\partial}{\partial R}\left(\frac{p}{\rho^2}\right) - \left(\frac{\partial\rho}{\partial R}\right)\frac{\partial}{\partial z}\left(\frac{p}{\rho^2}\right)\right\}\mathrm{d}z \\
&+ \frac{\partial \ln\rho(R,z)}{\partial R}\left\{\frac{p(R,z=0)}{\rho(R,z=0)} - \frac{p(R,z)}{\rho(R,z)}\right. \\
&- \left.\Phi(R,z) + \Phi(R,z=0) - \int_0^z \frac{p}{\rho^2}\frac{\partial\rho}{\partial z}\mathrm{d}z\right\}
\end{aligned}
\tag{A.3}
$$

Equation (2.11) says that the term in the big brace should vanish. And therefore, Eq. (2.1) reduces to

$$
\begin{aligned}
\frac{1}{\rho}\frac{\partial p}{\partial R} + \frac{\partial\Phi}{\partial R} &= \frac{\partial}{\partial R}\left[\frac{p(R,z=0)}{\rho(R,z=0)}\right] \\
&+ \frac{\partial\Phi(R,z=0)}{\partial R} + \frac{p(R,z=0)}{\rho(R,z=0)}\frac{\partial \ln\rho(R,z=0)}{\partial R} \\
&- \int_0^z \left\{\left(\frac{\partial\rho}{\partial z}\right)\frac{\partial}{\partial R}\left(\frac{p}{\rho^2}\right) - \left(\frac{\partial\rho}{\partial R}\right)\frac{\partial}{\partial z}\left(\frac{p}{\rho^2}\right)\right\}\mathrm{d}z
\end{aligned}
\tag{A.4}
$$

For the barotropic gas, i.e., $p(\rho)$, the integrand of the integral vanishes:

$$
\begin{aligned}
&\left(\frac{\partial\rho}{\partial z}\right)\frac{\partial}{\partial R}\left(\frac{p}{\rho^2}\right) - \left(\frac{\partial\rho}{\partial R}\right)\frac{\partial}{\partial z}\left(\frac{p}{\rho^2}\right) \\
&= \left(\frac{\partial\rho}{\partial z}\right)\frac{\partial}{\partial\rho}\left(\frac{p}{\rho^2}\right)\frac{\partial\rho}{\partial R} - \left(\frac{\partial\rho}{\partial R}\right)\frac{\partial}{\partial\rho}\left(\frac{p}{\rho^2}\right)\frac{\partial\rho}{\partial z} = 0
\end{aligned}
\tag{A.5}
$$

For the cases of initially constant temperature, the specific internal energy, e, is a constant and therefore the pressure is a function of density only, the integrand vanishes.

A.2 The effect of the disk thickness on the midplane potential

For an axisymmetrically and infinitesimally thin disk, the potential can be evaluated by the following relation (Binney & Tremaine 2008):

$$
\Phi(R,z) = \int_0^\infty \mathrm{d}k S_0(k) J_0(kR) e^{-k|z|}, \tag{A.6}
$$

where J_0 is the Bessel function of the first kind of order zero and S_0 is the Hankel transform of $-2\pi G\Sigma_0$ defined by:

$$S_0(k) = -2\pi G \int_0^\infty \mathrm{d}R' R' J_0(kR')\Sigma_0(R') \tag{A.7}$$

With Eq. (A.6) and Eq. (A.7), we can superimpose the potential contributed by each gas layer. For the sake of simplicity, we assume that the volume density has the double exponential profile:

$$\rho_0(R,z) = \Sigma_0 e^{-R/R_\mathrm{d}} \frac{e^{-z/h_z}}{2h_z}, \tag{A.8}$$

with h_z being the scale-height of the gaseous disk, Eq. (A.7) then becomes (Gradshteyn & Ryzhik 1965, hereafter GR65, 6.623-2):

$$\begin{aligned} S_0(k,z) &= \frac{-2\pi G\Sigma_0 e^{-z/h_z}}{2h_z}\Delta z \int_0^\infty \mathrm{d}R' R' J_0(kR') e^{-R'/R_d} \\ &= \frac{-2\pi G\Sigma_0 e^{-z/h_z}}{2h_z}\Delta z \frac{\xi}{(\xi^2+k^2)^{3/2}}, \end{aligned} \tag{A.9}$$

with $\xi = 1/R_\mathrm{d}$. Δz represents the infinitesimal thickness introduced to keep the dimension correct. The potential which takes into account the thickness of the disk then reads:

$$\begin{aligned} \Phi(R,z) &= -2\pi G\Sigma_0 \int_0^\infty \mathrm{d}k \frac{\xi}{(\xi^2+k^2)^{3/2}} J_0(kR) \\ &\times \int_{-\infty}^\infty e^{-k|z-h|} \frac{e^{-h/h_z}}{2h_z} \mathrm{d}h. \end{aligned} \tag{A.10}$$

Evaluating the potential at the midplane, $z = 0$, yields:

$$\Phi(R, z=0) = -2\pi G\Sigma_0 \int_0^\infty \mathrm{d}k \frac{\xi}{(\xi^2+k^2)^{3/2}} J_0(kR) \frac{1}{1+kh_z}. \tag{A.11}$$

Given the finite scale-height, the integral can be evaluated numerically and compared with the result of the infinitesimally thin disk.

A.3 The Derivation of the reduction factor

To derive the reduction factor F defined by Eq. (2.35) we need to evaluate the integral of the form:

$$\begin{aligned} &\int_{-\infty}^\infty e^{-k|h|} \mathrm{sech}^2(ah)\mathrm{d}h = 2\int_0^\infty e^{-kh}\mathrm{sech}^2(ah)\mathrm{d}h \\ &= \frac{2}{a}\left\{1 - \frac{k}{2a}\left[H\left(\frac{k}{4a}\right) - H\left(\frac{k}{4a} - \frac{1}{2}\right)\right]\right\}. \end{aligned} \tag{A.12}$$

The last line can be reached by looking up the formulae 3.541, 8.370, 8.361-7 listed in the integral table (GR65) and the definition Eq. (2.36). In the last line, we have employed the recursive relation (8.365-1 GR65):

$$H(\alpha) = H(\alpha - 1) + \frac{1}{\alpha}. \tag{A.13}$$

The asymptotic behavior of the harmonic number reads (8.367-2, 8.367-13 GR65):

$$H(\alpha) = \ln \alpha + \gamma + \frac{1}{2}\alpha^{-1} - \frac{1}{12}\alpha^{-2} + \frac{1}{120}\alpha^{-4} + O(\alpha^{-6}), \tag{A.14}$$

with $\gamma = 0.5772156649$ (8.367-1 GR65) being the Euler-Mascheroni constant. Note that Eq. (A.14) is only reliable when $\alpha \geq 1$. We employ the recursive relation (C2) to evaluate $H(\alpha)$ for $-1 < \alpha < 1$.

A.4 The vertical force ratio

The vertical force ratio measures the impact of the halo force on the vertical structure. The simplified Poisson equation for isothermally self-gravitating gas disk reads:

$$\frac{\partial^2 \Phi_g}{\partial z^2} = 4\pi G \rho_0(R) \mathrm{sech}^2\left(\frac{z}{h_z}\right), \tag{A.15}$$

where h_z being a measure of the scale-height. Parameter h_z can be related to the volume density in the midplane, $\rho_0(R)$ by:

$$h_z = \sqrt{\frac{c_s^2}{2\pi G \rho_0}}. \tag{A.16}$$

The corresponding vertical force for the gas then becomes:

$$F_{z,\mathrm{gas}} = -\frac{\partial \Phi}{\partial z} = -4\pi G h_z \rho_0(R) \tanh(z/h_z). \tag{A.17}$$

For a NFW halo, the vertical force can be written down directly:

$$F_{z,\mathrm{DM}} = \frac{GM_{200}}{f(c)} \left(\frac{c}{r_{200}}\right)^2 \frac{x/(1+x) - \ln(1+x)}{x^2} \frac{z}{\sqrt{R^2+z^2}}, \tag{A.18}$$

with $x = c\sqrt{R^2+z^2}/r_{200}$. Figure A.1 then shows the force ratio $F_{z,\mathrm{DM}}/F_{z,\mathrm{gas}}$ as a function of vertical height $|z|$ at different radii. Comparing to the rotation curve shown in the left panel of Fig. 2.1, although the dynamics is still dictated by the potential of the dark halo, the vertical structure of the gaseous disk is mainly determined by the self-gravity of the gas component. However, it raises another issue, the presence of the stellar disk will dominate both the dynamics and the vertical structure of the gas and will affect the stability of the gas component via changing the thickness of the gaseous disk and the rotation curve.

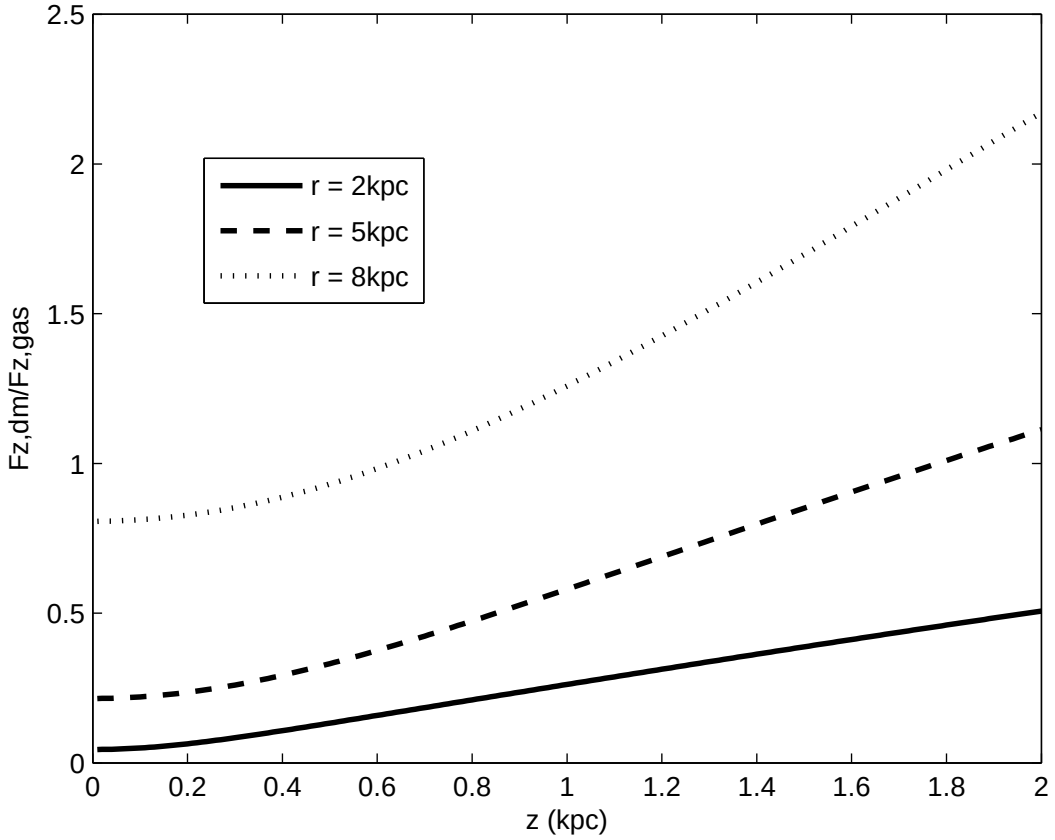

Figure A.1: The force ratio $F_{z,DM}/F_{z,gas}$ at R=2, 5 and 8 kpc. It shows that the vertical structure of the inner disk is determined mostly by the self-gravity of gas.

A.5 Validity check of the reduced Poisson Equation for the gas disk

Throughout this paper we have assumed that the radial potential gradients of the disk are negligible compared to the vertical gradients, such that the Poisson equation reduces to Eq. (2.14). We now test this assumption by computing the ratio

$$\epsilon \equiv |\frac{1}{R}\frac{\partial}{\partial R}(R\frac{\partial \Phi_g}{\partial R})/\frac{\partial^2 \Phi_g}{\partial z^2}|, \tag{A.19}$$

with Φ_g the gravitational potential of the gas disk. For a realistic, analytical disk model, our assumption will be valid as long as $\epsilon \ll 1$.

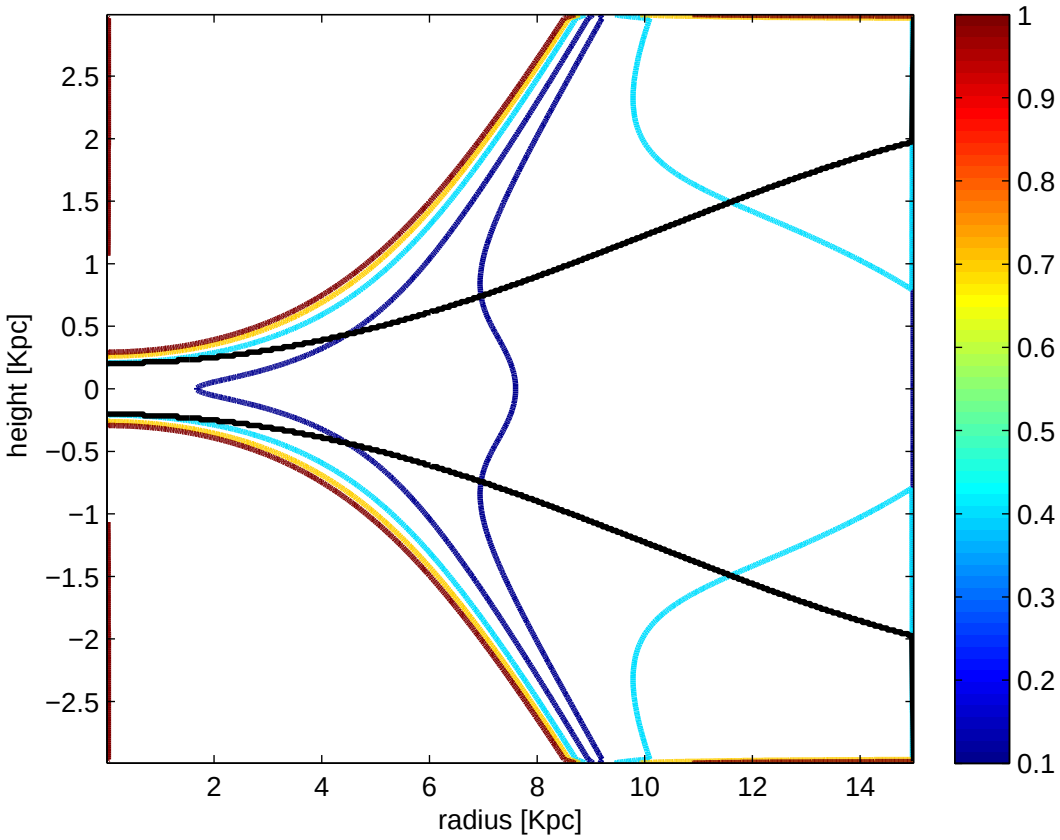

Figure A.2: Contour map of ϵ. The black lines represent the scale-height of the gas disk.

Consider the Miyamoto & Nagai (1975) potential:

$$\Phi_{\rm g}(R,z) = -\frac{GM_{\rm g}}{\sqrt{R^2 + (a + \sqrt{z^2 + b^2(R)})^2}}\,. \tag{A.20}$$

Here a is a constant that controls the scale-length of the disk and $b(R)$, which we take to be a function of radius, modulates the scale-height of the disk. In the limit $b \to 0$ this model reduces to the infinitesimal Kuzmin disk (e.g., Binney & Tremaine 2008). In an attempt to model the gas disk in our simulation 'Gas0', we adopt $a = 3.5$ kpc. In order to mimic the flaring of the Gas0 disk (see Fig. 2.2b), we consider

$$b(R) = -1.58 \times 10^{-5} R^4 + 1.21 \times 10^{-2} R^2 + 0.20. \tag{A.21}$$

Using the Poisson equation to solve (numerically) for the corresponding density distribution yields the radial-dependent scale-height shown as the solid black lines in Fig. A.2, and which is comparable to that of the Gas0 disk. The contours in Fig. A.2 are defined by constant values of

ϵ. These show that our assumption that $\epsilon \ll 1$ is well-justified in the inner part of the disk, out to ~ 3 scale-lengths, which encloses most of the disk mass. The assumption that $\epsilon \ll 1$ deteriorates at larger radii and at higher altitude away from the midplane. This might be in part responsible for the very slight outward drifting of the disk seen in Fig. 2.2b. In cases that include a stellar potential and/or cooler gas, the gas disk is even thinner than the case considered here, resulting in values for ϵ that are even smaller. Based on these results, and based on the absence of significant disk thickening in our simulations, we are confident that Eq. (2.14) is sufficiently accurate for all realistic gas disks.

A.6 transformation matrix

Supposing that we have a galaxy with position angle, PA, and inclination angle i. Velocity field is transformed from face-on view, $(v_x, v_y, 0)$, to tilted coordinates, (v'_x, v'_y, v'_z) by:

$$\begin{bmatrix} v'_x \\ v'_y \\ v'_z \end{bmatrix} = \begin{bmatrix} \cos(PA)\cos(i) & -\sin(PA)\cos(i) & \sin(i) \\ \sin(PA) & \cos(PA) & 0 \\ -\sin(i)\cos(PA) & \sin(i)\sin(PA) & \cos(i) \end{bmatrix} \begin{bmatrix} v_x \\ v_y \\ 0 \end{bmatrix}. \tag{A.22}$$

Then, the velocity in line-of-sight, $v_{\rm LoS}$, reads:

$$v_{\rm LoS} = -v_x \sin(i)\cos(PA) + v_y \sin(i)\sin(PA). \tag{A.23}$$

A.7 The post-shock streaming flow

In this appendix, we follow the picture described in the Appendix A of Vishniac (1994) to derive the post-shock streaming motion. A local coordinates (x, y) is set-up along the straight shock as shown in Fig. 4.13 . The displacement of the shock is described by a sinusoidal wave:

$$y = A\sin(\frac{2\pi}{\lambda}x) = A\sin(kx), \tag{A.24}$$

with λ being the wavelength of the wave and $k \equiv 2\pi/\lambda$ the wave number and A the amplitude of displacement. The unit normal vector, $\hat{n}_\perp$, to the shock front then reads:

$$\hat{n}_\perp = \frac{\hat{y} - Ak\cos(kx)\hat{x}}{\sqrt{1 + A^2k^2\cos^2(kx)}}, \tag{A.25}$$

with $\hat{x}$ and $\hat{y}$ being the unit vectors in x and y, respectively. The corresponding unit tangent is defined:

$$\hat{n}_{\parallel} = \frac{Ak\cos(kx)\hat{y} + \hat{x}}{\sqrt{1 + A^2k^2\cos^2(kx)}}. \tag{A.26}$$

Assuming that the incident flow is $\vec{v} = v_x\hat{x} + v_y\hat{y}$, the pre-shock velocity is decomposed into $\vec{v}_{\perp} \equiv \vec{v}\cdot\hat{n}_{\perp}$ and $\vec{v}_{\parallel} \equiv \vec{v}\cdot\hat{n}_{\parallel}$:

$$v_{\perp} = \frac{-Akv_x\cos(kx) + v_y}{\sqrt{1 + A^2k^2\cos^2(kx)}}, \tag{A.27}$$

$$v_{\parallel} = \frac{Akv_y\cos(kx) + v_x}{\sqrt{1 + A^2k^2\cos^2(kx)}}. \tag{A.28}$$

Applying the Rankine-Hugoniot jump conditions for isothermal gas, we have:

$$v_{\perp}v'_{\perp} = c_s^2, \tag{A.29}$$

$$v_{\parallel} = v'_{\parallel}, \tag{A.30}$$

where $v'_{\perp}$ and $v'_{\parallel}$ defines the post-shock velocity $\vec{v}' = v'_{\perp}\hat{n}_{\perp} + v'_{\parallel}\hat{n}_{\parallel}$. The expression of $v'_{\perp}$ reads:

$$v'_{\perp} = \frac{c_s^2\sqrt{1 + A^2k^2\cos^2(kx)}}{-Akv_x\cos(kx) + v_y}. \tag{A.31}$$

The singularity shown in Eq. (A.31) marks the point where $v_{\perp} = 0$ and therefore limits the amplitude of the displacement, A, and the possible values for wave number k.

Bibliography

Aalto, S., Hüttemeister, S., Scoville, N. Z., & Thaddeus, P. 1999, ApJ, 522, 165

Agertz, O., Lake, G., Teyssier, R., et al. 2009, MNRAS, 392, 294

Athanassoula, E. 1992, MNRAS, 259, 345

Athanassoula, E. 2005, MNRAS, 358, 1477

Athanassoula, E., Bosma, A., & Papaioannou, S. 1987, A&A, 179, 23

Balbus, S. A. 1988, ApJ, 324, 60

Balbus, S. A. & Hawley, J. F. 1991, ApJ, 376, 214

Balbus, S. A. & Hawley, J. F. 1998, Reviews of Modern Physics, 70, 1

Beck, R., Brandenburg, A., Moss, D., Shukurov, A., & Sokoloff, D. 1996, ARA&A, 34, 155

Begeman, K. G. 1989, A&A, 223, 47

Bell, E. F., Zheng, X. Z., Papovich, C., et al. 2007, ApJ, 663, 834

Bertin, G. 1983, A&A, 127, 145

Bigiel, F., Leroy, A., Seibert, M., et al. 2010a, ArXiv e-prints

Bigiel, F., Leroy, A., Walter, F., et al. 2010b, ArXiv e-prints

Bigiel, F., Leroy, A., Walter, F., et al. 2008, AJ, 136, 2846

Binney, J. 1974, MNRAS, 168, 73

Binney, J. & Tremaine, S. 2008, Galactic Dynamics: Second Edition, ed. Binney, J. & Tremaine, S. (Princeton University Press)

Blitz, L. & Rosolowsky, E. 2004, ApJ, 612, L29

Bonnell, I. A., Dobbs, C. L., Robitaille, T. P., & Pringle, J. E. 2006, MNRAS, 365, 37

Bournaud, F., Combes, F., Jog, C. J., & Puerari, I. 2005, A&A, 438, 507

Burstein, D. 1979, ApJ, 234, 829

Capuzzo-Dolcetta, R., Leccese, L., Merritt, D., & Vicari, A. 2007, ApJ, 666, 165

Carollo, C. M., Ferguson, H. C., & Wyse, R. F. G. 1999, The formation of galactic bulges. Proceedings., ed. Carollo, C. M., Ferguson, H. C., & Wyse, R. F. G.

Casertano, S. 1983, MNRAS, 203, 735

Chakrabarti, S., Laughlin, G., & Shu, F. H. 2003, ApJ, 596, 220

Chernin, A. D. 1993, A&A, 267, 315

Chernin, A. D. & Efremov, Y. N. 1995, MNRAS, 275, 209

Comte, G. 1981, A&AS, 44, 441

Daddi, E., Bournaud, F., Walter, F., et al. 2010a, ApJ, 713, 686

Daddi, E., Elbaz, D., Walter, F., et al. 2010b, ApJ, 714, L118

de Blok, W. J. G., Walter, F., Brinks, E., et al. 2008, AJ, 136, 2648

de Grijs, R. & Peletier, R. F. 1997, A&A, 320, L21

de Vaucouleurs, G. 1958, ApJ, 127, 487

de Vaucouleurs, G. 1959, Handbuch der Physik, 53, 275

de Vaucouleurs, G. 1963, ApJS, 8, 31

de Vaucouleurs, G., de Vaucouleurs, A., Corwin, Jr., H. G., et al. 1991, Third Reference Catalogue of Bright Galaxies. Volume I: Explanations and references. Volume II: Data for galaxies between 0^h and 12^h. Volume III: Data for galaxies between 12^h and 24^h., ed. de Vaucouleurs, G., de Vaucouleurs, A., Corwin, H. G., Jr., Buta, R. J., Paturel, G., & Fouqué, P.

Dekel, A. & Birnboim, Y. 2006, MNRAS, 368, 2

Dickey, J. M. & Lockman, F. J. 1990, ARA&A, 28, 215

Diehl, R., Halloin, H., Kretschmer, K., et al. 2006, Nature, 439, 45

Dobbs, C. L. & Bonnell, I. A. 2006, MNRAS, 367, 873

Doroshkevich, A. G. 1973, Soviet Ast., 16, 986

Dressler, A. 1980, ApJ, 236, 351

Dubinski, J. 1994, ApJ, 431, 617

Elmegreen, B. G. & Scalo, J. 2004, ARA&A, 42, 211

Elmegreen, B. G., Seiden, P. E., & Elmegreen, D. M. 1989, ApJ, 343, 602

Escala, A. & Larson, R. B. 2008, ApJ, 685, L31

Evans, N. W. & Read, J. C. A. 1998, MNRAS, 300, 106

Evrard, A. E., Silk, J., & Szalay, A. S. 1990, ApJ, 365, 13

Ferrarese, L. & Merritt, D. 2000, ApJ, 539, L9

Fleck, Jr., R. C. 1991, Ap&SS, 182, 81

Foyle, K., Rix, H., & Zibetti, S. 2010, MNRAS, 407, 163

Fraternali, F. 2009, in IAU Symposium, Vol. 254, IAU Symposium, ed. J. Andersen, J. Bland-Hawthorn, & B. Nordström, 255–262

Fraternali, F. 2010, in American Institute of Physics Conference Series, Vol. 1240, American Institute of Physics Conference Series, ed. V. P. Debattista & C. C. Popescu, 135–145

Fraternali, F. & Binney, J. J. 2008, MNRAS, 386, 935

Fraternali, F., Oosterloo, T. A., Sancisi, R., & Swaters, R. 2005, in Astronomical Society of the Pacific Conference Series, Vol. 331, Extra-Planar Gas, ed. R. Braun, 239–+

Fraternali, F., van Moorsel, G., Sancisi, R., & Oosterloo, T. 2002, AJ, 123, 3124

Frenk, C. S., White, S. D. M., Davis, M., & Efstathiou, G. 1988, ApJ, 327, 507

Fuchs, B. 2001, A&A, 368, 107

Fuchs, B. 2008, Astronomische Nachrichten, 329, 916

Fuchs, B. & von Linden, S. 1998, MNRAS, 294, 513

Fujimoto, M. 1966, IAU Symp

Gammie, C. F. 2001, ApJ, 553, 174

Garcia-Burillo, S., Guelin, M., & Cernicharo, J. 1993, A&A, 274, 123

Gebhardt, K., Bender, R., Bower, G., et al. 2000, ApJ, 539, L13

Gentile, G., Burkert, A., Salucci, P., Klein, U., & Walter, F. 2005, ApJ, 634, L145

Genzel, R., Tacconi, L. J., Gracia-Carpio, J., et al. 2010, ArXiv e-prints

Gnedin, O. Y., Goodman, J., & Frei, Z. 1995, AJ, 110, 1105

Goldreich, P. & Lynden-Bell, D. 1965, MNRAS, 130, 125

Goldreich, P. & Tremaine, S. 1979, ApJ, 233, 857

Goldreich, P. & Tremaine, S. 1980, ApJ, 241, 425

Goldreich, P. & Tremaine, S. D. 1978a, Icarus, 34, 240

Goldreich, P. & Tremaine, S. D. 1978b, Icarus, 34, 227

Goto, T., Yamauchi, C., Fujita, Y., et al. 2003, MNRAS, 346, 601

Gradshteyn, I. S. & Ryzhik, I. M. 1965, Table of integrals, series and products, ed. Gradshteyn, I. S. & Ryzhik, I. M.

Graham, A. W., Erwin, P., Caon, N., & Trujillo, I. 2001, ApJ, 563, L11

Griv, E., Liverts, E., & Mond, M. 2008, ApJ, 672, L127

Gunn, J. E. & Gott, III, J. R. 1972, ApJ, 176, 1

Haan, S., Schinnerer, E., Emsellem, E., et al. 2009, ApJ, 692, 1623

Häring, N. & Rix, H. 2004, ApJ, 604, L89

Hayashi, E., Navarro, J. F., Power, C., et al. 2004, MNRAS, 355, 794

Hayashi, E., Navarro, J. F., & Springel, V. 2007, MNRAS, 377, 50

Hayes, W. D. 1957, Journal of Fluid Mechanics, 2, 595

Hippelein, H., Maier, C., Meisenheimer, K., et al. 2003, A&A, 402, 65

Hohl, F. 1971, ApJ, 168, 343

Hopkins, A. M. & Beacom, J. F. 2006, ApJ, 651, 142

Hubble, E. 1929, Proceedings of the National Academy of Science, 15, 168

Hubble, E. P. 1926, ApJ, 64, 321

Hubble, E. P. 1936, Realm of the Nebulae, ed. Hubble, E. P.

Huchtmeier, W. K. & Bohnenstengel, H. 1981, A&A, 100, 72

Hunt, L. K., Combes, F., García-Burillo, S., et al. 2008, A&A, 482, 133

Hunter, D. A., Elmegreen, B. G., & Baker, A. L. 1998, ApJ, 493, 595

Huntley, J. M., Sanders, R. H., & Roberts, Jr., W. W. 1978, ApJ, 221, 521

Jackson, P. D. & Kellman, S. A. 1974, ApJ, 190, 53

Jiang, I. & Binney, J. 1999, MNRAS, 303, L7

Jog, C. J. & Solomon, P. M. 1984, ApJ, 276, 127

Jogee, S., Scoville, N., & Kenney, J. D. P. 2005, ApJ, 630, 837

Julian, W. H. & Toomre, A. 1966, ApJ, 146, 810

Kalnajs, A. J. 1978, in IAU Symposium, Vol. 77, Structure and Properties of Nearby Galaxies, ed. E. M. Berkhuijsen & R. Wielebinski, 113–125

Karachentsev, I. D., Karachentseva, V. E., Huchtmeier, W. K., & Makarov, D. I. 2004, AJ, 127, 2031

Kauffmann, G., White, S. D. M., & Guiderdoni, B. 1993, MNRAS, 264, 201

Kennicutt, Jr., R. C. 1989, ApJ, 344, 685

Kennicutt, Jr., R. C. 1998, ApJ, 498, 541

Kennicutt, Jr., R. C., Armus, L., Bendo, G., et al. 2003, PASP, 115, 928

Kent, S. M., Dame, T. M., & Fazio, G. 1991, ApJ, 378, 131

Kereš, D., Katz, N., Fardal, M., Davé, R., & Weinberg, D. H. 2009, MNRAS, 395, 160

Kereš, D., Katz, N., Weinberg, D. H., & Davé, R. 2005, MNRAS, 363, 2

Kevlahan, N. 1997, Journal of Fluid Mechanics, 341, 371

Kim, C., Kim, W., & Ostriker, E. C. 2006, ApJ, 649, L13

Kim, W. & Ostriker, E. C. 2002a, ApJ, 570, 132

Kim, W. & Ostriker, E. C. 2002b, ApJ, 570, 132

Kim, W. & Ostriker, E. C. 2006, ApJ, 646, 213

Kim, W. & Ostriker, E. C. 2007, ApJ, 660, 1232

Kim, W., Ostriker, E. C., & Stone, J. M. 2002, ApJ, 581, 1080

Klessen, R. S. & Hennebelle, P. 2010, A&A, 520, A17+

Koribalski, B. S. e. 2004, AJ, 128, 16

Kormendy, J. 1993, in IAU Symposium, Vol. 153, Galactic Bulges, ed. H. Dejonghe & H. J. Habing, 209–+

Kornreich, D. A., Lovelace, R. V. E., & Haynes, M. P. 2002, ApJ, 580, 705

Kornreich, P. & Scalo, J. 2000, ApJ, 531, 366

Kuijken, K. & Dubinski, J. 1995, MNRAS, 277, 1341

Kuzio de Naray, R., McGaugh, S. S., & de Blok, W. J. G. 2008, ApJ, 676, 920

Lacey, C. & Cole, S. 1993, MNRAS, 262, 627

Larson, R. B., Tinsley, B. M., & Caldwell, C. N. 1980, ApJ, 237, 692

Lemaître, G. 1927, Annales de la Societe Scietifique de Bruxelles, 47, 49

Leroy, A. K., Walter, F., Brinks, E., et al. 2008, AJ, 136, 2782

Levy, V. V., Mustsevoy, V. V., & Sergienko, V. A. 1996, Astronomical and Astrophysical Transactions, 11, 1

Li, Y., Mac Low, M., & Klessen, R. S. 2005a, ApJ, 620, L19

Li, Y., Mac Low, M., & Klessen, R. S. 2005b, ApJ, 626, 823

Li, Y., Mac Low, M., & Klessen, R. S. 2006, ApJ, 639, 879

Lighthill, M. J. 1957, Journal of Fluid Mechanics, 2, 1

Lin, C. C. & Shu, F. H. 1964, ApJ, 140, 646

Lisker, T. & Fuchs, B. 2009, A&A, 501, 429

Lockman, F. J. 1984, ApJ, 283, 90

Lynden-Bell, D. & Kalnajs, A. J. 1972, MNRAS, 157, 1

Mac Low, M. & Klessen, R. S. 2004, Reviews of Modern Physics, 76, 125

Marconi, A. & Hunt, L. K. 2003, ApJ, 589, L21

Martin, C. L. & Kennicutt, Jr., R. C. 2001, ApJ, 555, 301

Matthews, L. D., van Driel, W., & Gallagher, III, J. S. 1998, AJ, 116, 1169

Maulbetsch, C., Avila-Reese, V., Colín, P., et al. 2007, ApJ, 654, 53

Miller, E. D., Bregman, J. N., & Wakker, B. P. 2009, ApJ, 692, 470

Miyamoto, M. & Nagai, R. 1975, PASJ, 27, 533

Moore, B., Katz, N., Lake, G., Dressler, A., & Oemler, A. 1996, Nature, 379, 613

Narayan, C. A. & Jog, C. J. 2002, A&A, 394, 89

Navarro, J. F., Frenk, C. S., & White, S. D. M. 1997, ApJ, 490, 493

Noguchi, M. 1999, ApJ, 514, 77

Ostriker, E. C. & Binney, J. J. 1989, MNRAS, 237, 785

Pasha, I. I. 1985, Soviet Astronomy Letters, 11, 1

Pasha, I. I. & Smirnov, M. A. 1982, Ap&SS, 86, 215

Perlmutter, S., Aldering, G., Goldhaber, G., et al. 1999, ApJ, 517, 565

Pflamm-Altenburg, J. & Kroupa, P. 2009, ApJ, 706, 516

Pichon, C. & Cannon, R. C. 1997, MNRAS, 291, 616

Piontek, R. A. & Ostriker, E. C. 2004, ApJ, 601, 905

Piontek, R. A. & Ostriker, E. C. 2005, ApJ, 629, 849

Piontek, R. A. & Ostriker, E. C. 2007, ApJ, 663, 183

Postman, M. & Geller, M. J. 1984, ApJ, 281, 95

Rafikov, R. R. 2001, MNRAS, 323, 445

Rand, R. J. & Kulkarni, S. R. 1990, ApJ, 349, L43

Riess, A. G., Filippenko, A. V., Challis, P., et al. 1998, AJ, 116, 1009

Rix, H. & Zaritsky, D. 1995, ApJ, 447, 82

Roberts, W. W. 1969, ApJ, 158, 123

Roberts, Jr., W. W. & Stewart, G. R. 1987, ApJ, 314, 10

Rogstad, D. H., Lockhart, I. A., & Wright, M. C. H. 1974, ApJ, 193, 309

Rots, A. H. 1975, A&A, 45, 43

Ruhland, C., Bell, E. F., Häußler, B., et al. 2009, ApJ, 695, 1058

Sancisi, R., Fraternali, F., Oosterloo, T., & van der Hulst, T. 2008, A&A Rev., 15, 189

Sanders, D. B., Solomon, P. M., & Scoville, N. Z. 1984, ApJ, 276, 182

Sanders, R. H. & Tubbs, A. D. 1980, ApJ, 235, 803

Sawamura, M. 1988, PASJ, 40, 279

Schempp, W. V. 1982, ApJ, 258, 96

Schmidt, M. 1959, ApJ, 129, 243

Schoenmakers, R. H. M., Franx, M., & de Zeeuw, P. T. 1997, MNRAS, 292, 349

Schoenmakers, R. H. M. & Swaters, R. A. 1999, in Astronomical Society of the Pacific Conference Series, Vol. 182, Galaxy Dynamics - A Rutgers Symposium, ed. D. R. Merritt, M. Valluri, & J. A. Sellwood, 277–+

Scoville, N. Z., Polletta, M., Ewald, S., et al. 2001, AJ, 122, 3017

Sellwood, J. A. 1981, A&A, 99, 362

Sellwood, J. A. 1985, MNRAS, 217, 127

Sellwood, J. A. & Carlberg, R. G. 1984, ApJ, 282, 61

Sellwood, J. A. & Moore, E. M. 1999, ApJ, 510, 125

Shetty, R. & Ostriker, E. C. 2006, ApJ, 647, 997

Shetty, R., Vogel, S. N., Ostriker, E. C., & Teuben, P. J. 2007, ApJ, 665, 1138

Shu, F. H. 1969, ApJ, 158, 505

Shu, F. H., Dones, L., Lissauer, J. J., Yuan, C., & Cuzzi, J. N. 1985a, ApJ, 299, 542

Shu, F. H., Milione, V., Gebel, W., et al. 1972, ApJ, 173, 557

Shu, F. H., Milione, V., & Roberts, Jr., W. W. 1973, ApJ, 183, 819

Shu, F. H., Yuan, C., & Lissauer, J. J. 1985b, ApJ, 291, 356

Spergel, D. N., Bean, R., Doré, O., et al. 2007, ApJS, 170, 377

Spitzer, Jr., L. 1942, ApJ, 95, 329

Springel, V., Di Matteo, T., & Hernquist, L. 2005, MNRAS, 361, 776

Steinmetz, M. & Muller, E. 1995, MNRAS, 276, 549

Steinmetz, M. & Navarro, J. F. 2002, New Astron., 7, 155

Tamburro, D., Rix, H., Leroy, A. K., et al. 2009, AJ, 137, 4424

Tamburro, D., Rix, H., Walter, F., et al. 2008, AJ, 136, 2872

Tasker, E. J. & Bryan, G. L. 2006, ApJ, 641, 878

Teyssier, R. 2002, A&A, 385, 337

Thilker, D. A. e. 2005, ApJ, 619, L79

Toomre, A. 1964, ApJ, 139, 1217

Toomre, A. 1981, in Structure and Evolution of Normal Galaxies, ed. S. M. Fall & D. Lynden-Bell, 111–136

Toomre, A. 1990, Gas-hungry Sc spirals., ed. Wielen, R., 292–303

Toomre, A. & Toomre, J. 1972, ApJ, 178, 623

Trachternach, C., de Blok, W. J. G., Walter, F., Brinks, E., & Kennicutt, R. C. 2008, AJ, 136, 2720

Truesdell, C. A. 1952, J. Aero. Sci, 19, 826

van der Kruit, P. C. & Searle, L. 1981a, A&A, 95, 105

van der Kruit, P. C. & Searle, L. 1981b, A&A, 95, 116

van der Wel, A., Rix, H., Holden, B. P., Bell, E. F., & Robaina, A. R. 2009, ApJ, 706, L120

van Woerden, H. & Wakker, B. P. 2004, in Astrophysics and Space Science Library, Vol. 312, High Velocity Clouds, ed. H. van Woerden, B. P. Wakker, U. J. Schwarz, & K. S. de Boer , 195–+

van Zee, L. & Bryant, J. 1999, AJ, 118, 2172

Vauterin, P. & Dejonghe, H. 1996, A&A, 313, 465

Vishniac, E. T. 1994, ApJ, 428, 186

Visser, H. C. D. 1978a, in IAU Symposium, Vol. 77, Structure and Properties of Nearby Galaxies, ed. E. M. Berkhuijsen & R. Wielebinski, 105–111

Visser, H. C. D. 1978b, The dynamics of the spiral galaxy M81, ed. Visser, H. C. D.

Vogel, S. N., Kulkarni, S. R., & Scoville, N. Z. 1988, Nature, 334, 402

Wada, K. & Koda, J. 2004, MNRAS, 349, 270

Wakker, B. P., York, D. G., Howk, J. C., et al. 2007, ApJ, 670, L113

Walter, F., Brinks, E., de Blok, W. J. G., et al. 2008, AJ, 136, 2563

White, S. D. M. & Rees, M. J. 1978, MNRAS, 183, 341

Whitmore, B. C., Gilmore, D. M., & Jones, C. 1993, ApJ, 407, 489

Wong, T., Blitz, L., & Bosma, A. 2004, ApJ, 605, 183

Woodward, P. R. 1975, ApJ, 195, 61

Wouterloot, J. G. A., Brand, J., Burton, W. B., & Kwee, K. K. 1990, A&A, 230, 21

Yang, C., Gruendl, R. A., Chu, Y., Mac Low, M., & Fukui, Y. 2007, ApJ, 671, 374

Yuan, C. & Kuo, C. 1997, ApJ, 486, 750

Zang, T. A. & Hohl, F. 1978, ApJ, 226, 521

Zaritsky, D. & Rix, H. 1997, ApJ, 477, 118

Zhang, X. 1996, ApJ, 457, 125

Zhang, X. 1998, ApJ, 499, 93

Zhang, X. 1999, ApJ, 518, 613

Zhang, X. 2002, Ap&SS, 281, 281

Zhang, X., Lee, Y., Bolatto, A., & Stark, A. A. 2001, ApJ, 553, 274

Acknowledgments

I would like to thank all the people who have helped and supported me during my PhD study.

It is very hard to express my gratitude to Prof. Ralf Klessen and Prof. Kees Dullemond in a few words! Whenever I had difficulties, they were always there supporting me. They spent a lot of time listening to my questions. They offered their invaluable insights to these questions and patiently explained things to me. They created opportunities for me to contact and discuss scientific issues with other outstanding researchers. They broaden not only my field of view but also my mind.

Thank you Dr. Christian Fendt for taking good care of me that makes my life in Germany enjoyable.

Thank you to Dr. Fabian Walter, Dr. Frank van den Bosch, Prof. Lucio Mayer and Prof. Romain Teyssier for the constructive scientific discussions. These inspiring discussions help me think from different angles.

Many thanks to all the people who contribute to my works for the fruitful discussions: Prof. Ralf Klesseen, Prof. Kees Dullemond, Prof. Frank van den Bosch, Prof. Burkhard Fuchs, Dr. Frank Bigiel, Prof. Erwin de Blok, Dr. Fabian Walter.

I am also thankful to my committee members (Prof. Ralf Klessen, Dr. Henrik Beuter, Prof. Kees Dullemond and Prof. Luca Amendola) for reading the thesis and for your time participating my defense.

I would like to thank my family. Although the distance between the Taiwan and the Germany, you let me know there is always a home supporting me in any situation. Thanks to all my friends and colleaques sharing my enjoyable life in Germany. Thank you to Bhargav for your hospitable host when I was in Santa Cruz and also for the interesting scientific discussions. Finally, I would like to thank you Shih-Yi for listening the everyday murmur when I was in depression.